

**INFLUENCE OF HEAT TREATMENT ON THE  
CORROSION BEHAVIOR OF  
SUPER-AUSTENITIC STAINLESS STEEL**

BY

**Hani Mohamed Razaz Ahmed**

A Thesis Presented to the  
**DEANSHIP OF GRADUATE STUDIES**

**KING FAHD UNIVERSITY OF PETROLEUM & MINERALS**

DHAHRAN, SAUDI ARABIA

In Partial Fulfillment of the  
Requirements for the Degree of

**MASTER OF SCIENCE**

In

**MATERIAL SCIENCE AND ENGINEERING**

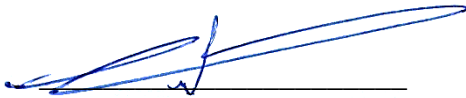
**April 2023**

KING FAHD UNIVERSITY OF PETROLEUM & MINERALS

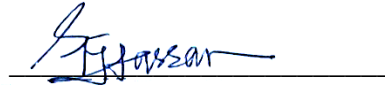
DHAHRAN- 31261, SAUDI ARABIA

**DEANSHIP OF GRADUATE STUDIES**

This thesis, written by **Hani Mohamed Razaz Ahmed** under the direction of his thesis advisor and approved by his thesis committee, has been presented and accepted by the Dean of Graduate Studies, in partial fulfillment of the requirements for the degree of **MASTER OF SCIENCE IN MATERIALS SCIENCE & ENGINEERING.**



Dr. Turki N. Baroud  
Department Chairman



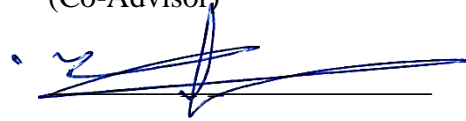
Dr. Fida Hassan Syed  
(Advisor)



Dr. Akeem Y. Adesina  
(Co-Advisor)



Dr. Suliman S. Al-Homidan  
Dean of Graduate Studies



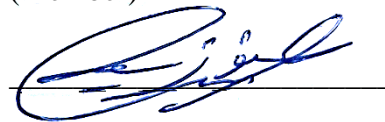
Dr. Turki N. Baroud  
(Member)

\_\_\_\_\_

Date



Dr. Ahmad A. Sorour  
(Member)



Dr. Nouari Saheb  
(Member)

© Hani Mohamed Razaz Ahmed

**2023**

*Dedication*

*To My Family*

## ACKNOWLEDGMENTS

First, I would like to thank God almighty for allowing me to finish this thesis, then to my wife and the rest of my family for giving me the support and encouragement in my work and studies.

I would also like to thank Dr. Fida Hassan Syed, my advisor, for his continuous guidance and teachings. I have gained so much from him and will continue to do so Insha'allah. My thanks also go to Dr. Akeem Y. Adesina, my Co-advisor, for his great help, support, and effort with labs access, implementing correct scientific experiment methodology & analysis procedures and continuous review & feedback on the results generated from this work. Furthermore, POSTDOC. Nestor K. Ankah for his valuable involvement and effort with heat-treated samples during lab activities to achieve our desired objectives.

I would also like to thank the committee members, Dr. Turki N. Baroud, Dr. Nouari Saheb and Dr. Ahmad A. Sorour for their valuable involvement, feedback and comments. Finally, thanks to King Fahd University of Petroleum & Minerals (KFUPM) in Dhahran and its Research Institute (RI) for creating and funding this project and support throughout project completion.

# TABLE OF CONTENTS

|  |      |
|--|------|
| ACKNOWLEDGMENTS  | V    |
| TABLE OF CONTENTS  | VI   |
| LIST OF TABLES   | VII  |
| LIST OF FIGURES  | VIII |
| LIST OF ABBREVIATIONS  | X    |
| ABSTRACT   | XI   |
| ملخص الرسالة   | XIII |
| CHAPTER 1  | 1    |
| 1.1. INTRODUCTION  | 1    |
| 1.2. THESIS OBJECTIVES   | 5    |
| CHAPTER 2  | 6    |
| 2.1. LITERATURE REVIEW   | 6    |
| CHAPTER 3  | 17   |
| 3.1. EXPERIMENTAL PROCEDURE                                    | 17   |
| 3.1.1 AS RECEIVED SAMPLE [UNS N08029 (Alloy 29) - SANICRO® 29] | 17   |
| 3.1.2 HEAT TREATMENT PROGRAM                                   | 18   |
| 3.1.3 SAMPLE PREPARATION & HEAT TREATMENT                      | 21   |
| 3.1.4 SAMPLE PREPARATION FOR CHARACTERIZATION                  | 21   |
| 3.1.5 ELECTROCHEMICAL CORROSION MEASUREMENTS                   | 22   |
| 3.2. RESULTS AND DISCUSSION                                    | 24   |
| 3.2.1 CHARACTERIZATION OF HEAT-TREATED SAMPLES                 | 24   |
| 3.2.2 ELECTROCHEMICAL CORROSION OF HEAT-TREATED SAMPLES        | 41   |
| 3.2.3 HARDNESS OF HEAT-TREATED SAMPLES                         | 70   |
| 3.3. CONCLUSIONS   | 71   |
| REFERENCES   | 74   |
| VITAE  | 77   |

# LIST OF TABLES

|   |    |
|---|----|
| TABLE 1 EFFECT OF ALLOYING ELEMENTS ON STEEL MATRIX [1] .....   | 6  |
| TABLE 2 INTERMETALLIC PHASES CLASSIFICATION [1] .....   | 7  |
| TABLE 3 LITERATURE REVIEW OF AUSTENITIC STAINLESS STEEL HT PROGRAMS AND MICROSTRUCTURAL<br>FINDINGS .....   | 14 |
| TABLE 4 ALLOY 29 CHEMICAL COMPOSITION (NOMINAL) % .....   | 17 |
| TABLE 5 AVERAGE GRAIN SIZE OF AS-RECEIVED AND HEAT-TREATED SAMPLES AS FUNCTION OF<br>SOLUTIONIZING DURATION .....   | 28 |
| TABLE 6 EDS ANALYSIS SHOWING THE AVERAGE ELEMENTAL COMPOSITION OF THE PHASES FOR VARIOUS<br>SAMPLES .....   | 32 |
| TABLE 7 AVERAGE GRAIN SIZE OF AS-RECEIVED AND HEAT-TREATED SAMPLES AS FUNCTION OF<br>SOLUTIONIZING TEMPERATURE .....  | 36 |
| TABLE 8 LPR PARAMETERS FOR THE SAMPLES SOLUTIONIZED FOR DIFFERENT DURATIONS .....   | 43 |
| TABLE 9 LPR PARAMETERS FOR THE SAMPLES SOLUTIONIZED FOR DIFFERENT TEMPERATURES .....  | 44 |
| TABLE 10 TAFEL EXTRAPOLATION AND PITTING PARAMETERS OBTAINED FROM THE CPDP MEASUREMENT<br>FOR THE SAMPLES HEAT-TREATED AT DIFFERENT SOLUTIONIZING DURATIONS .....   | 48 |
| TABLE 11 TAFEL EXTRAPOLATION AND PITTING PARAMETERS OBTAINED FROM THE CPDP MEASUREMENT<br>FOR THE SAMPLES HEAT-TREATED AT DIFFERENT SOLUTIONIZING TEMPERATURES .....  | 48 |
| TABLE 12 EIS PARAMETERS OBTAINED FROM THE EC FITTING FOR THE SAMPLES SOLUTIONIZED FOR<br>DIFFERENT DURATIONS .....  | 52 |
| TABLE 13 EIS PARAMETERS OBTAINED FROM THE EC FITTING FOR THE SAMPLES SOLUTIONIZED FOR<br>DIFFERENT TEMPERATURES .....   | 52 |
| TABLE 14 TAFEL EXTRAPOLATION AND PITTING PARAMETERS OBTAINED FROM THE CPDP MEASUREMENT<br>FOR THE AS-RECEIVED SAMPLE AT DIFFERENT TEMPERATURE STEEPNESS FOR THE CPT BEHAVIOR OF<br>N08029 AFTER 1 H IMMERSION IN 3.5 % NaCl AERATED SOLUTION. ....                      | 62 |
| TABLE 15 TAFEL EXTRAPOLATION AND PITTING PARAMETERS OBTAINED FROM THE CPDP MEASUREMENT<br>FOR THE A10T120 SAMPLE AT DIFFERENT TEMPERATURE STEEPNESS FOR THE CPT BEHAVIOR OF<br>N08029 AFTER 1 H IMMERSION IN 3.5 % NaCl AERATED SOLUTION. ....                          | 62 |
| TABLE 16 TAFEL EXTRAPOLATION AND PITTING PARAMETERS OBTAINED FROM THE CPDP MEASUREMENT<br>FOR THE A12T120 SAMPLE AT DIFFERENT TEMPERATURE STEEPNESS FOR THE CPT BEHAVIOR OF<br>N08029 AFTER 1 H IMMERSION IN 3.5 % NaCl AERATED SOLUTION. ....                          | 62 |
| TABLE 17 BREAKDOWN POTENTIAL AT 10 mA/cm <sup>2</sup> OBTAINED FROM THE CPDP MEASUREMENT FOR AS-<br>RECEIVED, A10T120 AND A12T120 SAMPLES AT DIFFERENT TEMPERATURE STEEPNESS FOR THE<br>CPT BEHAVIOR OF N08029 AFTER 1 H IMMERSION IN 3.5 % NaCl AERATED SOLUTION. .... | 68 |

## LIST OF FIGURES

|   |    |
|---|----|
| FIGURE 1 TERNARY FE–CR–C DIAGRAM ON THE TEMPERATURE X% CR (IN WT%) PLANE [1] .....  | 8  |
| FIGURE 2 AUSTENITIC LOOP EXPANSION WITH NITROGEN CONTENT (IN WT%) [1] .....   | 9  |
| FIGURE 3 AUSTENITIC LOOP EXPANSION WITH NI CONTENT (IN WT%) IN TERNARY FE–CR–NI ALLOYS [1] 10   | 10 |
| FIGURE 4 ADOPTED FIGURE OF MAIN TRANSFORMATIONS THAT ARE GENERALLY OCCUR IN AUSTENITIC<br>STAINLESS STEELS DURING HEAT TREATMENT [1].....   | 11 |
| FIGURE 5 CALCULATED PHASE DIAGRAMS OF ALLOY 28 USING THERMO-CALC SOFTWARE: (A)<br>RELATIONSHIP OF MASS FRACTION OF PHASES TO TEMPERATURE; (B) PARTIAL ENLARGED DETAIL OF<br>(A) [3].....                                | 12 |
| FIGURE 6 SCHAEFFLER’S CONSTITUTION DIAGRAM FOR STAINLESS STEELS [1].....  | 18 |
| FIGURE 7 EXPERIMENTAL MATRIX AND FLOW CHART SHOWING THE SEQUENCE OF THE HEAT TREATMENT<br>AND CORROSION TESTING.....  | 20 |
| FIGURE 8 (A) OPTICAL IMAGE (B) SEM IMAGE OF THE AS-RECEIVED (ALLOY 29).....   | 25 |
| FIGURE 9 (A-C) OPTICAL IMAGES (D-F) GRAIN SIZE DISTRIBUTION OF SOLUTIONIZED SAMPLES (A,D)<br>A12T30, (B,E) A12T60 AND (C,F) A12T90.....   | 26 |
| FIGURE 10 (A-C) OPTICAL IMAGES (D-F) GRAIN SIZE DISTRIBUTION OF SOLUTIONIZED SAMPLES (A,D)<br>A12T120, (B,E) A12T180 AND (C,F) A12T240.....   | 27 |
| FIGURE 11 (A-C) SEM IMAGES WHICH REVEAL GRAINS ARRANGEMENT OF SOLUTIONIZED SAMPLES (A,A <sub>1</sub> )<br>A12T30, (B,B <sub>2</sub> ) A12T60 AND (C,C <sub>1</sub> ) A12T90.....  | 29 |
| FIGURE 12 (A-C) SEM IMAGES WHICH REVEAL GRAINS ARRANGEMENT OF SOLUTIONIZED SAMPLES (A,A <sub>1</sub> )<br>A12T120, (B,B <sub>2</sub> ) A12T180 AND (C,C <sub>1</sub> ) A12T240.....                                     | 29 |
| FIGURE 13 SAMPLE EDX SPECTRUM DETAIL OF SOLUTIONIZED SAMPLES (A) A12T90, (B) A10T120 AND (C)<br>A12T30 .....  | 34 |
| FIGURE 14 (A-D) OPTICAL IMAGES (D-H) GRAIN SIZE DISTRIBUTION OF SOLUTIONIZED SAMPLES (A,E)<br>A10T120, (B,F) A11T120, (E,G) A12T120 AND (D,H) A13T120 .....   | 35 |
| FIGURE 15 (A-C) SEM IMAGES WHICH REVEAL GRAINS ARRANGEMENT OF SOLUTIONIZED SAMPLES (A,A <sub>1</sub> )<br>A10T120, (B,B <sub>2</sub> ) A11T120 AND (C,C <sub>1</sub> ) A13T120.....                                     | 37 |
| FIGURE 16 XRD PATTERNS OBTAINED FROM HEAT-TREATED SPECIMEN SHOWING THE EFFECT OF<br>SOLUTIONIZING DURATION.....   | 39 |
| FIGURE 17 XRD PATTERNS OBTAINED FROM HEAT-TREATED SPECIMEN SHOWING THE EFFECT OF<br>SOLUTIONIZING TEMPERATURE.....  | 40 |
| FIGURE 18 (A) OPEN CIRCUIT POTENTIALS SHOWING THE EFFECT OF SOLUTIONIZING DURATION AND (B)<br>SOLUTIONIZING TEMPERATURE ON THE CORROSION BEHAVIOR OF N08029 AFTER 1 H IMMERSION<br>IN 3.5 % NaCl AERATED SOLUTION. .... | 41 |
| FIGURE 19 LPR CURVES SHOWING THE EFFECT OF (A) SOLUTIONIZING DURATION AND (B) SOLUTIONIZING<br>TEMPERATURE ON THE CORROSION BEHAVIOR OF N08029 AFTER 1 H IMMERSION IN 3.5 % NaCl<br>AERATED SOLUTION.....               | 42 |
| FIGURE 20 CPDP CURVES SHOWING THE EFFECT OF (A) SOLUTIONIZING DURATION AND (B)<br>SOLUTIONIZING TEMPERATURE ON THE CORROSION BEHAVIOR OF N08029 AFTER 1 H IMMERSION<br>IN 3.5 % NaCl AERATED SOLUTION. ....             | 45 |
| FIGURE 21 EIS PLOTS, (A) MODULUS AND PHASE ANGLE, AND (B) NYQUIST PLOTS, SHOWING THE EFFECT<br>OF.....  | 48 |
| FIGURE 22 EIS PLOTS, (A) MODULUS AND PHASE ANGLE, AND (B) NYQUIST PLOTS, SHOWING THE EFFECT<br>OF.....  | 49 |

|   |    |
|---|----|
| FIGURE 23 SCHEMATIC ILLUSTRATION OF THE CORROSION PROCESS OF N08029 AFTER 1 H IMMERSION IN 3.5 % NACL AERATED SOLUTION [3].....   | 53 |
| FIGURE 24 (A-C) SEM IMAGES WHICH REVEAL GRAINS ARRANGEMENT OF SOLUTIONIZED SAMPLES (A,A <sub>1</sub> ) A12T120, (B,B <sub>2</sub> ) A12T180 AND (C,C <sub>1</sub> ) A12T240.....  | 54 |
| FIGURE 25 CPDP AND LPR CORROSION RATES OF AS-RECEIVED SAMPLE AND ALL SOLUTIONIZED SAMPLES OF N08029 AFTER 1 H IMMERSION IN 3.5 % NACL AERATED SOLUTION. ....  | 56 |
| FIGURE 26 CPDP CURVES SHOWING THE EFFECT OF TEMPERATURE STEEPNESS VERSUS PITTING CORROSION ON (A) AS-RECEIVED SAMPLE (B) A10T120 AND (C) A12T120 SOLUTIONIZED SAMPLES ON THE CPT BEHAVIOR OF N08029 AFTER 1 H IMMERSION IN 3.5 % NACL AERATED SOLUTION.....   | 57 |
| FIGURE 27 OPEN CIRCUIT POTENTIALS SHOWING THE EFFECT OF TEMPERATURE STEEPNESS VERSUS PITTING CORROSION ON (A) AS-RECEIVED SAMPLE (B) A10T120 AND (C) A12T120 SOLUTIONIZED SAMPLES ON THE CPT BEHAVIOR OF N08029 AFTER 1 H IMMERSION IN 3.5 % NACL AERATED SOLUTION.....   | 61 |
| FIGURE 28 PITTING POTENTIAL VS. TEMPERATURE CURVES SHOWING THE EFFECT OF TEMPERATURE STEEPNESS VERSUS PITTING CORROSION ON AS-RECEIVED, A10T120 AND A12T120 SOLUTIONIZED SAMPLES ON THE CPT BEHAVIOR OF N08029 AFTER 1 H IMMERSION IN 3.5 % NACL AERATED SOLUTION. ....   | 65 |
| FIGURE 29 LOCAL PASSIVITY CURRENT DENSITY VS. TEMPERATURE CURVES SHOWING THE EFFECT OF TEMPERATURE STEEPNESS VERSUS PITTING CORROSION ON AS-RECEIVED, A10T120 AND A12T120 SOLUTIONIZED SAMPLES ON THE CPT BEHAVIOR OF N08029 AFTER 1 H IMMERSION IN 3.5 % NACL AERATED SOLUTION.....  | 66 |
| FIGURE 30 BREAKDOWN POTENTIAL VS. TEMPERATURE CURVES SHOWING THE EFFECT OF TEMPERATURE STEEPNESS VERSUS PITTING CORROSION ON AS-RECEIVED, A10T120 AND A12T120 SOLUTIONIZED SAMPLES ON THE CPT BEHAVIOR OF N08029 AFTER 1 H IMMERSION IN 3.5 % NACL AERATED SOLUTION.....  | 67 |
| FIGURE 31 CPDP CURVES SHOWING THE EFFECT OF TEMPERATURE STEEPNESS VERSUS PITTING CORROSION ON AS-RECEIVED SAMPLE, A10T120 AND A12T120 SOLUTIONIZED SAMPLES ON THE CPT BEHAVIOR OF N08029 AFTER 1 H IMMERSION IN 3.5 % NACL AERATED SOLUTION. AT VARIOUS TEMPERATURE (A)RT(20°C) (B) 30°C (C) 40°C (D) 50°C (E) 60°C (F) 70°C AND (G) 85°C. .... | 69 |
| FIGURE 32 INFLUENCE OF AVERAGE GRAIN SIZE ON HARDNESS OF AS-RECEIVED AND HEAT-TREATED SAMPLES AS FUNCTION OF SOLUTIONIZING DURATION (A12T30, A12T60, A12T390, A12T120, A12T180 & A12T240) AND TEMPERATURE (A10T120, A11T120, A12T120 & A13T120). ....   | 70 |

## LIST OF ABBREVIATIONS

|             |   |  |
|-------------|---|--|
| $\alpha$    | : | Alpha                                  |
| $\beta$     | : | Beta                                   |
| SASS        | : | Super-austenitic Stainless Steel       |
| HAASS       | : | High-Alloy Austenitic Stainless Steel  |
| $\sigma$    | : | Sigma-Phase                            |
| XRD         | : | X-ray diffraction                      |
| EDS         | : | Energy dispersive spectroscopy         |
| GPa         | : | Giga pascal                            |
| MPa         | : | Megapascals                            |
| $\chi$      | : | Chi-Phase                              |
| $\gamma$    | : | Austenite-Phase                        |
| $M_{23}C_6$ | : | Carbides -Phase                        |
| OCP         | : | Open Circuit Potential                 |
| CPT         | : | Critical Pitting Temperature           |
| LPR         | : | Linear Polarization Resistance         |
| CPDP        | : | Cyclic Potentiodynamic Polarization    |
| EIS         | : | Electrochemical Impedance Spectroscopy |

## ABSTRACT

Full Name : [Hani Mohamed Razaz Ahmed]  
Thesis Title : [Influence of Selected Heat Treatment Programs On The Corrosion Behavior of Super-Austenitic Stainless Steel UNS 08029 (Alloy 29)]  
Major Field : [Material Science and Engineering]  
Date of Degree : [September 2022]

Super-austenitic Stainless Steel (SASS) is a family grade of stainless steel (SS) mainly with single-phase austenitic microstructure. SASS have been attracted several applications in oil & gas, power, petrochemical and water treatment industries due to their inherently mechanical properties (ductility and failure resistance) and great resistivity to corrosion. This study investigates the heat treatment effect on the alloy UNS N08029 (Alloy 29). The solution annealing of cold rolled super austenitic stainless steel UN08029 alloy was carried out to investigate the role of solutionizing duration and temperature on the electrochemical corrosion and pitting resistance of the alloy. Linear polarization, cyclic potentiodynamic, and electrochemical impedance spectroscopy techniques were used to evaluate the electrochemical behavior in 3.5% NaCl solution. The microstructural analysis of the solutionized samples revealed the occurrence of recrystallization from elongated columnar grains to uniform equiaxed grains, which size increases with duration and temperature. The charge transfer resistance shows an increasing corrosion protectiveness of 65%, 67%, 69%, 75%, 72% and 80 % after solutionizing for a duration of 30, 60, 90, 120, 180 and 240 min, respectively. Similarly, the resistance of the alloy was also increased by about 73%, 71%, 75%, and 42 % after solutionizing at temperatures of 1000°C, 1100°C, 1200°C, and 1300°C, respectively. In general, the solutionized samples demonstrated improved resistance over the As-Received alloy and this behavior increases with solutionizing duration and temperature. Though, the pitting potential drops below that of the As-Received, the hysteresis loop revealed that the solutionized samples are less prone to pitting damage and the sample solutionized at 1200°C for 120 min exhibited optimum pitting

corrosion resistance. The microstructural, hardness, elasticity and CPT influences on the corrosion and corrosion-rate were also discussed.

## ملخص الرسالة

|                      |   |
|----------------------|---|
| الاسم الكامل         | : [هاني محمد رزاز أحمد]   |
| عنوان الرسالة        | : [تأثير برامج المعالجة الحرارية المختارة على سلوك التآكل للفولاذ الأوستنيتي الفائق المقاوم للصدأ UNS 08029 (سبيكة 29)] |
| التخصص               | : [هندسة وعلم المواد]   |
| تاريخ الدرجة العلمية | : [سبتمبر 2022]   |

الفولاذ المقاوم للصدأ الأوستنيتي الفائق (SASS) هو فئة عائلية من الفولاذ المقاوم للصدأ بشكل أساسي مع بنية مجهرية أوستنيتي في طور الإشارة. اجتذبت (SASS) العديد من التطبيقات في صناعات النفط والغاز والطاقة والبتروكيماويات ومعالجة المياه نظرًا لخصائصها الميكانيكية بطبيعتها (اليونة ومقاومة الأعطال) ومقاومتها الكبيرة للتآكل. تبحث هذه الدراسة في تأثير المعالجة الحرارية على السبيكة UNS N08029 (السبيكة 29). تم إجراء التلدين بالمحلول لسبائك الفولاذ الأوستنيتي المقاوم للصدأ UN08029 الفائق المدلفن على البارد للتحقق من دور مدة المحلول ودرجة الحرارة على التآكل الكهروكيميائي ومقاومة التنقر للسبائك. تم استخدام تقنيات الاستقطاب الخطي والديناميكي الدوري والتحليل الطيفي للمقاومة الكهروكيميائية لتقييم السلوك الكهروكيميائي في محلول كلوريد الصوديوم بنسبة 3.5%. أظهر تحليل البنية المجهرية للعينات المحلول حدوث إعادة التبلور من حبيبات عمودية ممدودة إلى حبيبات منتظمة الشكل، والتي يزيد حجمها مع المدة ودرجة الحرارة. تظهر مقاومة نقل الشحنة حماية متزايدة ضد التآكل بنسبة 65% ، 67% ، 69% ، 75% ، 72% و 80% بعد الحل لمدة 30 ، 60 ، 90 ، 120 ، 180 و 240 دقيقة ، على التوالي. وبالمثل، تمت زيادة مقاومة السبيكة أيضًا بحوالي 73% و 71% و 75% و 42% بعد التحلل عند درجات حرارة 1000 درجة مئوية و 1100 درجة مئوية و 1200 درجة مئوية و 1300 درجة مئوية على التوالي. بشكل عام، أظهرت العينات المحلول مقاومة محسنة على سبيكة (As-Received) ويزداد هذا السلوك مع مدة الحل ودرجة الحرارة. على الرغم من انخفاض إمكانات التنقر إلى ما دون تلك الموجودة في (As-Received) ، كشفت حلقة التباطؤ أن العينات المحللة أقل عرضة لضرر التنقر وأن العينة التي تم حلها عند 1200 درجة مئوية لمدة 120 دقيقة أظهرت مقاومة التآكل المثلى. كما تمت مناقشة تأثيرات البنية المجهرية والصلابة والمرونة واختبار التآكل النقري الحرج على التآكل ومعدل التآكل.

# CHAPTER 1

## 1.1. INTRODUCTION

Fe-Ni based alloy, Super-austenitic Stainless Steel (SASS) or High-Alloy Austenitic Stainless Steel (HAASS) are a family grade of stainless steel (SS) mainly with single-phase austenitic microstructure [1]. Super austenitic stainless steel is a type of stainless steel that has even higher levels of corrosion resistance than traditional austenitic stainless steel. It contains a higher percentage of nickel, chromium, and molybdenum, which helps to improve its resistance to various types of corrosion, including crevice corrosion, pitting corrosion, and stress corrosion cracking [2]–[7]. SASS have been attracted several applications in oil & gas, power, petrochemical and water treatment industries due to their inherently mechanical properties (ductility and failure resistance) and great resistivity to corrosion. In addition to favourable cost-effective, Fe-Ni based alloys used in a highly corrosive environment such as phosphoric acid evaporator tubes, deep and sour gas well production tubing, casing, and liners, nuclear power plant heat exchangers, seawater piping and heat exchangers [2]–[7]. Alloying elements and impurities that are mixed with steel have a significant impact on austenite, ferrite, and cementite phase formation. The combination of alloying ingredients and exerted heat treatment program result in a wide range of microstructures and characteristics of an alloy. The austenitic phase is stabilized mainly when a high percentage of nickel and chromium elements exist [1]. The microstructural properties of alloys, in general, have a significant impact on their performance. During the heat treatment and welding procedures of many heavily alloyed steels, a range of desirable and undesirable precipitates occur, which can have a significant

impact on the mechanical properties and corrosion resistance of the steels [3]. SASS are commonly utilized in applications that require a higher level of pitting corrosion resistance. When highly alloyed steels are exposed to higher temperatures (550–1050°C), various secondary phases develop, influencing both mechanical characteristics and corrosion resistance [8].  $\sigma$ -phase has been found to be the most important intermetallic phase formed following heat treatment [8], [9]. It forms as austenite decomposes, releasing huge amounts of chromium and occasionally molybdenum into the austenitic matrix, forming Cr-rich compounds that deteriorate the steel's overall corrosion resistance [8]–[11]. The hard and brittle  $\sigma$ -phase transforms ductile austenitic steel into brittle steel when created in large volume fractions. Metal carbides, Cr-nitrides,  $\chi$ -phase (Chi-phase), and Laves phase are other frequent secondary phases that occur during the ageing of SASS [8]–[11]. This study investigates the heat treatment effect on the alloy UNS N08029 (Alloy 29) from the HAASS grade. Heat treatment is an economical approach that can be employed to further improve the corrosion properties of UNS N08029 alloy amidst the increasingly harsh environments and extreme conditions that are encountered by the oil & gas and other industries. Alloy 29 is developed specifically for improved localized corrosion resistance where the environment contains high chloride concentrations, CO<sub>2</sub> and H<sub>2</sub>S at high temperatures in which such an environment causes corrosion in lower alloyed materials. Annealing might be summarize as heating a metal above a critical temperature range, holding for a certain period of time, and slowly cooling [1]. Solution annealing is a heat treatment process which alters the metallurgical structure of a material to decrease metal crack sensitivity of aged material that needs to be returned to a weldable state. Several specialized heat treatments are applied to Oil & Gas and refinery equipment either to

enhance corrosion resistance in certain environments, facilitate in-service repair, or restore mechanical properties that have deteriorated during long-term service. For instance, heat treatment is applied prior to weld repair of alloys after long-term exposure in high-temperature service which called De-embrittlement process according to ASME and API terminologies. De-embrittlement restores ductility to the material so that welding repairs can be successfully made free of cracking. Similarly, Dehydrogenation (heat treatment process) is normally applied to steels prior to repair welding of refinery equipment exposed to services that can cause hydrogen-induced cracking (HIC). These services include wet hydrogen sulfide service, high-pressure/high-temperature hydrogen service, caustic service, or amine service. intended to help avoid delayed hydrogen cracking during or after repair welding which primarily intended to help avoid delayed hydrogen cracking during or after repair welding. Additionally, Post weld heat treatment (PWHT) conditions the weldment following welding. Its application, or misapplication, can dramatically affect in-service corrosion performance. PWHT is conducted at an elevated temperature, slightly below the transformation temperature for the alloy involved. The PWHT temperature is high enough for stress to flow and hard microstructures to temper. This results in reduced residual stress and a softer weld and heat-affected zone (HAZ). Super austenitic stainless steel can be exposed to high temperatures in a variety of industrial applications, including chemical processing, power generation, and oil and gas production. Some common causes of high temperature exposure in super austenitic stainless steel include:

Welding: Welding can generate high temperatures in the steel, particularly if the welding process is not properly controlled. The heat generated during welding can cause

sensitization and sigma phase formation, which can reduce the steel's corrosion resistance and mechanical properties.

**Heat treatment:** As mentioned earlier, heat treatment can be used to improve the mechanical properties and corrosion resistance of super austenitic stainless steel. However, if the steel is exposed to high temperatures for too long or at too high of a temperature, it can lead to the formation of sigma phase and other types of degradation.

**Elevated temperature service:** Super austenitic stainless steel may be exposed to high temperatures during its normal service life, such as in high-temperature chemical processing or power generation applications. In these cases, the steel may need to be specially designed and selected to withstand the specific temperature and environmental conditions.

**Fire exposure:** In the event of a fire or other high-temperature event, super austenitic stainless steel may be exposed to temperatures well beyond its normal operating range. In these cases, the steel may need to be inspected and potentially replaced to ensure that it remains safe and functional.

Overall, it is important to consider the potential for high temperature exposure when selecting and using super austenitic stainless steel, and to take appropriate measures to prevent degradation and ensure optimal performance.

Aforementioned paragraphs describe the importance of heat treatment (specifically solutionizing/annealing) which is the sole aim of this project because the heat treatment of metals and alloys often affects corrosion resistance, and once optimum heat treatment

program is specified, it is essential to be a major quality control limit of heat treatment operations such as importance of assuring that the proper austenitizing/annealing temperature and duration, the type of quenching media, aging temperature. However, to the best of our knowledge, no study has been conducted to investigate the effect of heat treatment on the corrosion properties of SASS UNS N08029 grade. Furthermore, there is no strategical study that evaluates the influence of annealing temperature and annealing duration, with the sole aim of attaining an optimum heat treatment program for this alloy grade. Therefore, this project is aimed to reveal the relationship between the composition and microstructural distribution in the deferent phase alloy and the corresponding effect on the corrosion properties for this alloy.

## **1.2. THESIS OBJECTIVES**

The main objective of the project is to investigate the influence of selected heat treatment programs on the corrosion behavior of super-austenitic stainless steel UNS 08029 (Alloy 29) in 0.6 M NaCl corrosive environment. This investigation is aimed at designing an optimum heat treatment program with the best corrosion behavior.

The specific objectives are:

1. Characterization of the heat-treated sample to understand the effect of the selected heat treatments on the microstructural evolution.
2. Evaluating the corrosion behavior of the treated samples in an aggressive environment and this will be compared with the untreated alloy (as received) as a control.
3. An optimum heat treatment program with the best corrosion performance will be designed.

## CHAPTER 2

### 2.1. LITERATURE REVIEW

Alloying elements and impurities that are paired with ferrite, austenite, and cementite along with heat treatment result in a wide range of microstructures and characteristics in steels which can be categorized into two groups; i) Austenite Stabilizers  
ii) Ferrite Stabilizers (see Table 1) [1].

**Table 1 Effect of Alloying Elements on Steel Matrix [1]**

| Austenite Stabilizers<br>(expanding $\gamma$ -field) | Ferrite Stabilizers<br>(contracting $\gamma$ -field)  |
|--|---|
| C, Co, Ni, Cu, Mn, N                                 | Mo, Si, Cr, W, P, Al, Sn, Sb,<br>As, Zr, Nb, B, S, Ce |

Figures 1, 2 & 3 show that carbon, nitrogen and nickel levels will increase in conjunction with chromium levels in order to stabilize austenite respectively, from the aforementioned figures, alloys having 13wt% Cr, must have a C concentration greater than 0.15wt% and heat treated to at least 950°C to complete phase austenitization. Similarly, alloys with a higher chromium content, such as 17wt%, must have a C percentage greater than 0.3wt% and heat-treated to at least 1100°C. As previously stated, both N and Ni are enlarging the  $\gamma$ -loop. There are two types of intermetallic phases (see Figure 4) that can be generally categorize in stainless steels as shown in Table 2. The most common heat treatment for austenitic stainless steels is solution annealing [1].

**Table 2 Intermetallic Phases Classification [1]**

| Topologically Close-Packed (TCP) Phases                      | Geometrically Close-Packed Phases (GCP)                                       |
|--|---|
| $\sigma, \chi, \text{Laves } (\eta), \text{G, R, Mu } (\mu)$ | $\gamma', \gamma'', \eta, \text{-Ni}_3\text{Ti}, \delta\text{-Ni}_3\text{Nb}$ |

The primary purpose of this treatment is to dissolve the phases that formed during the material's thermomechanical processing, particularly chromium-rich carbides of the  $M_{23}C_6$  type, where M could be Cr, Fe, and/or Mo. Because  $M_{23}C_6$  precipitates at temperatures between 450 and 900°C, the lower temperature limit for solution annealing should be over 900°C. Carbides should be dissolved; however, they take a long time to dissolve. The highest solution-annealing temperature is limited by grain growth. It's very important to avoid irregular grain development, commonly known as secondary recrystallization. It is worth to highlighting that compounds must not be confused with chemical compounds, therefore phases with crystallographic structures that differ from the components they are made up of have a different form of bonding than crystals and a chemically significant ratio [1]–[3]. For instance, alloy containing solid phases including two or more metallic or semi-metallic elements arranged in an ordered structure, such as iron compounds with non-carbides forming elements such as (Ni, Si, Co, Al, Cu, N), are known as intermetallic compounds. Nitrides in other hand, which is a chemical compound, formed when N level is greater than 0.015 % in steel and form chemical compounds with iron and/or with carbides forming elements such as (Cr, Mn, Mo, W, V, Ti, Zr, Nb) [1].

The sigma ( $\sigma$ ) phase is definitely one of the most investigated intermetallic compounds. Precipitation in austenitic stainless steel takes hundreds or even thousands of hours, and the precipitated volumetric percentage is usually less than 5% [1]–[3]. When compared to the original austenite, usually precipitation is represented by the reaction  $\gamma \rightarrow \gamma^* + \sigma$  where  $\gamma^*$  is a Cr & Mo ( $\sigma$  Stabilizers) depleted austenite. Precipitation is more common around grain interfaces, particularly triple spots [8]–[12].

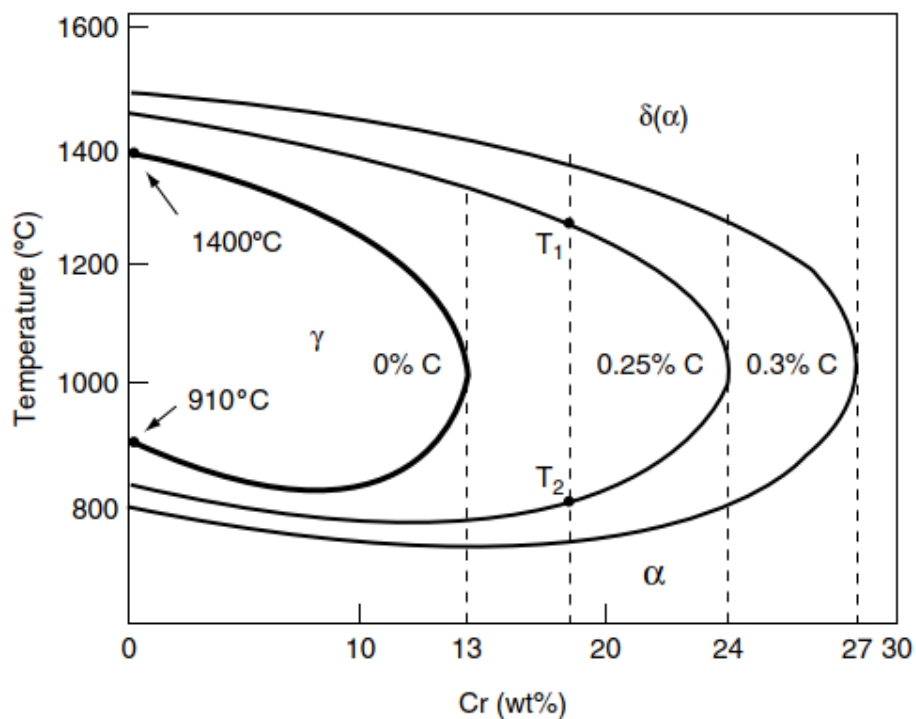


Figure 1 Ternary Fe–Cr–C Diagram on The Temperature x% Cr (in wt%) Plane [1]

Yan Jiang et al. investigated the evolution of the sigma phase in a commercial HAASS alloy N08028 (Ni-32, Cr-26.69, Mo-3.3 Mn-0.9, Fe-bal. [nominal wt%]) in which water was quenched after a 2-hour solution annealing treatment at 1200°C, followed by aging at 900, 950, and 1000°C for periods ranging from 0.5 to 16 hours. They found that the sigma phase, in any event, tends to break out with a granular shape at grain boundaries first, and that as time passes, it is forced to precipitate with a lamellar structure in grain interiors.

This sequence occurs due to solute atom redistribution and the difference in thermodynamic driving force and kinetic activation energy coupling effects between intergranular and intra-granular precipitation. Furthermore, they reported that the volume fraction of the sigma phase increases as the aging temperature decreases, and that the distribution position has a significant impact on the morphology of the sigma phase by changing the competition between interface and strain energy [2].

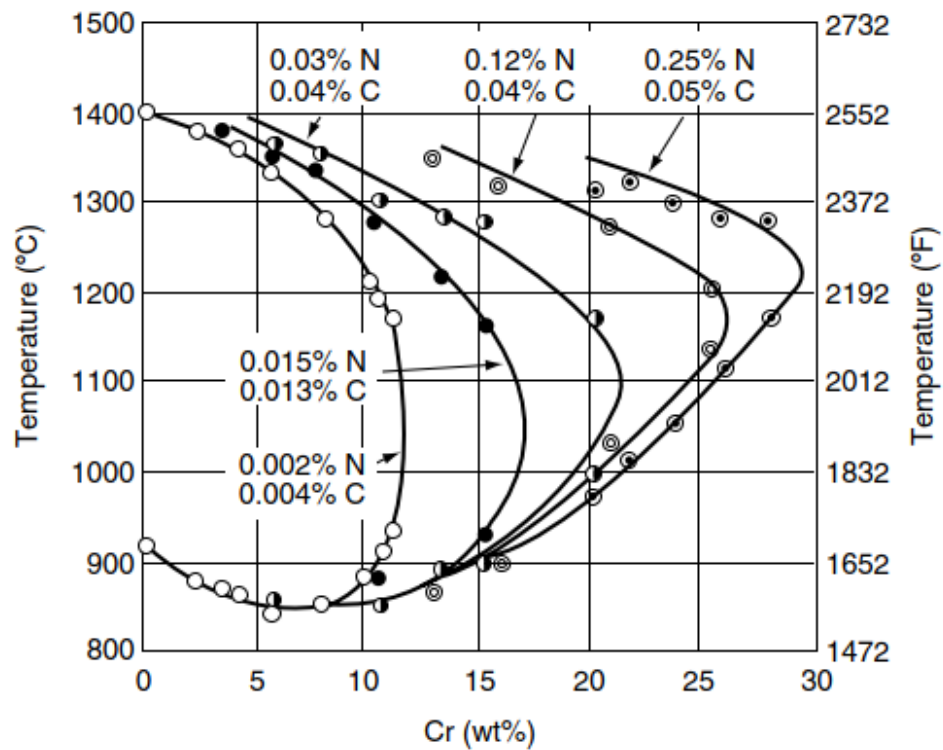


Figure 2 Austenitic Loop Expansion With Nitrogen Content (in wt%) [1]

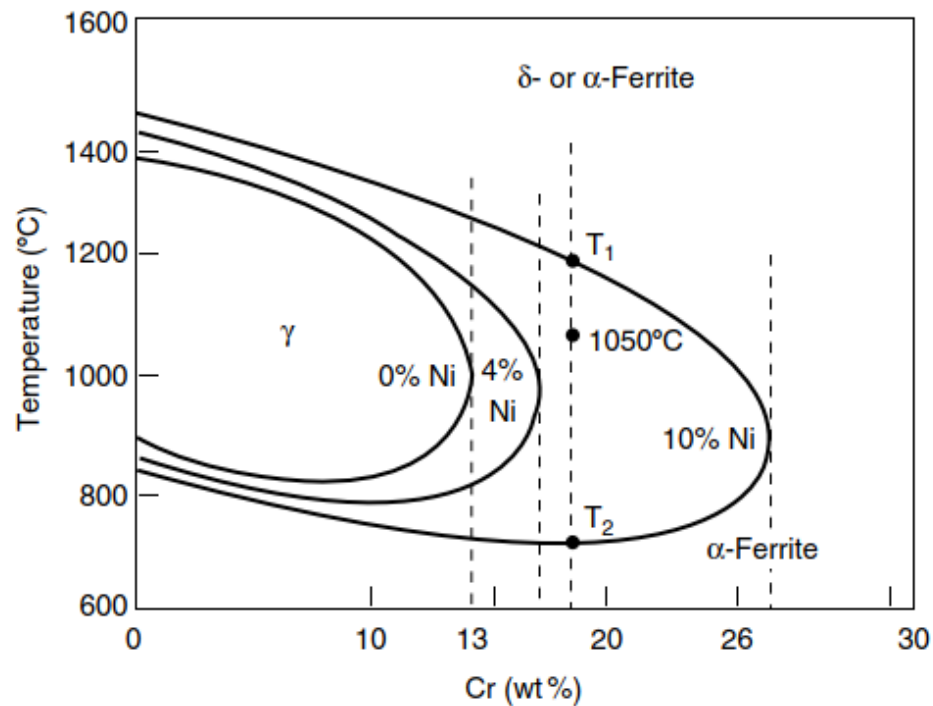


Figure 3 Austenitic Loop Expansion with Ni Content (in wt%) in Ternary Fe–Cr–Ni Alloys [1]

The relationship between microstructure and characteristics of SASS grades S31254 (Ni-18.16, Cr-20.02, Mo-5.98 Mn-0.47, N-0.214, Cu-0.65, Fe-bal. [nominal wt%]) and S32654 (Ni-21.58, Cr-24.19, Mo-7.24 Mn-3.43, N-0.497, Cu-0.38, Fe-bal. [nominal wt%]) was investigated by T. Koutsoukis et al [8]. Air cold after heat treatments takes place between 650 and 950 °C, with a step of 100 °C, aged between 0.5 and 3000 hours and then water quenched. After the aging period, the study revealed 4 different types of precipitates:  $\sigma$ -phase,  $\chi$ -phase, Laves phase, and  $\beta$ -Cr<sub>2</sub>N nitride. Results show that Laves phase is the first secondary phase to form, followed by  $\sigma$ -phase,  $\chi$ -phase and  $\beta$ -Cr<sub>2</sub>N as time goes on. At an ageing temperature of 950 °C, the full change of Laves phase to the sigma phase and/or dissolving in the matrix happen within 240-h. In both alloys, precipitation of predominantly Laves phase and  $\sigma$ -phase resulted in an increase in hardness values at all temperatures [8]. The influence of heat treatment on the microstructure and corrosion behavior is investigated by L.N. Zhang et al. [3].

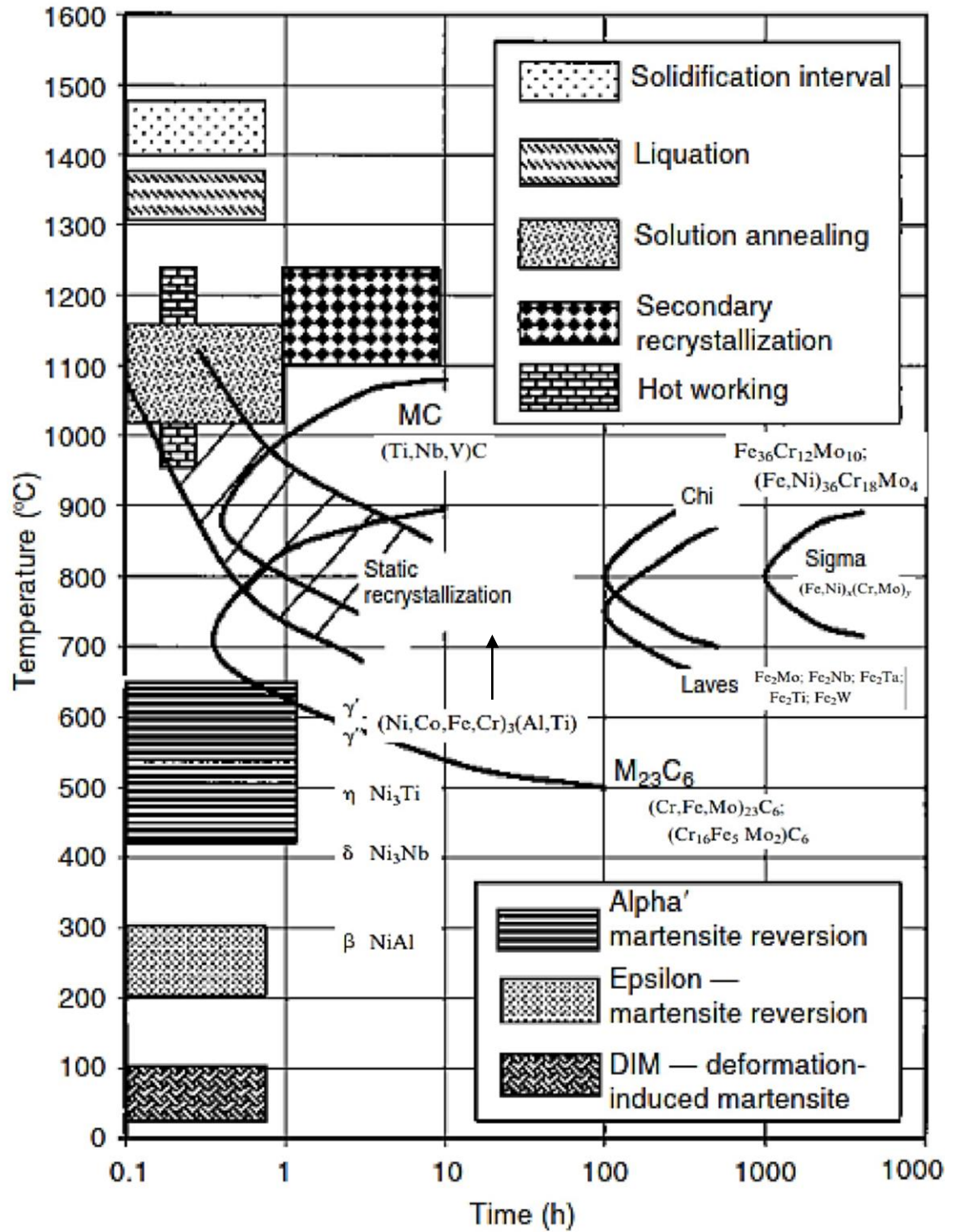


Figure 4 Adopted Figure of Main Transformations That Are Generally Occur in Austenitic Stainless Steels During Heat Treatment [1]

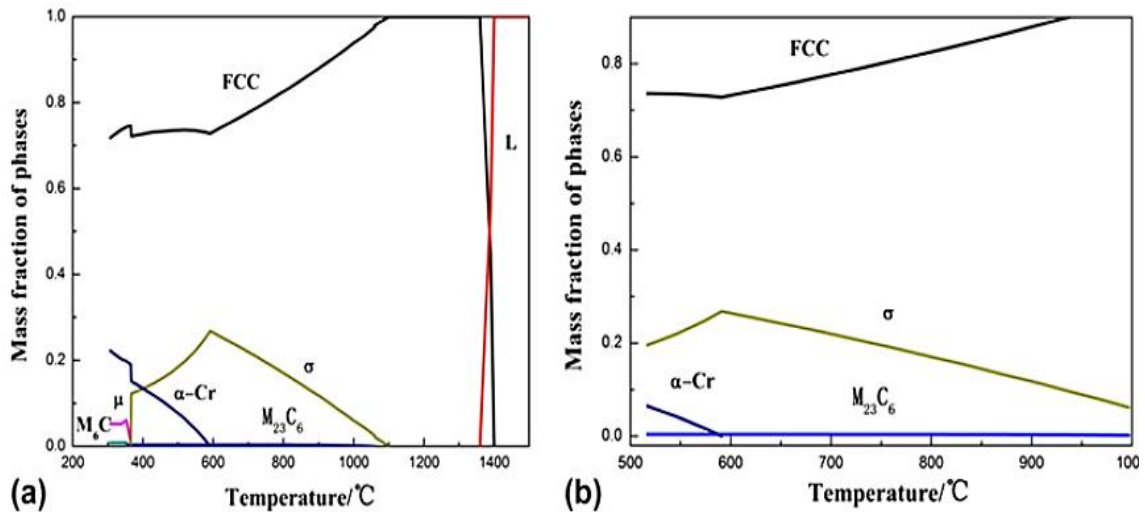


Figure 5 Calculated Phase Diagrams of Alloy 28 Using Thermo-Calc Software: (a) Relationship of Mass Fraction of Phases to Temperature; (b) Partial Enlarged Detail of (a) [3]

For the same aging time, they reported that the precipitation rate is higher at 900 °C than at 850 and 950 °C. According to the thermodynamic calculations presented in Figure 5,  $\sigma$ -phase begins to form at 1090 °C and reaches its maximum temperature around 600 °C, carbide first occurs at 1060 °C and remains quite low throughout the precipitation temperature range. Hence, the sigma phase is the most important component in precipitation in Alloy 28. Furthermore, as aging time progresses, the hardness and intermetallic precipitation increase. Similarly, when the amount of precipitates increases, the corrosion rate increases, implying that the presence of precipitates reduces corrosion resistance [3]. J. Anburaj et al. reported that Alloy-7Mo (Ni-16.23, Cr-20.47, Mo-7.26 Mn-0.61, N-0.37, Cu-0.4, Fe-bal. [nominal wt%]) was heat treated at 1250°C for three hours and then aged at 500 to 1000°C for one hour and ten hours. At 900°C, sigma is richer in Mo and can be deleterious to SASS toughness due to susceptibility for de-cohesion with the austenite matrix [13]. The influence of cooling rate following heat treatment on pitting corrosion SDSS of UNS S32750 (Ni-6.8, Cr-25, Mo-3.8 Mn-0.79, N-0.27, Cu-0.18, Fe-bal. [nominal wt%]) was investigated by Byung-Hyun Shin et al [14]. The austenite volume

fraction increased while the ferrite volume fraction fell when the cooling rate was reduced from 5,600.0 J/s (water cooling) to 1.9 J/s (air cooling) at the same temperature. At all temperatures, lowering the cooling rate to 0.4 J/s (furnace cooling) improved the precipitation of the secondary phases [14]. Table 3 summarized the finding of literature review of austenitic stainless steel undergone thought heat-treatment processes and correlated microstructural findings. It is observed that most of the studies are focusing on aging temperature. It is confirmed that precipitations are invadable during the aging process.  $\sigma$ -phase, carbides,  $\chi$ -phase, Laves phase and  $\beta$ -Cr<sub>2</sub>N nitride are the common type of precipitations. Whereas  $\sigma$ -phase is the predominant secondary phase formed for commercially available SASS. Aging time have been reported from 0.5 to 3000 hours in a temperature range of 650 to 950°C and the findings confirmed that the precipitates always tend to separate out primarily at grain boundaries, and then arise at grain interiors. Studies confirms the formation of the precipitates but differs in shape and volume fraction, and is in proportion to aging time and temperature. In addition, the carbides have granular structure, the  $\sigma$  phase forms short rod-like structures. With the increase of aging time, precipitates at grain boundaries are coarsening and also form continuous chain structures. Moreover, the needle-like  $\sigma$  phase is formed in grains with an increase of the holding time. However,  $\chi$ -phase, Laves phase and  $\beta$ -Cr<sub>2</sub>N are not reported to be presence in N08028 or N08029 grades of SASS. Whereas, they are commonly found in commercial grades of SS or HAASS. S31254, S32654 and Alloy-7Mo are the most commonly grades of SASS found to form  $\chi$ -phase, Laves phase and  $\beta$ -Cr<sub>2</sub>N at relatively low heat-treatment temperatures and durations. Moreover, starting from 800 °C and above along with longer duration full transformation begins to sigma and carbides phases.

Most available studies on SASS only investigated selected annealing temperatures without investigating the duration. Furthermore, studies which focused on the influence of heat-treatment on the corrosion properties for the SASS are very rare. This might be because they are considered from the emerging grade of austenitic stainless steels. The influence of heat-treatment on the microstructure and thus the corrosion behavior, of metallic alloys differs depending on the pre-processing condition, composition of the alloy, and the heat treatment program selected as well as the targeted properties to improve. Therefore, heat treatment programs are usually developed for specific alloy.

**Table 3 literature review of austenitic stainless steel HT programs and microstructural findings**

| Ref | Alloy  | Solution annealing conditions                            | Aging conditions  | Microstructure findings  |
|-----|--------|--|---|--|
| [2] | N08028 | Solution treated at 1200 °C for 2 h, water quenching     | Aged at 900, 950 and 1000 °C for a time duration ranging from 0.5 h to 16 h | The $\sigma$ phase always tends to separate out primarily at GBs, and then arise at GIs. This multi-stage behavior is correlated with the redistribution of solute atoms and with the difference in coupling effect of thermodynamic driving force and kinetic activation energy between the intergranular and the intragranular precipitation. The volume fraction of $\sigma$ phase increases with a decrease in aging temperature and this can be explained by the effects of atom diffusion, solid solubility and supercooling degree of phase transition. |
| [3] | N08028 | Solution treatment at 1200 °C for 0.5 h, water quenching | Aged at 850 °C/2 h, 900 °C/0.5,2,5 h, 950 °C/2 h air cooled                 | The precipitates preferentially form at the grain boundaries, the carbides have granular structure, the $\sigma$ phase forms short rod-like structures. With the increase of aging time, precipitates at grain boundaries are coarsening and also form continuous chain structures. Moreover, the needle-like $\sigma$ phase is formed in grains with an increase of the holding time.   |

|      |   |   |  |  |
|------|---|---|--|--|
| [8]  | S31254<br>and<br>S32654                               | Solution treatment in range 650–950°C with a step of 100°C for unspecified duration, air cooled | Aged at 850 °C or 950 °C for duration range 0.5 -3000 h, followed by water quenching       | <p>(i) At least four different types of precipitates, <math>\sigma</math>-phase, <math>\chi</math>-phase, Laves phase and <math>\beta</math>-Cr<sub>2</sub>N nitride, were identified following ageing of S32654 and S31254 within the temperature range of 650-950 °C. At all temperatures, Laves phase is the first secondary phase forming, followed by <math>\sigma</math>-phase and then at longer ageing times <math>\chi</math>-phase and the <math>\beta</math>-Cr<sub>2</sub>N nitride also form. Full transformation of Laves phase to <math>\sigma</math>-phase and/or its dissolution in the austenitic matrix takes place for time intervals over 240-h at an ageing temperature of 950 °C.</p> <p>(ii) Full transformation of Laves phase to <math>\sigma</math>-phase and/or its dissolution in the austenitic matrix takes place for time intervals over 240 h at an ageing temperature of 950 °C.</p> |
| [9]  | S31254<br>and<br>S32654                               | No solution treatment has been conducted  | Aged at 650, 750, 850 or 950°C for 1, 24 or 120 h, followed by water quenching             | <p>The cold rolled SASS S32654 and S31254 are susceptible to formation of secondary phases following aging within the temperature range of 650–950°C, in proportion to aging time and temperature, with <math>\sigma</math>-phase precipitates being the predominant, varying in morphology.</p>   |
| [10] | S31254<br>and<br>S32654                               | Solution treatment at 1080 °C for 1 h, water quenching  | Aged at 650, 750, 850 or 950°C for 1, 24, 120, 240, 500 and 1000 h, followed by air cooled | <p>(i) <math>\sigma</math>-phase is the predominant secondary phase formed on all stainless grades studied but differs in shape and volume fraction, and is in proportion to aging time and temperature. Well dispersed precipitates of size up to 10 <math>\mu</math>m were detected in S32654 and S31254 SASS alloys.</p> <p>(ii) intermetallic precipitation of <math>\sigma</math>-phase starts early at elevated temperatures, while its formation is delayed at 650°C, implying faster kinetics with the increase in aging temperature.</p>  |
| [11] | SASS alloys<br>N0 <sup>(1)</sup><br>N1 <sup>(2)</sup> | Solution treatment at 1170 °C for 1 h, water quenching  | Aged at 900°C for duration range 0 -168 h, followed by water quenching                     | <p>(i) In N0 and N1 alloys with and without nitrogen, the dominant second phase found in solution-treated and isothermally aged samples was the intermetallic sigma phase. From SAD patterns and stereographic projection, the main orientation relationship between sigma phase and austenite matrix was determined to be <math>(\bar{1}11)_\gamma // (00\bar{1})_\sigma</math>, <math>[\bar{1}10]_\gamma // [\bar{1}10]_\sigma</math>. Another less frequent orientation relationship was also found.</p>  |

|      |           |   |   |  |
|------|-----------|---|---|--|
|      |           |   | (ii) Two types of carbides ( $M_{23}C_6$ and $M_6C$ ) that showed the same orientation relationship with matrix were found in both N0 and N1 specimens. In spite of the similar FCC structures and very close lattice parameters of these two carbides, the different space groups of $M_6C$ and $M_{23}C_6$ ( $Fd\bar{3}m$ and $Fm\bar{3}m$ , respectively) permitted unique identification. |  |
| [12] | N08028    | Solution treatment at 1150 °C for 5 min, furnace cooled at cooling rate of about 300°C/s from 150°C to 800°C, and finally rapidly quenched. The times at target temperature were 100, 300, 1000, 3000, 10000, and 30000 s | No ageing has been conducted  | It was found that the sigma growth was diffusion limited after an initial nucleation period of about 300 s. APT showed very sharp interfaces between the austenite and the sigma phase, consistently narrower than 1 nm. By combining the growth kinetics from the electron micrographs with atomic resolution composition data on the sigma/austenite interface, it was possible to determine diffusion coefficients for the rate limiting elements that compare well with values found in general databases. The method used in this paper provides a direct measurement of the propagation velocities of the phase boundary, for grain boundary as well as lattice diffusion. The diffusion coefficients along the grain boundary were calculated to about 250 times that of lattice diffusion. |
| [13] | Alloy-7Mo | Solution treatment at 1250 °C for unspecified duration  | Aged at range of 500-1000°C with a step of 100°C for duration 1 h and 10 h  | (i) $\chi$ -phase was observed at ageing temperatures up to 800 °C and above this temperature it is unstable and gives rise to sigma. The elemental composition of $\chi$ -phase varies with temperature.<br>(ii) Sigma began to precipitate from temperatures of 850°C on, reached its highest concentration between 900°C and 1000°C, and dissolved completely above 1050°C. The elemental composition of sigma does not vary with temperature. Sigma shows a tendency of decohesion with austenite matrix and shows cleavage fracture.  |

(1) Chemical Composition [nominal wt%] (Ni-21.36, Cr-21.86, Mo-6 Mn-0.64, N-0.007, Al-0.08, Fe-bal.)

(2) Chemical Composition [nominal wt%] (Ni-21.78, Cr-21.87, Mo-6.05 Mn-0.64, N-0.295, Al-0.085, Fe-bal.)

## CHAPTER 3

### 3.1. EXPERIMENTAL PROCEDURE

#### 3.1.1 AS RECEIVED SAMPLE [UNS N08029 (Alloy 29) - SANICRO® 29]

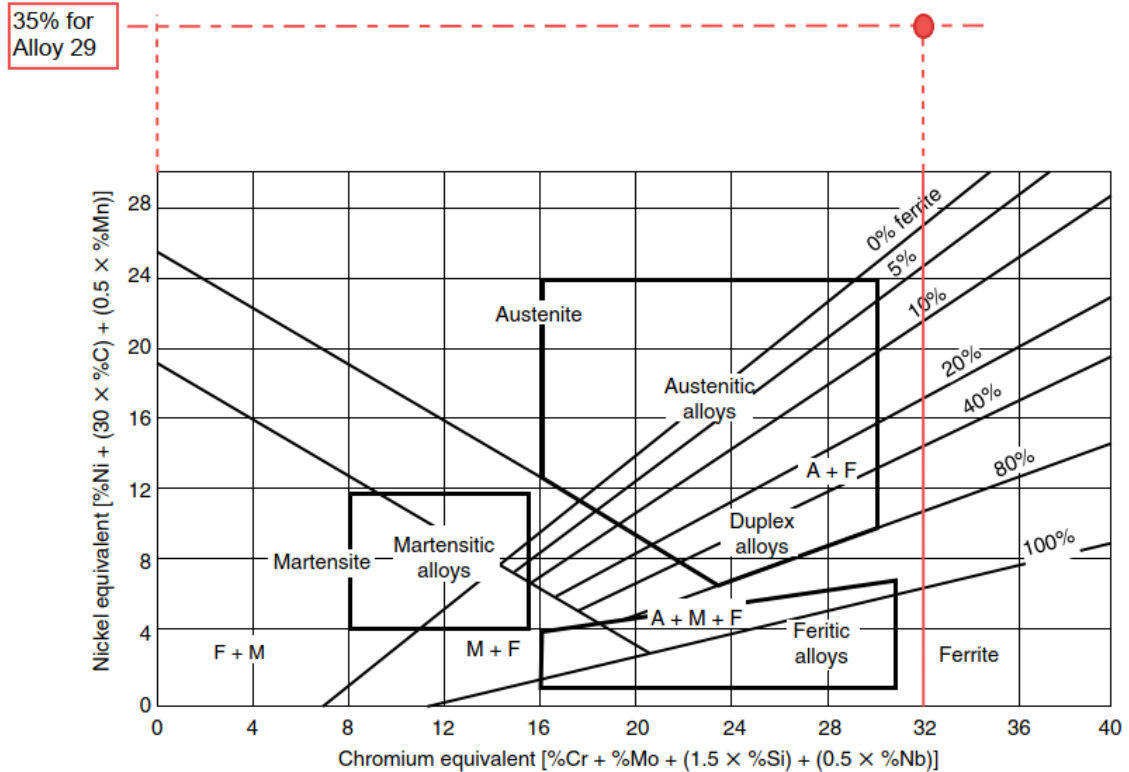
Alloy 29 is utilized in sour gas wells for high-strength downhole production tubing, casing, and liners. This includes high-temperature conditions, high CO<sub>2</sub> and H<sub>2</sub>S partial pressures, and high chloride concentrations as stated in the supplied datasheet. Table 4 shows standard UNS N08029 chemical composition and minimum PRE number (Pitting Resistance Equivalent) which have been calculated by using equation (2.2).

$$PRE = \%Cr + 3.3 \times \%Mo + 16 \times \%N \quad (3.1.1)$$

**Table 4 Alloy 29 Chemical Composition (nominal) %**

| C      | Si   | Mn   | P      | S      | Cr | Ni   | Mo  | Cu  | N    | PRN |
|--------|------|------|--------|--------|----|------|-----|-----|------|-----|
| ≤0.020 | ≤0.7 | <2.0 | ≤0.020 | ≤0.015 | 27 | 33.5 | 4.4 | 1.0 | ≤0.1 | 42  |

The non-equilibrium diagram by Schaeffler (see Figure 6) could be a valuable equilibrium-phase diagram for predicting the microstructure of an alloy. The alloying components were separated into four groups in the diagram; i) ferrite ii) austenite and iii) martensite iv) duplex alloys. Each group's elements could be expressed as chromium equivalents and nickel equivalents. The microstructures visible in each class of stainless steel are represented by the diagram's regions. Figure 6 confirms imperially that Alloy 29 is super-austenitic stainless steel by using Table 4 chemical composition [1].



### 3.1.2 HEAT TREATMENT PROGRAM

The literature review aimed to optimize number of experimental samples and obtain efficient results. In this experiment ageing temperature has been chosen as 900°C, due to lower precipitation rate at 900 °C compared to 850 °C and 950°C, and minimize aging duration to 0.5 hour [3]. Increasing the aging time will increase secondary phases precipitation along with transformation of  $\chi$ -phase, Laves phase and other carbide phase into the sigma phase [8]. Moreover, the sigma phase has the highest reported kinetic energy at 900°C when aged for 2 h which will be avoided in this HT program of Alloy 29 to obtain best corrosion behavior. Figure 7 shows the experimental path to obtain an optimum heat treatment program. Experiment matrix and flow chart divided into two phases; In the 1<sup>st</sup>

phase of the heat treatment, the samples were annealed at 1200°C for different durations of 30, 60, 90, 120, 180 and 240 min and tagged as A12T30, A12T60, A12T90, A12T120, A12T180 and A12T240, respectively. This phase of HT program was aimed at assessing the effect of annealing duration on corrosion behavior. Thereafter, an optimum duration based on the corrosion evaluation was maintained for the second phase of the annealing HT program. The 2<sup>nd</sup> phase designed for understanding the influence of annealing temperature on the corrosion behavior of alloy 29. The samples were then annealed at different temperatures of 1000, 1100, 1200, and 1300°C for 120 min and then tagged as A10T120, A11T120, A12 T120, and A13T120, respectively. The detailed solution annealing heat treatment program showing the relation between the two phases is schematized in Figure 7. All solution annealed heat-treated samples were quenched in water to room temperature and thereafter aged at 900°C for 0.5h before they were air cooled to room temperature and submitted for further characterization and testing.

In summary, we anticipate significant improvement on the as received alloy 29 samples after applying the heat treatment program. By fixing aging temperature and duration, we anticipate appearance of higher concentration fraction of  $\sigma$ -phase than  $\chi$ -phase, Laves phase and other carbide phases. Moreover, after heat treatment the  $\sigma$ -phase expected to show less concentration fraction at grain interiors as well as grain boundary in comparison with the as received sample. Therefore, mechanical properties shall be reacted accordingly by showing significant reduction in hardness values and better corrosion resistance test performance.

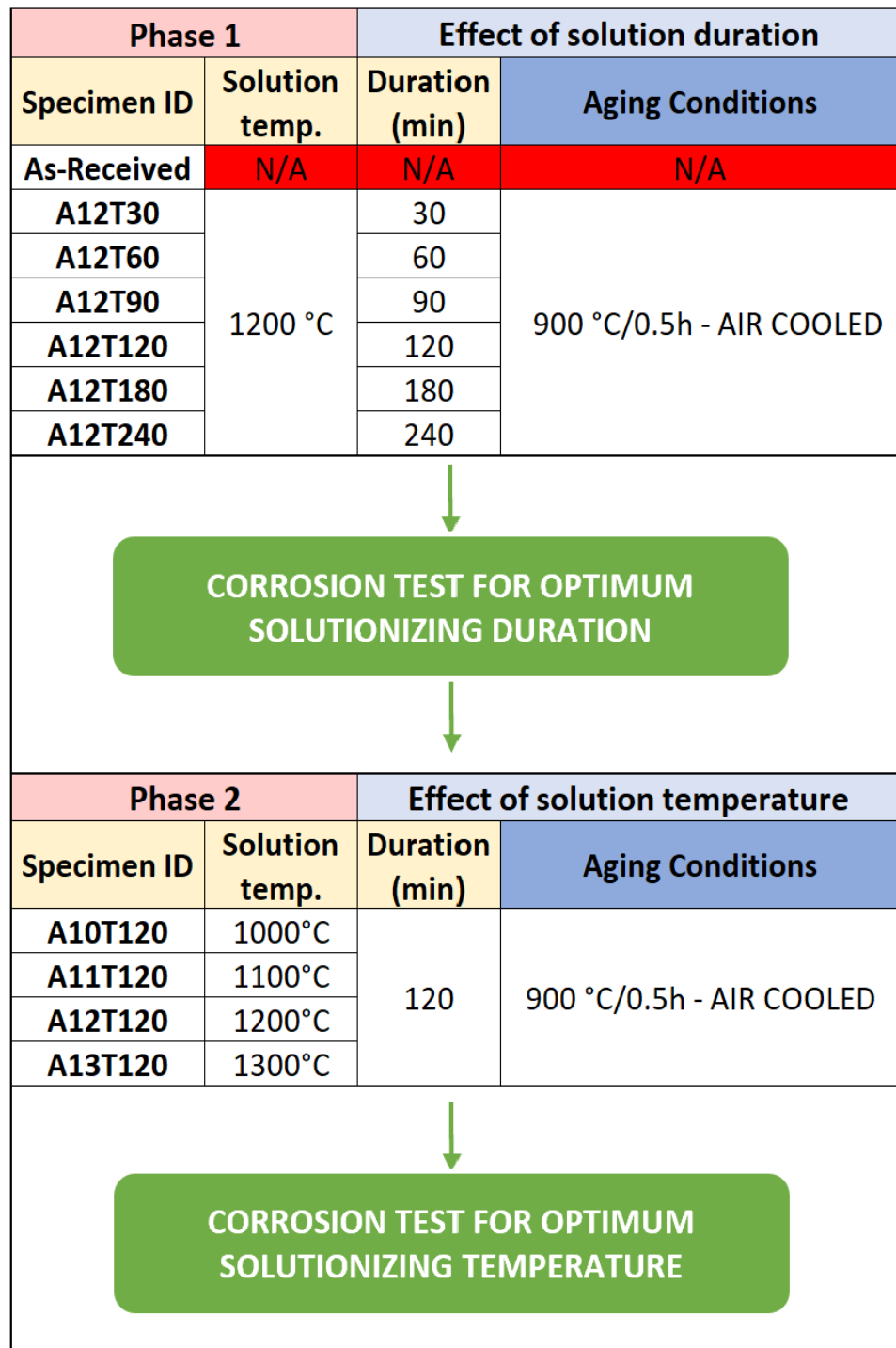


Figure 7 Experimental Matrix and Flow Chart Showing the Sequence of The Heat Treatment and Corrosion Testing

### 3.1.3 SAMPLE PREPARATION & HEAT TREATMENT

Cold hardened super austenitic stainless steel (SASS) was produced with a composition of 26.7 wt% Cr, 32.8 wt% Ni, 4.4 wt% Mo, and 0.9 wt% Cu. After being cut into the necessary size sections, the samples were then solution annealed as illustrated in section (2.3). The solutionizing heat treatment was carried out in a tube furnace (GSI-1700X, MTI, USA) to remove all oxide layers left behind from the heat treatment, all heat-treated samples were grinded using SiC papers with grit sizes ranging from 240 to 800. The samples were then polished to have mirrors-like surfaces in preparation for characterization and corrosion testing.

### 3.1.4 SAMPLE PREPARATION FOR CHARACTERIZATION

The polished samples were electrolytically etched in a solution of sulfuric acid, hydrochloric acid, and ethanol to unveil the microstructure. The optical images were captured using an optical microscope (Video, Microcombi, CMS Instruments, Switzerland), and the measurement of the grain size was carried out using ImageJ image analysis software [16]. An X-ray diffractometer (XRD, Rigaku MiniFlex, Japan) was utilized with Cu  $K_{\alpha 1}$  radiation ( $\lambda = 0.15416$  nm), a tube current of 10 mA, and an accelerating voltage of 30 kV to study the structural changes. The microstructural development resulting from the various heat treatment conditions was examined using an emission scanning electron microscope (SEM, JEOL, Japan) with an accelerating voltage of up to 20 kV coupled with an energy-dispersive X-ray spectroscopy (EDX) silicon drift detector (X-Max<sup>N</sup>, Oxford Instruments, UK).

### 3.1.5 ELECTROCHEMICAL CORROSION MEASUREMENTS

Electrochemical corrosion measurements were conducted to reveal the corrosion behavior and the effect of the adopted heat treatment conditions. A three-electrode system was utilized for the corrosion test wherein the samples served as the working electrode, an Ag/AgCl electrode was used as the reference electrode and a graphite rod was utilized as the counter electrode. For the evaluation of the optimum solutionizing duration and temperature the corrosion behavior of all samples was studied in chloride environments by employing 3.5% (0.6 M) NaCl aerated solution under ambient conditions using a flat sample with a dimension of 30 x 30 x 5 mm. The exposed area for corrosion study is 2.85 cm<sup>2</sup> and an immersion duration of 1 h for the system to attain steady-state condition during which the Open Circuit Potential (OCP) was measured and before the commencement of other electrochemical tests. The electrochemical measurements were conducted using a Gamry potentiostat (Model 600, Gamry, USA). Potentiostatic Electrochemical Impedance Spectroscopy (EIS) measurement was carried out by applying a sinusoidal excitation voltage of  $\pm 10$  mV and acquiring the impedance responses over a frequency range from  $10^5$  to  $10^{-1}$  Hz. Similarly, the Linear Polarization Resistance (LPR) measurement was conducted over a voltage range of  $\pm 25$  mV against the OCP with a scan rate of 0.125 mV/s. The corrosion resistance is directly proportional to the slope of the LPR curve and is often used to estimate the corrosion current density ( $I_{corr}$ ) according to the Stern Geary relationship as in Equation (3.1.5-1) [17], [18]. Accordingly, the polarization resistance ( $R_p$ ) was obtained from the slope of the LPR curves while the  $I_{corr}$  and corrosion rate ( $CR$ ) were then obtained from Equations [3.1.5] 1 and 2, respectively [17], [18].

$$I_{corr} = \frac{\beta_a \beta_c}{2.303 R_p (\beta_a \beta_c)} \quad (3.1.5-1)$$

Where  $R_p$  is the polarization resistance obtained from the LPR slope, and  $\beta_c$  and  $\beta_a$  are the cathodic and anodic Tafel constants taken as  $\pm 0.12$ , respectively.

$$CR = \frac{0.131 \times I_{corr} \times EW}{\rho} \quad (3.1.5-2)$$

Where  $\rho$  is the density, and EW is the equivalent weight of the UN08029 alloy. The Cyclic Potential Dynamic Polarization (CPDP) measurement was carried out as per ASTM standard guidelines [19]. The CPDP test involves perturbing the system from an initial potential of  $-0.5$  V against the OCP with a forward scan rate of  $0.5$  mV/s until an apex current or voltage of  $5$  mA/cm<sup>2</sup> or  $1.5$  V, respectively, whichever is first reached. Then a reverse scanning is conducted at a scan rate of  $0.5$  mV/s until a final potential of  $0.5$  V against the OCP is attained.

The EIS data were fitted with an equivalent circuit (EC) to enumerate the various parameters useful in further understanding the electrochemical behavior of the solutionized samples. The EC consisted of a constant phase element accounting for the non-ideal capacitive behavior of the electrical double-layer ( $CPE_{dl}$ ). The  $CPE_{dl}$  is connected in parallel with the surface resistance to charge transfer ( $R_{ct}$ ). Both  $CPE_{dl}$  and  $R_{ct}$  are further connected serially to the resistance of the oxide films ( $R_f$ ) and a constant phase element ( $CPE_f$ ) which accounts for the capacitive properties of the oxide film. The solution resistance ( $R_s$ ) is connected in series with the  $R_f$  and  $CPE_f$  elements. The EC used in this study is well described as Model C in [20] and it is the most famous EC used to fit EIS

data of stainless steels [21]–[23]. The chi-square or the goodness of fit ( $\chi^2$ ) is usually utilized to assess the agreement between the experimental and simulated data, and the lower the  $\chi^2$  the better the agreement and the more reliable the obtained parameters from the fitting. In general,  $\chi^2$  value of  $10^{-3}$  and lower is accredited to a better quality of the EIS fitting [24]. In this study, the goodness of fit ( $\chi^2$ ) values were found to be about  $10^{-4}$ , which signifies an appropriate equivalent circuit choice. The constant phase element (*CPE*), which has been widely used to model surfaces with oxide films and the numerical relationship is well documented [20], [25], [26]. was employed to account for the deviation from ideal capacitive behavior caused by the heterogeneous nature of the inherent surface oxide film formed on stainless steel when exposed aqueous environment [18]. The electrical impedance of a *CPE* can be calculated according to Equation (3.1.5-3) [18], [20].

$$Z_{CPE} = \frac{1}{Q(\omega i)^n} \quad (3.1.5-3)$$

where  $Q$  is a frequency-dependent real constant ( $\Omega^{-1} s^\alpha$ ),  $n$  is the quantity that represents the deviation from ideal capacitive behavior,  $\omega$  is the angular frequency ( $\omega = 2\pi f \text{ rads}^{-1}$ ). When  $n$  approaches unity, an ideal capacitive behavior is observed and  $Q$  is equivalent to the film capacitance.

## 3.2. RESULTS AND DISCUSSION

### 3.2.1 CHARACTERIZATION OF HEAT-TREATED SAMPLES

Figure 8 shows the optical micrograph and SEM images of the as-received sample that demonstrate the deformed columnar grains produced through the cold-rolling operations. The sample has clearly undergone significant distortion from rolling since the boundary

between the distorted grains is nearly invisible in the vertical direction which making it very difficult to etch the sample.

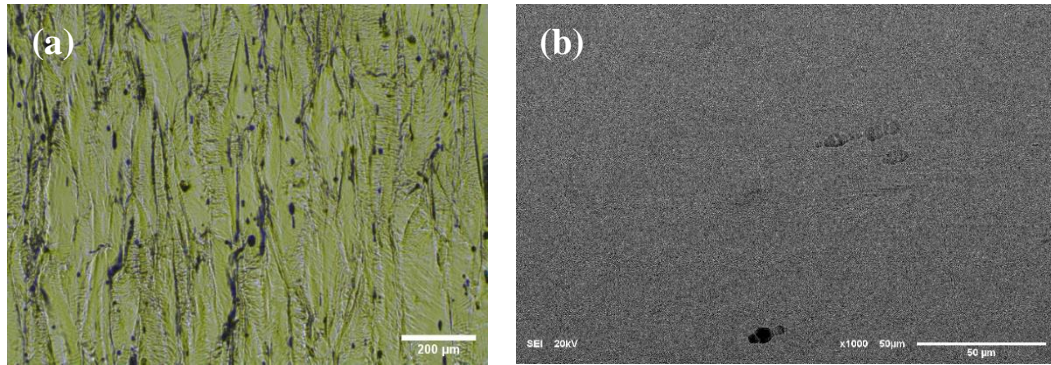


**Figure 8 (a) Optical image (b) SEM image of the as-received (Alloy 29)**

Optical micrographs and their grain sizes distribution of solutionized samples at 1200°C for various durations to investigate temperature effect are presented Figure 9 & Figure 10. The as-received alloy which possesses deformed and elongated grains began to recrystallize into equiaxed grains of various diameters as shown in Figure 9 for (30, 60 and 90 min.) & Figure 10 for (120, 180 and 240 min.) respectively. As shown in both Figure 9 (d-f) & Figure 10 (d-f), which represents the grain size distribution as a function of solutionizing duration, study of various optical micrographs confirms that there is grain expansion that occurs in conjunction with the rise of solution duration.

About 77% of as-received alloy columnar gains are below 99 μm while 23% between 100-199 μm. Equiaxed grains of A12T30, solutionized sample for 30 min. shown about 15% increase in average grain size, consist of around 69% gains below 99 μm, 25% between 100-199 μm and less than 6% grain size between 200-299 μm.

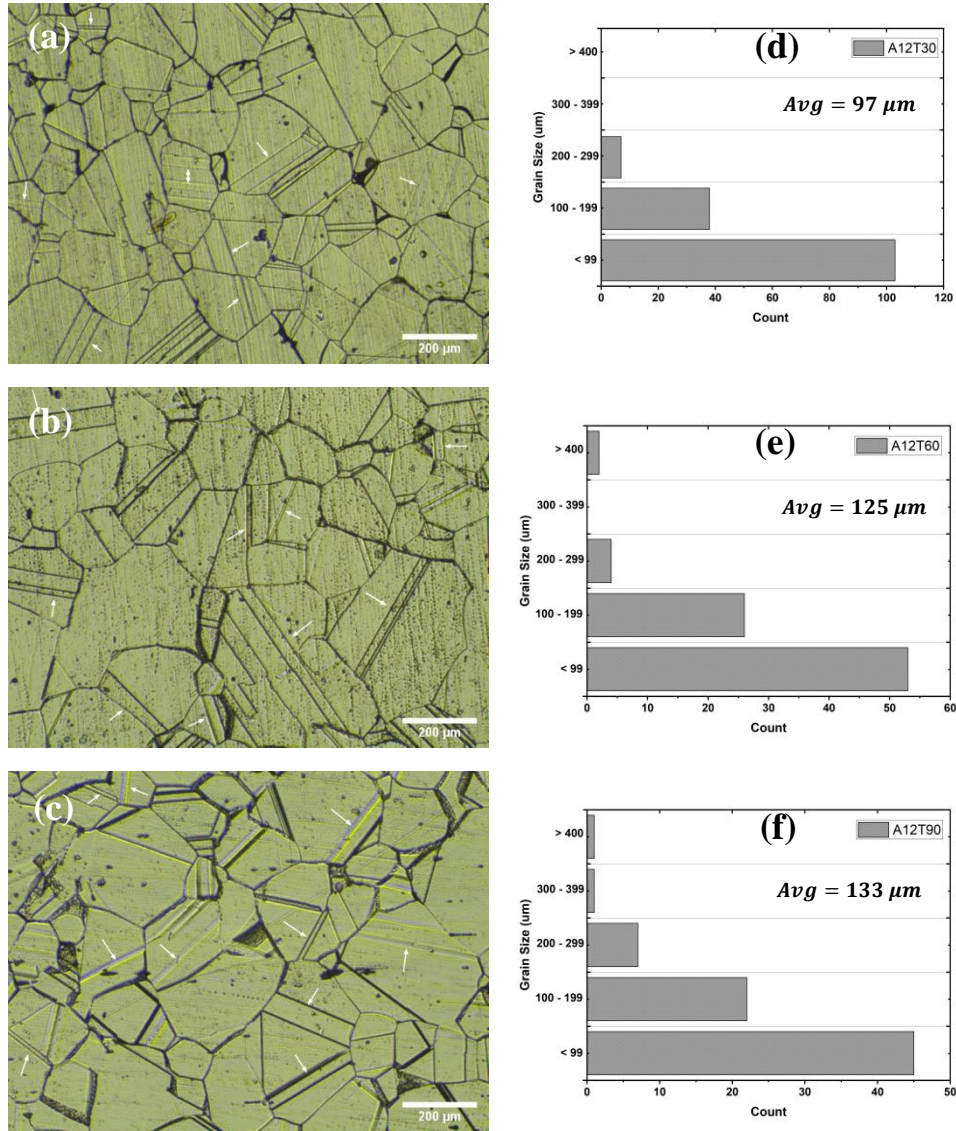


Figure 9 (a-c) Optical images (d-f) grain size distribution of solutionized samples (a,d) A12T30, (b,e) A12T60 and (c,f) A12T90

Higher solutionizing duration of A12T60 & A12T90 resultant further grain size growth about 49% & 58%, respectively in comparison with as-received grains. However, gains below 99 μm are 61% & 59% for A12T60 and A12T90 respectively. Moreover, about 30% grain size between 200-299 for both samples. While grain size more than 200 are 7% & 12% for A12T60 and A12T90 respectively as proven grain boundary growth for heat-treated samples.

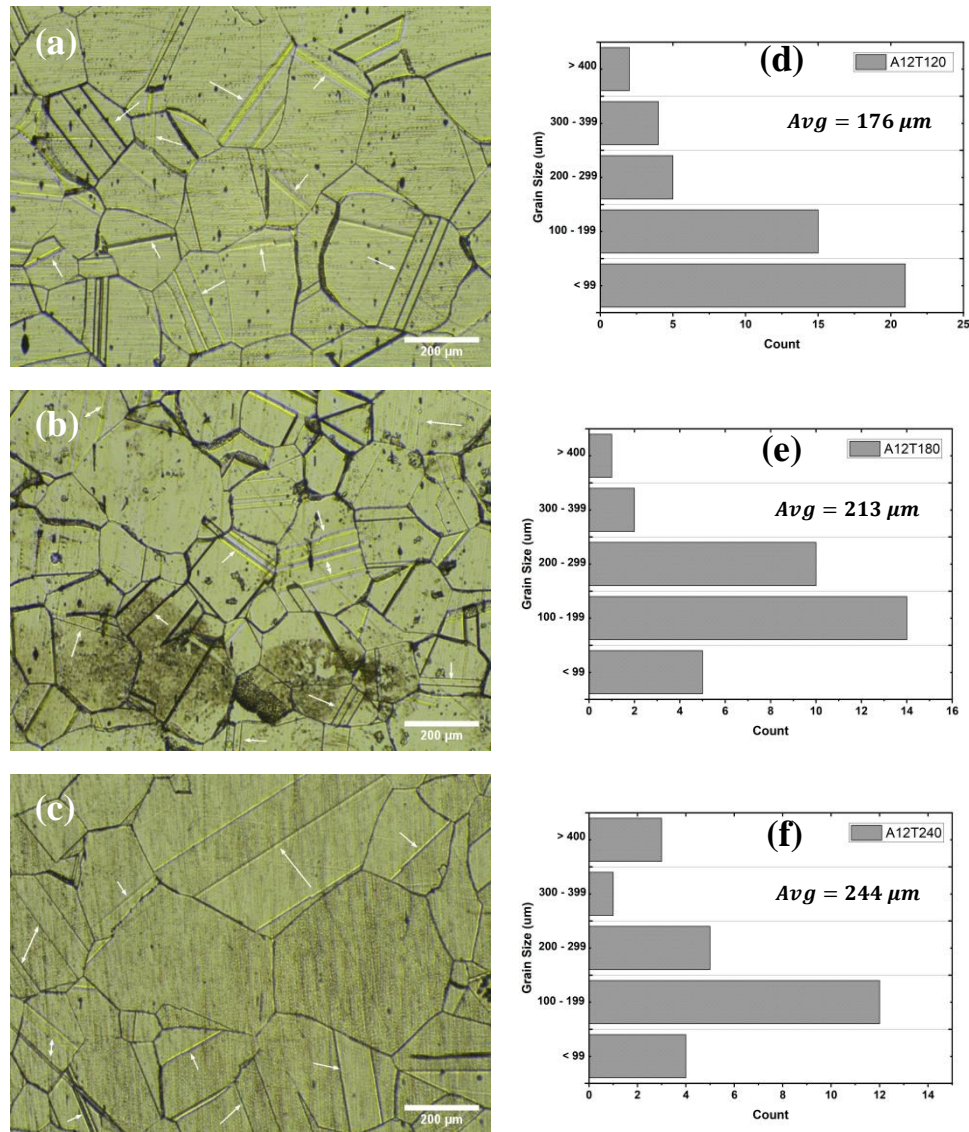


Figure 10 (a-c) Optical images (d-f) grain size distribution of solutionized samples (a,d) A12T120, (b,e) A12T180 and (c,f) A12T240

It is observed that solution annealing for 120 min. (A12T120) have significant impact on average grain size. A12T120 has about 50% & 110% higher average grains than A12T90 and as received samples. Heat-treated sample for 120 min. consists of 45% below 99 μm, 32% between 100-199 μm, 11% between 200-299 μm and 12% higher 300 μm. Similarly, further treatment for 3h (A12T180) and 4h (A12T240) resultant increase of average grain size by 154% & 190% respectively in comparison with as-received. Both samples contain

no more than 16% grains below 99  $\mu\text{m}$ . A12T180 found to have 43% between 100-199  $\mu\text{m}$ , 31% between 200-299  $\mu\text{m}$ , 6% between 300-399  $\mu\text{m}$  and 3% higher than 400  $\mu\text{m}$ . In other hand, a further growth developed in A12T240 sample as it consists of 48% between 100-199  $\mu\text{m}$ , 20% between 200-299  $\mu\text{m}$ , 4% between 300-399  $\mu\text{m}$  and 12% higher than 400  $\mu\text{m}$ . Table 5 summaries the average grain size of as-received and heat-treated samples as function of solutionizing durations. The grain growth with solutionizing duration can be associated with particle coalesce due to increased thermal energy by diminishing the grain boundary area per unit volume [15], [27].

**Table 5 Average grain size of As-received and heat-treated samples as function of solutionizing duration**

| Sample ID   | Average Grain Size ( $\mu\text{m}$ ) | % Change with respect to As-received sample |
|-------------|--------------------------------------|---|
| As-received | 84                                   | -   |
| A12T30      | 97                                   | 15%   |
| A12T60      | 125                                  | 49%   |
| A12T90      | 133                                  | 58%   |
| A12T120     | 176                                  | 110%  |
| A12T180     | 213                                  | 154%  |
| A12T240     | 244                                  | 190%  |

Figure 11(a<sub>1</sub>, b<sub>1</sub>, and c<sub>1</sub>) & Figure 12(a<sub>1</sub>, b<sub>1</sub>, and c<sub>1</sub>) are the SEM images of heat-treated samples. Images show similar grain growth behavior from 30 min to 240 min duration at 1200°C. low magnification images reveal appearance of C- rich precipitates (black) inside the grains as well as at grain boundaries. Solutionized sample for 30 min. (A12T30) has more precipitates concertation as shown in Figure 11(a<sub>1</sub>), while further increment in annealing duration a notable reduction of precipitates inside the grains as shown in Figure 11(b<sub>1</sub>, and c<sub>1</sub>) for A12T60 & A12T90 respectively.

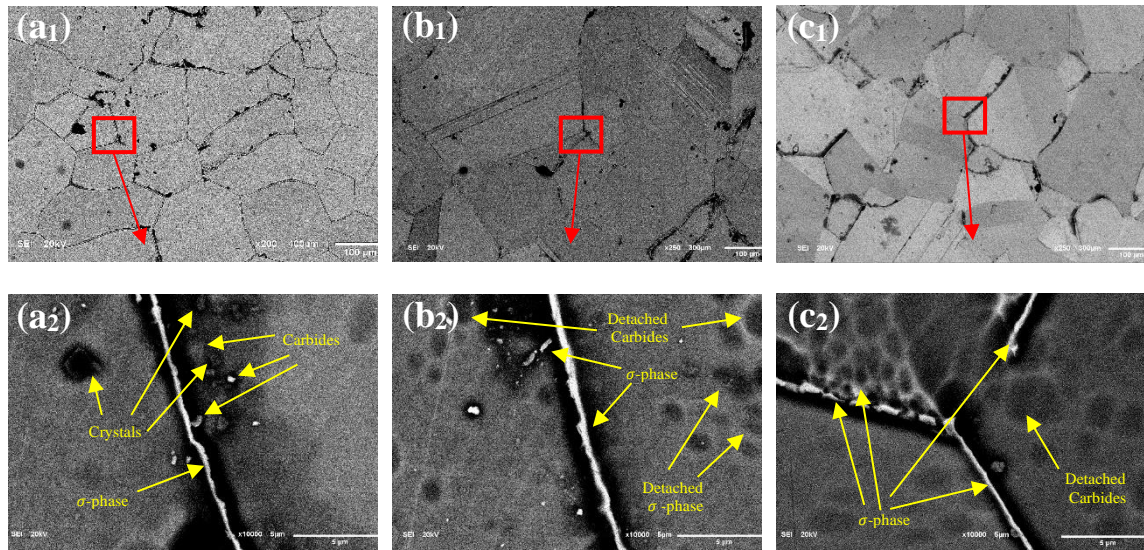


**Figure 11 (a-c) SEM images which reveal grains arrangement of solutionized samples (a<sub>1</sub>,a<sub>2</sub>) A12T30, (b<sub>1</sub>,b<sub>2</sub>) A12T60 and (c<sub>1</sub>,c<sub>2</sub>) A12T90**

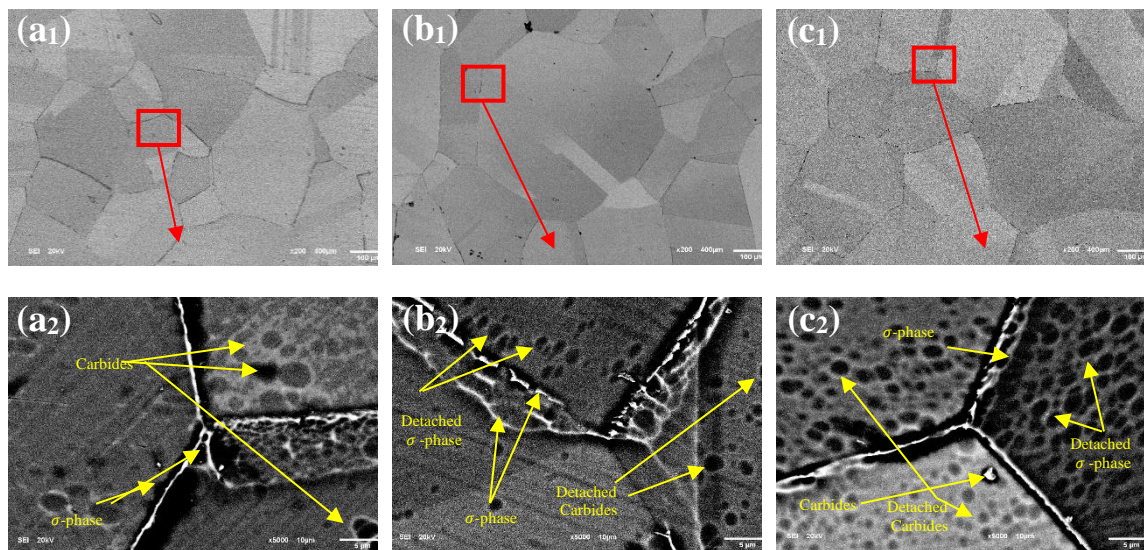


**Figure 12 (a-c) SEM images which reveal grains arrangement of solutionized samples (a<sub>1</sub>,a<sub>2</sub>) A12T120, (b<sub>1</sub>,b<sub>2</sub>) A12T180 and (c<sub>1</sub>,c<sub>2</sub>) A12T240**

In other hand, Figure 12(a<sub>1</sub>,b<sub>1</sub>, and c<sub>1</sub>) shows almost no precipitates inside the grains and not visible at grain boundaries. As seen in Figure 11(a<sub>2</sub>,b<sub>2</sub>, and c<sub>2</sub>) & Figure 12(a<sub>2</sub>,b<sub>2</sub>, and c<sub>2</sub>), the higher-magnification SEM images demonstrated the existence of precipitates. The precipitates tend to separate out in isolation with a granular shape at grain boundaries

primarily (30-60 min), and then grows along the grain boundaries (90 -120 min) as the time goes on. Finally, it starts to arise in grain interiors with a needle-like morphology for sigma phase and spherical morphology for carbide phase (180 – 240 min) when all the grain boundaries are covered with intermetallic phases. This indicates that the transition from intergranular to intragranular precipitation is not an accident but an inevitable result closely related with the material itself. One thing to be noted is that the detailed SEM observation reveals that the phase in grain interiors is, more precisely, lamellar structure rather than needle-like showing the micro-structure interfaces at grain boundaries and in grain interiors, indicate that the intermetallic phase and the austenitic phase, in any cases, adopt an incomplete coherent relationship. This is due to the different crystal structures and lattice constants between the and phases as confirmed by Yan Jiang et al [2]. Additionally, it is well known that the morphology of a new phase formed during a solid-state phase transformation is determined by the competition of interface energy and strain energy, which acts as resistance to nucleation [2]–[7]. For the phase at grain boundaries, the interface between the and phase is noncoherent, where the grain boundary grows from nuclei, which do not have a coherent interface with the matrix, and exhibits no definite orientation with either grain [2]–[7]. As a result, the phase at grain boundaries contains a low density of stacking faults in comparison with lamellar precipitating within the grains, and hence, the precipitation process at grain boundaries is dominated by the interface energy, derived from a high chemical energy change and a low matching degree to form nuclei. In this way, the crystal nucleus of phase here is similar to a sphere [1]–[3]. Due to the criterion of minimum energy path and the effect of boundary diffusion, the nuclei at grain boundaries elongate and thicken quickly and result in isolated particles in consistent

with the experiment result of this work. As for the ones in grain interiors (de-attached carbides and sigma phases), the interface is semi-coherent the elastic strain yielded to sustain the coherent interface finally leads the precipitation process and the nucleus tends to be a thin sheet. Since the nucleus grows along the close alignment direction of matrix, the phase in grain interiors finally have a lamellar structure [1]–[3]. With regard to the phenomenon of the intergranular precipitation occurring prior to the intragranular precipitation, this can be explained by the huge defects in grain boundaries, which can facilitate the precipitation of phase in three ways: firstly, the grain boundaries can act as high-energy nucleation sites and stimulate a lower nucleation energy for the intergranular precipitation as compared to that for the intragranular precipitation [2]–[7]. Furthermore, the grain boundaries can act as a collection plate of solute atoms, which induce the segregation of phase forming elements like Ni, Fe, Cr, Mo in the vicinity of grain boundaries and a higher degree of supersaturation at grain boundaries finally results in an increased nucleation rate of phase. Last but not least, the diffusion rates of phase forming elements within the austenite grains are greatly lower than those along grain boundaries for the abundant vacancies in grain boundaries. All the three reasons make the phase take longer time to nucleate and grow up in grain interiors [2]–[7].

EDX analysis of various precipitates reveal that they are mostly carbides and sigma phase as demonstrated in EDX spectrum samples in Figure 13 (a, b and c) where the average qualitative analysis of elements summarised in Table 6. The carbide is more spherical than the  $\sigma$ -phase, which has a more needle-like form. The sigma phase has a lighter Gray appearance due to its high concentration of Cr and Mo [28].

**Table 6 EDS analysis showing the average elemental composition of the phases for various samples**

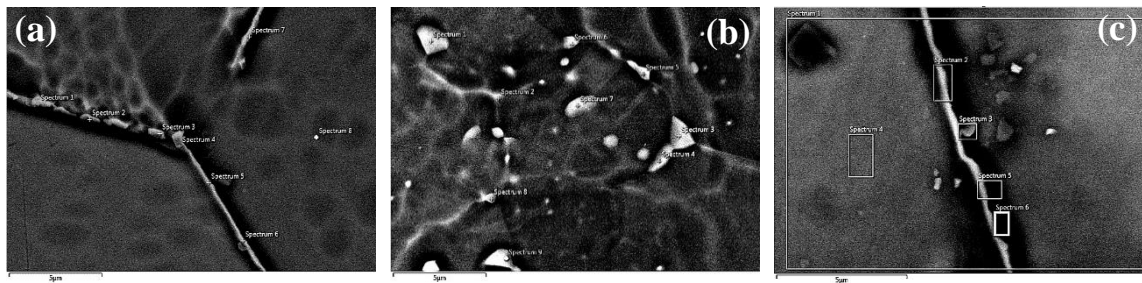
| Phase                   | Cr   | Ni   | Mo   | Fe   |
|-------------------------|------|------|------|------|
| $\gamma$                | 27.7 | 32.8 | 4.5  | 33.9 |
| $\sigma$                | 32.8 | 29.3 | 6.6  | 30.2 |
| Carbide ( $M_{23}C_6$ ) | 35.1 | 19.8 | 12.6 | 30.4 |

Additionally, twin boundaries can be seen in optical micrographs (shown with arrows in Figure 9 ,10 & 14). The twin boundaries are a special case of a large angle grain boundary whereby there is no misalignment of atoms and thus adjacent planes are mirrored across the boundary. The twin boundaries are found to increase with solution inning duration as evident from the optical images as well as from the SEM images in Figure 11 & 12.

Optical micrographs and their grain sizes distribution of heat-treated samples for 2h at various temperatures to investigate duration effect are presented Figure 14. When compared to the microstructure of the as-received sample, the sample solutionized at 1000°C (Figure 14(a-e)) is identical but has larger and clearer defined elongated columnar grain boundaries (shown in Figure 8(a)). This is evidence of the equiaxed microstructure's recrystallization process. Heat-treated sample for 120 min (A10T120) consists of only 17% grain size below 99  $\mu\text{m}$  while as-received sample has 77% at same category. Moreover, a 45% between 100-199  $\mu\text{m}$ , 16% between 200-299  $\mu\text{m}$  and 6% higher than 300  $\mu\text{m}$ . As A10T120 sample has not been recrystallized into equiaxed grains, it should be emphasized that a direct comparison with other solutionized samples is not accurately possible. Hence, the samples that were solutionized at 1100°C, 1200°C, and 1300°C have all been entirely recrystallized, allowing for a comparison of grain size.

As demonstrated in (Figure 14(b-f)), further raising the solutionizing temperature to 1100°C caused the cold role columnar grains to fully recrystallize and become equiaxed with fine & smaller in size grains. Only 7% of grain size between 100-199  $\mu\text{m}$  while remaining 96% are below 99  $\mu\text{m}$ . It is observed that A11T120 is the only solutionized sample has lower average grain size than as-received sample by about 29%. Further increase in annealing temperature resultant in higher grain size as shown in (Figure 14(e,g)) & (Figure 14(d,h)) for A12T120 and A13T120 respectively. As mentioned earlier, Heat-treated sample for 120 min at 1200°C. consists of 45% below 99  $\mu\text{m}$ , 32% between 100-199  $\mu\text{m}$ , 11% between 200-299  $\mu\text{m}$  and 12% higher 300  $\mu\text{m}$ . Whereas, annealing for 1300°C have 29% below 99  $\mu\text{m}$ , 25% between 100-199  $\mu\text{m}$ , 19% between 200-299  $\mu\text{m}$  and 29% higher than 300  $\mu\text{m}$ .

Obtained grain size of A13T120 sample is shows an increase of average grain size by 218% & 52% in comparison with as-received and A12T120 respectively. Table 7 summaries the average gain size of as-received and heat-treated samples as function of solutionizing temperature. In addition, at a constant dwell duration of 120 min, an increase in the solutionizing temperature will induce an increase in the thermodynamic driving force and kinetic activation energy which accelerate grain coalesces and growth [2].



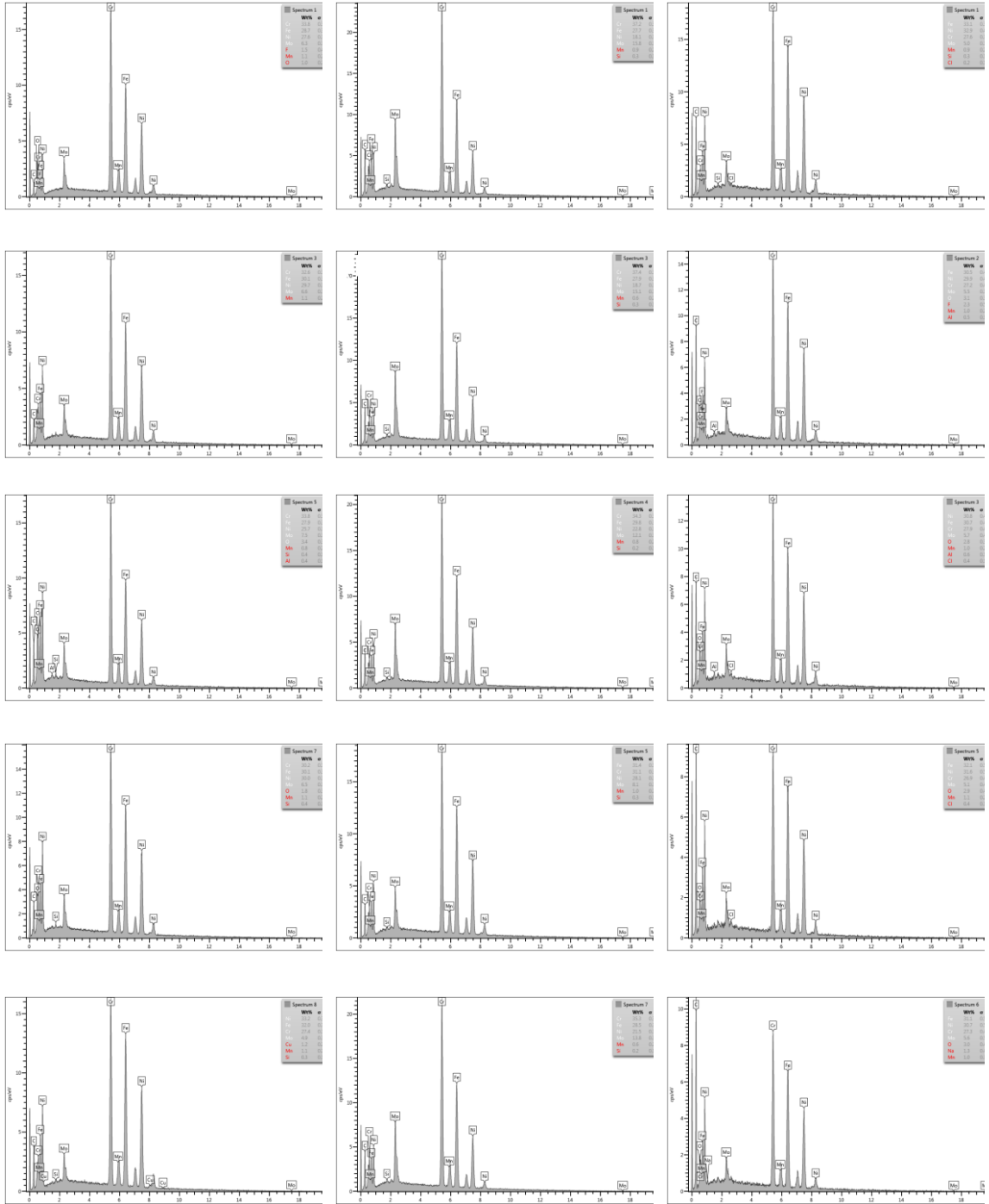


Figure 13 Sample EDX spectrum detail of solutionized samples (a) A12T90, (b) A10T120 and (c) A12T30

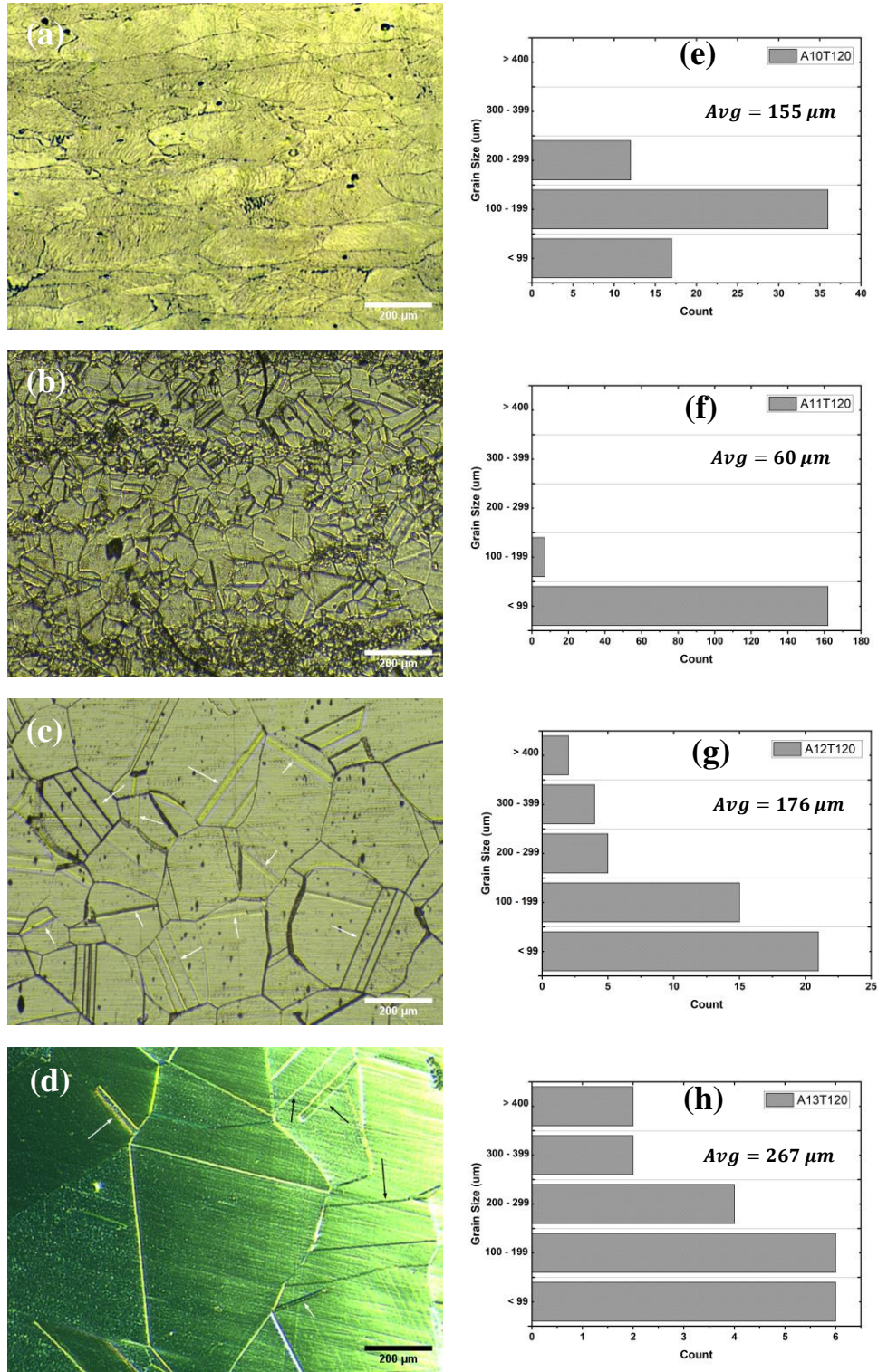


Figure 14 (a-d) Optical images (d-h) grain size distribution of solutionized samples (a,e) A10T120, (b,f) A11T120, (c,g) A12T120 and (d,h) A13T120

Generally, a lower heat-treatment temperature results in a smaller solid solubility of the precipitate and a higher degree of supercooling. a decreased heat-treatment temperature for a same alloy will stimulate a higher degree of supersaturation and a smaller critical nucleation radius, hence a higher nucleation rate for the precipitate as evidently shown in Figure 14(a-b) for solutionizing temperature of 1000°C and 1100°C, respectively. Thus, higher degree of supercooling is inversely proportional to grain size and growth as such.

**Table 7 Average grain size of As-received and heat-treated samples as function of solutionizing temperature**

| Sample ID   | Average Grain Size ( $\mu\text{m}$ ) | % Change with respect to As-received sample |
|-------------|--------------------------------------|---|
| As-received | 84                                   | -   |
| A10T120     | 155                                  | 85%   |
| A11T120     | 60                                   | -29%  |
| A12T120     | 176                                  | 110%  |
| A13T120     | 267                                  | 218%  |

Higher temperature improves the effect of grain boundary migration due to increased thermal energy and thus more recrystallization is observed as the solutionizing temperature is increased [15], [27]. Furthermore, after a close observation of the optical images, it is interesting to note that the sample solutionized at 1200°C possessed the largest number of twin boundaries as compared to all the solutionized samples as seen in Figures (9,10 &14). Twin boundaries are known for their very low energy due to their high degree of order at the interface, providing some superior properties compared to random high-angle grain boundaries [29].

Figure 15(a<sub>1</sub>,b<sub>1</sub>, and c<sub>1</sub>) is the SEM images of heat-treated samples for temperature effect investigation. Figure 15(a<sub>2</sub>), which displays high magnification SEM images of sample A10T120, reveals various particle-like partials that can be classified as sub-grains or small crystals within the elongated columnar grains Figure 15(a<sub>1</sub>). Most of the time, these tiny crystals are developed during the high-temperature recovery stage [30]. The crystals

coalesce to create bigger and recrystallized grains as the solutionizing temperature rises. The crystals are clearly fully equiaxed at a higher solutionizing temperature of 1200°C, as seen in Figure 12(a<sub>1</sub>, a<sub>2</sub>) for A12T120, and they continue to develop with rising temperature, as shown in Figure 15(c<sub>1</sub>, c<sub>2</sub>) for A13T120. In other hand, A11T120 annealed sample for 1100°C might be the starting equiaxed recrystallization temperature. It's noteworthy that secondary phases of the carbide and  $\sigma$  phases can be seen precipitating at higher solutionizing temperatures in Figure 15(c<sub>1</sub>, c<sub>2</sub>). This seems to occur more frequently at higher temperatures. According to Zhiying Mo et al., greater annealing temperatures result in faster recrystallization rates, more movable grain boundaries, quicker grain growth, and larger recrystallized grain sizes [30].

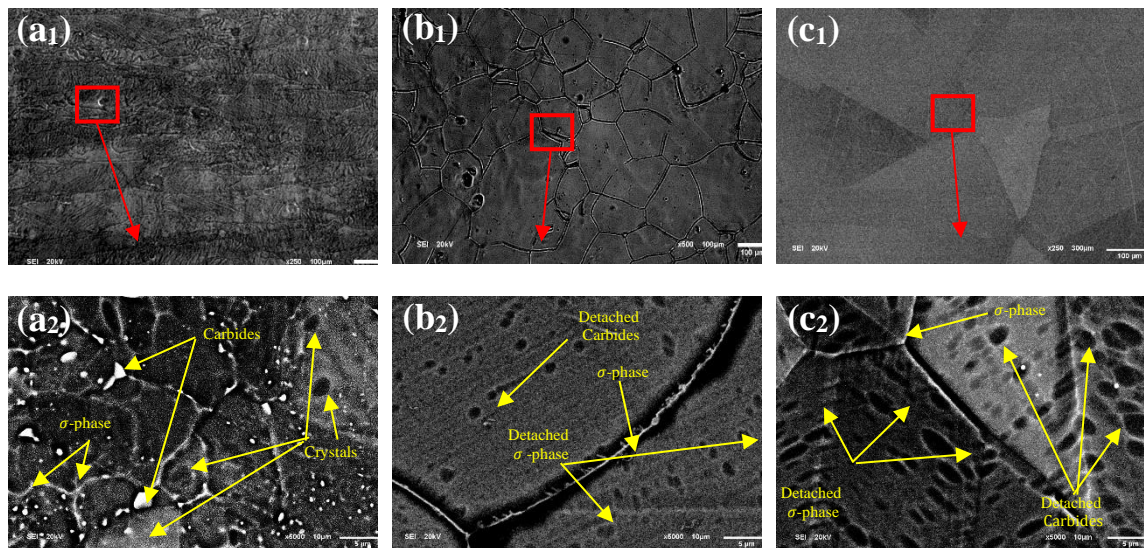


Figure 15 (a-c) SEM images which reveal grains arrangement of solutionized samples (a<sub>1</sub>,a<sub>2</sub>) A10T120, (b<sub>1</sub>,b<sub>2</sub>) A11T120 and (c<sub>1</sub>,c<sub>2</sub>) A13T120

The EDS analysis of the precipitates on the grain boundaries as shown in Figure 13(b) shows that the deposits are mainly carbides, besides crystals and sigma phase. Figure 13(c) spectrums are evidence that despite presence of precipitations, the chemical composition of about a 1  $\mu\text{m}^2$  and higher are mainly  $\gamma$ -Phase. XRD charts shown in Figure 16 and 17

confirm the findings of EDS and microstructure analysis. The cubic crystal structure peaks at angles (around  $43^\circ$ ,  $51^\circ$  &  $75^\circ$ ) are related to  $\gamma$ -Phase while other randomly distributed peaks are precipitates of both carbides and sigma phases. At higher solutionized temperature and duration samples (specifically A13T120 and A12T240), peaks at  $43^\circ$  &  $75^\circ$  angles are almost completely diminished with large intensity value at about  $51^\circ$  angle [2].

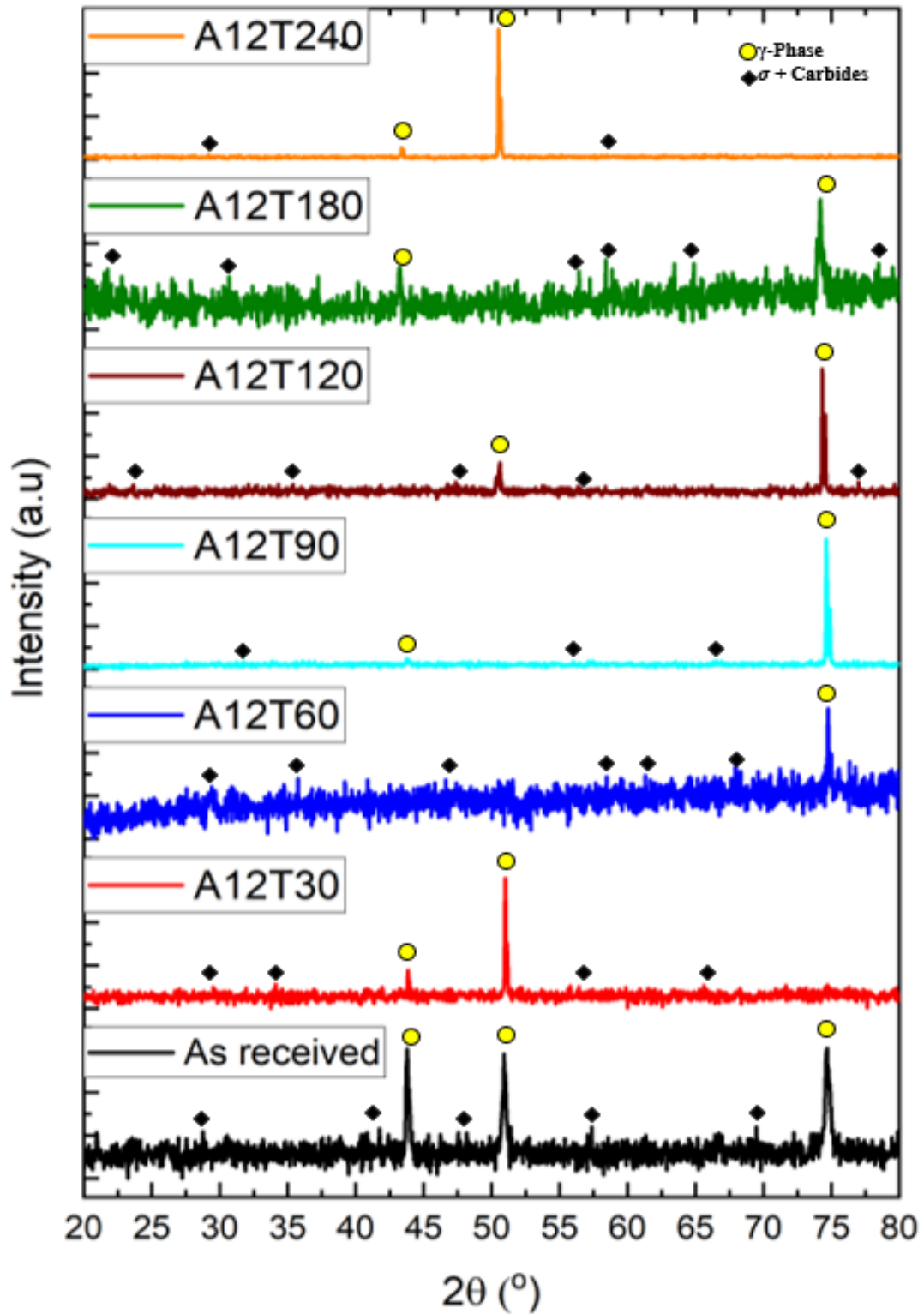


Figure 16 XRD patterns obtained from heat-treated specimen showing the effect of solutionizing duration

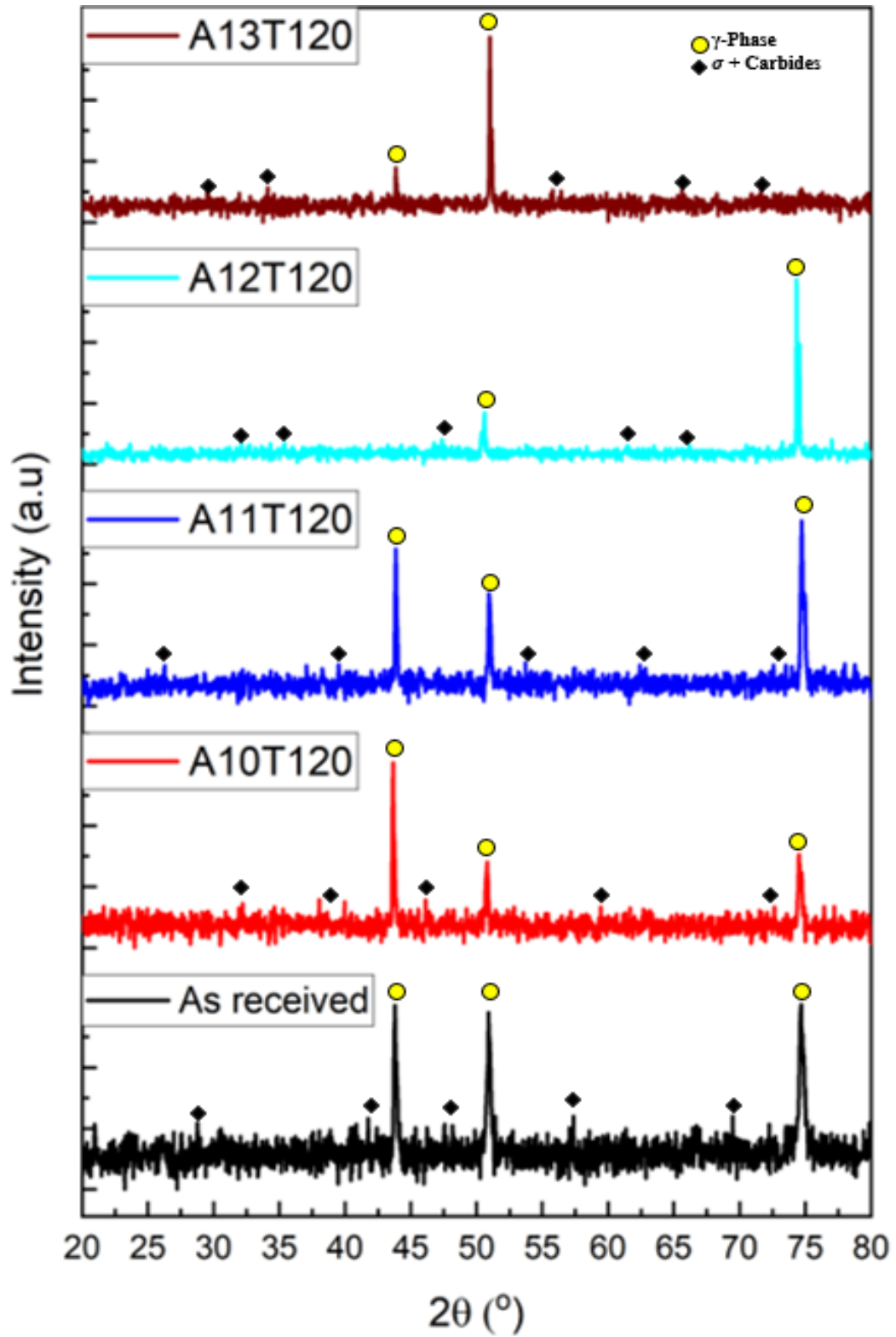
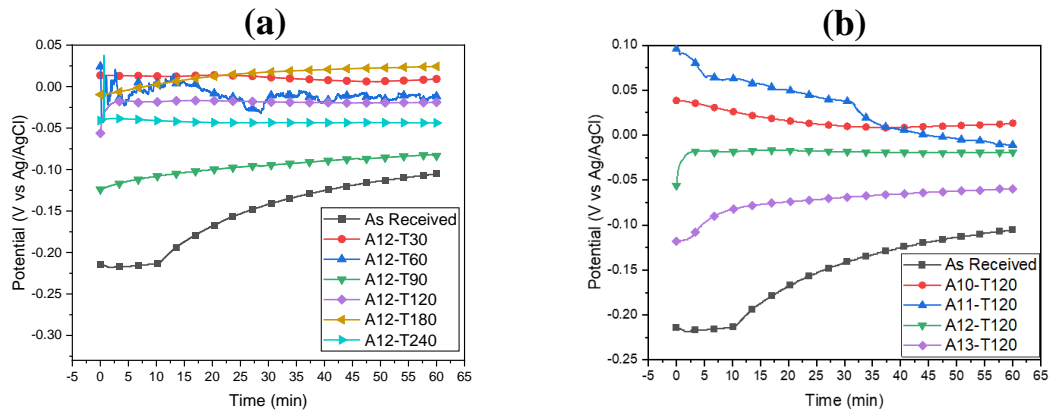


Figure 17 XRD patterns obtained from heat-treated specimen showing the effect of solutionizing temperature

### 3.2.2 ELECTROCHEMICAL CORROSION OF HEAT-TREATED SAMPLES

#### A) OPEN CIRCUIT POTENTIAL (OCP) MEASUREMENT

The OCP measurement was used to monitor the unperturbed corroding potential of the sample when no external current was applied, and the system is expected to attain a steady-state condition when the potential is no longer a function of the immersion duration. Thus, the OCP shows the stability of the electrochemical environment before polarizing the system and it also provides information about the thermodynamic tendency of the samples towards corrosion. The OCP of the solutionized samples is shown in Figure 18 and it is evident that the samples attained an equilibrium state after the monitoring duration of 1 h.



**Figure 18 (a) Open circuit potentials showing the effect of solutionizing duration and (b) solutionizing temperature on the corrosion behavior of N08029 after 1 h immersion in 3.5 % NaCl aerated solution.**

Figure 18(a) shows the OCP trend of the samples solutionized for different durations (30 to 240 minutes), it is seen that the samples attain an equilibrium state and exhibited a nobler potential in comparison to the As-Received alloy. Furthermore, the potential of the sample A120T180 is noblest and as the solutionized duration increase from 30 to 240 minutes, the potential reduces from + 24.3 to -83.4 mV as compared to a potential of -105 mV of the As-Received alloy at the end of 1h monitoring duration.

A similar trend is observed for the samples solutionized at different temperatures (1000°C to 1300°C) as shown in Figure 18(b) sample solutionized at 1000°C (A10T120) shows the noblest potential (+13.2 mV) and increasingly becomes active (less noble) with solutionizing temperatures. The most active sample (sample A13T120) showed a potential of -59.8 mV as compared to sample As-Received which exhibited a stable potential of -105 mV at the end of 1h monitoring duration. Besides, the trend in the OCP can also be related to the formation of the passive film. The lower and increasing OCP with time for the As-Received sample indicates the incremental film formation over time. However, the solutionized samples mostly showed a steady OCP over a wide duration indicating the early formation of the film and its stability and protectiveness. Generally, the degree of the nobility of the OCP after attaining equilibrium indicates the inertness of the sample and hence the lower the corrosion propensity in the test environment.

## B) LINEAR POLARIZATION RESISTANCE (LPR) MEASUREMENT

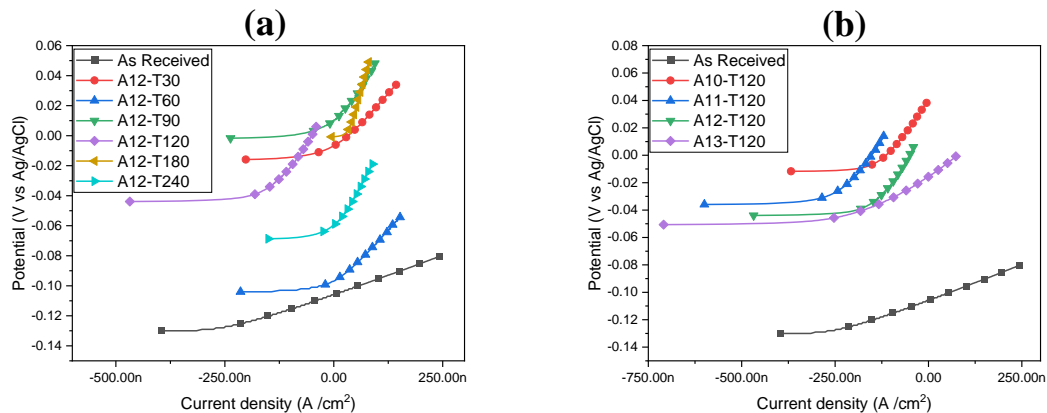


**Figure 19 LPR curves showing the effect of (a) solutionizing duration and (b) solutionizing temperature on the corrosion behavior of N8029 after 1 h immersion in 3.5 % NaCl aerated solution.**

Figure 19 shows linear polarization resistance (LPR) plots for the As-Received and solutionized samples. From the LPR curves, it can be observed that all the solutionized

samples possessed higher corrosion resistance as compared to the As-Received cold rolled UN08029 alloy as evident from the steepness of the slope of the potential vs current curves. The parameters  $R_p$ ,  $I_{corr}$ , and  $CR$  for the samples obtained from the LPR measurement are shown in Tables 8 and 9 showing the effects of solutionizing duration and temperatures, respectively. All the solutionized samples demonstrated a higher slope thus larger  $R_p$  and consequently lower  $I_{corr}$  and  $CR$  than the As-Received alloy. As seen from Table 8, as the solutionizing duration increases from 30 to 240 min, the  $R_p$  increases. This necessitates a corresponding reduction in the current density and corrosion rate with an increase in the solutionizing duration. The  $R_p$  of the untreated alloy sample was increased by about 65, 67, 69, 75, 72 and 80 % after solutionizing for a duration of 30, 60, 90, 120, 180 and 240 minutes, respectively, as estimated from the resistive efficiency ( $\mathcal{E}_{lpr}$ ) according to the LPR measurement. Though there is an appreciable increase in the  $R_p$  when compared to the As-Received sample, the increment among the solutionized samples is not that significant, especially for the duration between 30,60 and 90 minutes as the grain size distribution is fairly similar (see Figure 9). The increasing corrosion resistance behavior can be associated with the microstructure of the samples after solutionizing for the different duration as shown in Figures 9 and 10. An increase in the grain size with solutionizing duration reduces the grain boundary defects and thus improves the corrosion resistance.

**Table 8 LPR parameters for the samples solutionized for different durations**

| Sample ID   | $I_{corr}$ ( $\mu\text{A}/\text{cm}^2$ ) | $E_{corr}$ (mV) | CR (mpy) | $R_p$ ( $\text{k}\Omega\cdot\text{cm}^2$ ) | $\mathcal{E}_{lpr}$ (%) |
|-------------|--|-----------------|----------|--|-------------------------|
| As-Received | 0.090                                    | -105.9          | 0.041    | 101.800                                    | -                       |
| A12T30      | 0.031                                    | -6.74           | 0.013    | 311.800                                    | 65.6%                   |
| A12T60      | 0.030                                    | -96.96          | 0.014    | 315.450                                    | 66.7%                   |
| A12T90      | 0.028                                    | -85.06          | 0.013    | 321.700                                    | 69.2%                   |
| A12T120     | 0.022                                    | 5.73            | 0.010    | 408.200                                    | 75.1%                   |
| A12T180     | 0.025                                    | -0.7768         | 0.011    | 368.800                                    | 72.4%                   |
| A12T240     | 0.018                                    | -59.59          | 0.008    | 521.700                                    | 80.5%                   |

**Table 9 LPR parameters for the samples solutionized for different temperatures**

| Sample ID   | $I_{corr}$ ( $\mu\text{A}/\text{cm}^2$ ) | $E_{corr}$ (mV) | CR (mpy) | $R_p$ ( $\text{k}\Omega.\text{cm}^2$ ) | $\mathcal{E}_{lpr}$ (%) |
|-------------|--|-----------------|----------|--|-------------------------|
| As-Received | 0.090                                    | -105.9          | 0.041    | 101.800                                | -                       |
| A10T120     | 0.025                                    | 38.15           | 0.011    | 381.100                                | 73.1%                   |
| A11T120     | 0.026                                    | 13.7            | 0.012    | 364.900                                | 71.2%                   |
| A12T120     | 0.022                                    | 5.73            | 0.010    | 408.200                                | 75.1%                   |
| A13T120     | 0.052                                    | -15.73          | 0.024    | 174.800                                | 41.7%                   |

Though there are precipitated carbide and sigma phases as observed in Figure 11 and 12, this does not seem to affect the corrosion behavior of this alloy. This may be attributed to the substantial availability of Cr, Mo, and Ni in the matrix (as seen in Table 6 and EDS spectrums in Figure 13(c)), which are instrumental in the corrosion resistance property, so the matrix was not detrimentally depleted of these elements for the formation of the secondary phases. The LPR parameters for the sample solutionized at different temperatures are shown in Table 9 and the  $I_{corr}$  and CR are lower for the solutionized samples with sample A12T120 exhibiting the lowest values. Also, it is seen that the  $R_p$  of the untreated alloy sample was increased by about 73, 71, 75, and 42 % after solutionizing at temperatures of 1000°C, 1100°C, 1200°C, and 1300°C, respectively, as enumerated from the  $\mathcal{E}_{lpr}$ . The obtained resistive efficiency of 73 % for sample A10T120 decreases slightly by 2% for A11T120 and then increase until 75% for 1200°C and then drops to about 42 % at 1300°C (A13T120).

Similarly, the increased corrosion resistance with increasing solutionizing temperature can be linked to the grain size growth as evident from Figure 14. However, the reduction in the corrosion behavior at a temperature of 1300°C may be attributed to the increased growth and coalesces of secondary phases in the matrix as well as wider grain boundaries of carbides and sigma phases as shown in Figure 12(b,c) and Figure 15(c).

## C) CYCLIC POTENTIODYNAMIC POLARIZATION (CPDP) MEASUREMENT

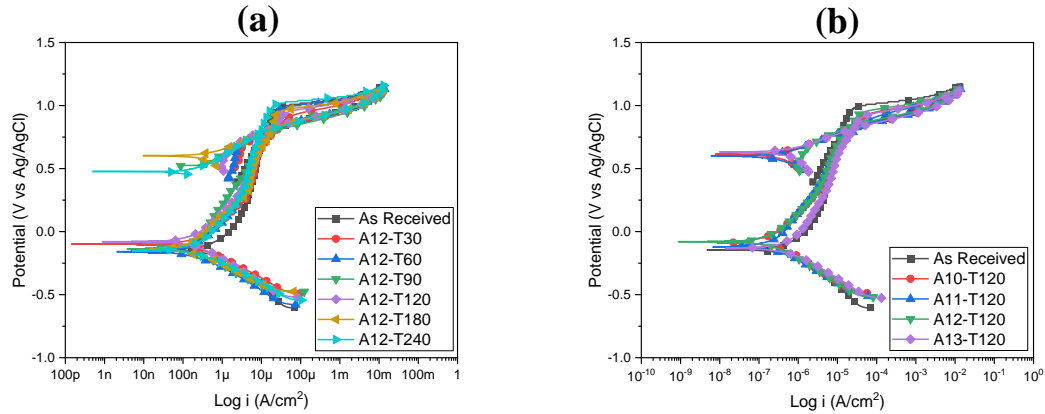


**Figure 20** CPDP curves showing the effect of (a) solutionizing duration and (b) solutionizing temperature on the corrosion behavior of N8029 after 1 h immersion in 3.5 % NaCl aerated solution.

The CPDP measurement also revealed important corrosion characteristics of the As-Received and solutionized samples. Tafel extrapolation method was employed to obtain the corrosion potential ( $E_{corr}$ ) and corrosion current density ( $I_{corr}$ ) from which the corrosion rate ( $CR$ ) was calculated. The CPDP plots for the solutionized samples are shown in Figure 20 and they exhibited both active and passive behavior at various polarizing potentials. The parameters  $E_{corr}$ ,  $I_{corr}$ , and the  $CR$  quantify the general corrosion behavior of the samples while the pitting potential ( $E_{pit}$ ), passivation current density ( $I_p$ ), and the repassivation or protection potential ( $E_p$ ) are essential parameters for quantifying the localized pitting corrosion behavior of the samples [19], [31]. The  $E_{pit}$  is defined as the potential at which the surface passive film breakdown occurs as indicated by the rapid increase in the current in the active-passive region [19], [31], [32]. For a better insight into the film breakdown, the  $I_p$  was determined as the corresponding current density at which the surface film breakdown occurs. While the  $E_p$  is defined as the potential in the reverse scan direction when repassivation occurs or the hysteresis loop (approximated to  $E_{pit} - E_p$ ) is completed (i.e. when the reverse scan intercepts the forward scan) [31]. Figure 20(a) is the CPDP plot

for the samples solutionized for different time duration and it can be seen that all the samples exhibited similar behavior. However, all the solutionized samples were shifted lower current density while the  $E_{corr}$  of the samples A12T30 and A12T120 becomes nobler as compared to the As-Received sample. Subsequently, the solutionized samples showed higher potential at any given current density almost throughout the passive region. Though the  $E_{pit}$  for the As-Received sample is slightly higher than for the solutionized samples, a closer look into the hysteresis loop shows that the loop size in the decreasing order of A12T30 < A12T120 < A12T60 < A12T90 < A12T180 < A12T240 < As-Received. The lower the hysteresis loop the faster the repassivation and lesser the damage due to pitting corrosion on the sample. Table 10 shows the quantitative CPDP parameters for the solutionized samples for a different duration. It is evident from the table that the  $I_{corr}$  and consequently  $CR$  decreases necessitating an increase in resistance efficiency ( $\mathcal{E}_{cp}$ ) with solutionizing duration and consonant with the LPR findings. The  $E_{pit}$ ,  $I_p$ , and  $E_p$  values which quantify the pitting corrosion behavior show that the As-Received sample exhibited the second highest  $E_{pit}$  and lowest  $I_p$ , however, it has the lowest  $E_p$  values. This indicates that though the pitting potential is the second highest and occurs at a lower current density repassivation is somewhat delayed which means more pitting corrosion damage to the sample. Additionally, A12T240 exhibited the highest  $E_{pit}$  and highest  $I_p$ , however, it has the highest  $E_p$  values which indicates that though the pitting potential and repassivation potential are the highest, but occurs at the highest current density repassivation which means more pitting corrosion damage to the sample. Based on the repassivation capability, samples A12T30 and A12T120 possessed improved repassivation tendency which result in a lesser pitting damage, especially considering that their  $I_p$  values are just barely higher

than that of the As-Received sample. Similarly, the CPDP plots for the samples solutionized at different temperatures are shown in Figure 20(b) and the  $E_{corr}$  of the solutionized samples shifted to the noble positive potentials with correspondingly lower  $I_{corr}$ . This behavior shows that all the samples solutionized at different temperatures exhibited improved resistance against general corrosion in comparison with the As-Received sample. Furthermore, for the pitting behavior, the As-Received sample offered the highest  $E_{pit}$  and lowest  $I_p$  just as observed with the samples solutionized for a different duration. However, the hysteresis loop of s As-Received ample can be seen to be the largest due to it having the lowest  $E_p$  value. Interestingly, the hysteresis loop for the solutionized samples is almost overlapping and the  $E_p$  is only slightly different. The  $E_{corr}$ ,  $I_{corr}$ , and  $\mathcal{E}_{cp}$  parameters alongside the pitting corrosion parameters for these samples are given in Table 11. The  $\mathcal{E}_{cp}$  parameter can be seen to be within a close range between 75 and 81 % with the solutionizing temperature and then sharply drops to 52 % for the sample solutionized at 1300°C (A13T120). The samples can be ranked according to increasing  $E_{pit}$  thus; As-Received > A12T120 > A11T120 > A10T120 > A13T120 while the hysteresis loop can be ranked in the increasing order thus: As-Received > A10T120 > A12T120 > A13T120 > A11T120. It should be noted that the sample with a high  $E_{pit}$  and a low hysteresis loop will demonstrate superior pitting resistance. Thus, it can be proposed that sample A12T120 showed an optimum combination of both  $E_{pit}$  and relatively low hysteresis loop, thus will suffer less from pitting corrosion damage.

**Table 10 Tafel extrapolation and pitting parameters obtained from the CPDP measurement for the samples heat-treated at different solutionizing durations**

| Sample ID   | $\beta_a$<br>(mV/dec) | $\beta_c$<br>(mV/dec) | $I_{corr}$<br>( $\mu\text{A}/\text{cm}^2$ ) | $E_{corr}$<br>(mV) | CR<br>(mpy) | $\mathcal{E}_{cp}$<br>(%) | $E_{pit}$<br>mV | $I_p$<br>( $\mu\text{A}/\text{cm}^2$ ) | $E_p$<br>(mV) | $E_{pit}-E_p$<br>(mV) |
|-------------|-----------------------|-----------------------|---|--------------------|-------------|---------------------------|-----------------|--|---------------|-----------------------|
| As-Received | 572.8                 | 276.8                 | 0.34  | -144               | 0.157       | -                         | 943.9           | 6.86                                   | 794.6         | 149.3                 |
| A12T30      | 272.7                 | 145.2                 | 0.11  | -103               | 0.033       | 68.6%                     | 872.9           | 12.59                                  | 823.5         | 49.4                  |
| A12T60      | 281.4                 | 145.7                 | 0.10  | -162               | 0.024       | 70.4%                     | 904.3           | 9.06                                   | 820           | 84.3                  |
| A12T90      | 350.2                 | 180.9                 | 0.09  | -145               | 0.023       | 73.3%                     | 906.9           | 12.49                                  | 821.9         | 85                    |
| A12T120     | 322.8                 | 172.6                 | 0.07  | -82.9              | 0.020       | 80.7%                     | 892.5           | 10.00                                  | 831.6         | 60.9                  |
| A12T180     | 330.2                 | 128.0                 | 0.07  | -146               | 0.023       | 78.7%                     | 909.8           | 7.79                                   | 819.8         | 90                    |
| A12T240     | 349.2                 | 134.6                 | 0.05  | -151               | 0.019       | 84.4%                     | 996.7           | 44.70                                  | 865.7         | 131                   |

**Table 11 Tafel extrapolation and pitting parameters obtained from the CPDP measurement for the samples heat-treated at different solutionizing temperatures**

| Sample ID   | $\beta_a$<br>(mV/dec) | $\beta_c$<br>(mV/dec) | $I_{corr}$<br>( $\mu\text{A}/\text{cm}^2$ ) | $E_{corr}$<br>(mV) | CR<br>(mpy) | $\mathcal{E}_{cp}$<br>(%) | $E_{pit}$<br>mV | $I_p$<br>( $\mu\text{A}/\text{cm}^2$ ) | $E_p$<br>(mV) | $E_{pit}-E_p$<br>(mV) |
|-------------|-----------------------|-----------------------|---|--------------------|-------------|---------------------------|-----------------|--|---------------|-----------------------|
| As-Received | 572.8                 | 276.8                 | 0.34  | -144               | 0.157       | -                         | 943.9           | 6.86                                   | 794.6         | 149.3                 |
| A10T120     | 389.1                 | 189.0                 | 0.08  | -86.7              | 0.022       | 77.5%                     | 883.3           | 11.45                                  | 814.7         | 68.6                  |
| A11T120     | 466.5                 | 175.1                 | 0.09  | -122               | 0.024       | 75.1%                     | 883.7           | 22.85                                  | 830.5         | 53.2                  |
| A12T120     | 322.8                 | 172.6                 | 0.07  | -82.9              | 0.020       | 80.7%                     | 892.5           | 10.00                                  | 831.6         | 60.9                  |
| A13T120     | 538.0                 | 204.4                 | 0.16  | -133               | 0.047       | 52.6%                     | 867.8           | 11.27                                  | 811.8         | 56                    |

**D) ELECTROCHEMICAL IMPEDANCE SPECTROSCOPY (EIS) MEASUREMENT**

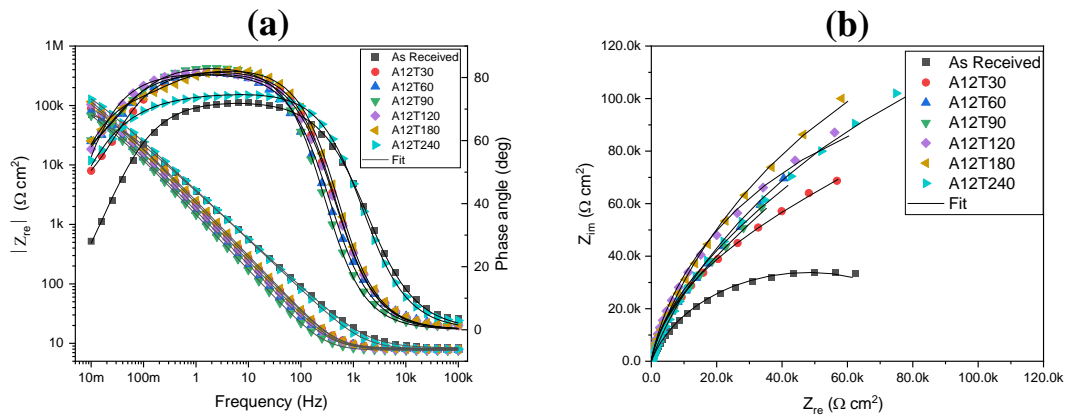


**Figure 21 EIS plots, (a) Modulus and phase angle, and (b) Nyquist plots, showing the effect of solutionizing duration on the corrosion behavior of N08029 after 1 h immersion in 3.5 % NaCl aerated solution.**

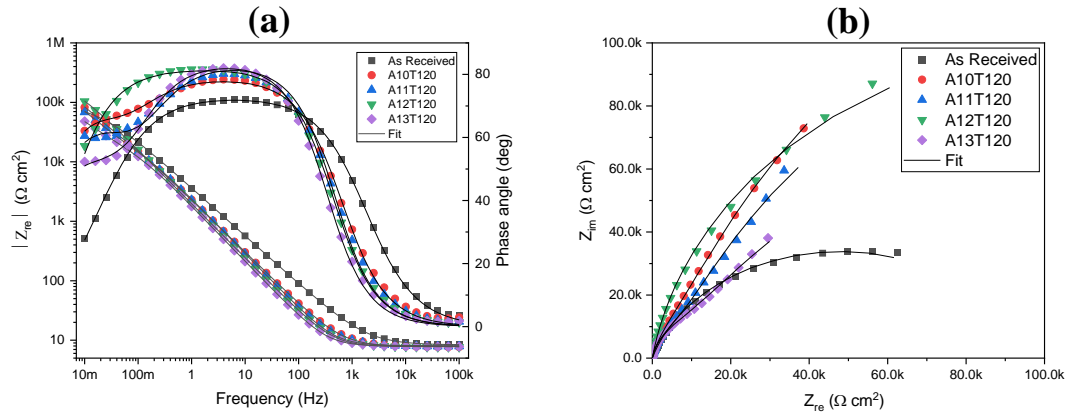


**Figure 22 EIS plots, (a) Modulus and phase angle, and (b) Nyquist plots, showing the effect of solutionizing temperature on the corrosion behavior of N08029 after 1 h immersion in 3.5 % NaCl aerated solution.**

Electrochemical impedance spectroscopy (EIS) is probably among the most sophisticated non-destructive steady-state electrochemistry techniques used for corrosion evaluation as it is capable of providing information relating to the reaction parameters, corrosion rates, oxide formation, and their characteristics, surface integrity, and porosity as well as other interfacial properties [33], [34]. Thus, the investigation of the corrosion behavior of the As-Received and heat-treated alloys using EIS was also conducted. Figures 21 and 22 are the Bode and Nyquist EIS plots showing the effect of solutionizing duration and temperature on the electrochemical behavior of the alloy, respectively. It can be observed from the Bode plots (which consist of modulus impedance ( $|Z|$ ) and phase angle ( $\theta$ ) plots) that the  $\log|Z|$  vs  $\log f$  (frequency) relationship does not conform to -1 and the phase angle maxima ( $\theta_{max}$ ) is much below -90 degrees indicating a deviation from ideal capacitive behavior. It is known that the  $|Z|$  measured from the low-frequency portion of the modulus impedance plot is related inversely to the corrosion rate, thus larger absolute impedance assures superior charge transfer resistance at the surface/electrolyte interface [35]–[38]. In Figure 21(a), the  $|Z|$  can be observed to increase with increasing solutionizing duration while at the same time the  $\theta_{max}$  also tends to increase fairly above -80 degrees in comparison

with the As-Received alloy which is just about -70 degrees. The higher the  $\theta_{max}$  the higher the capacitive behavior of the alloy which indicates improved resistance to charge leakage or transfer to the corrosive medium. Similarly, the peak of the  $\theta_{max}$  for the solutionized samples is also observed to shift to a lower frequency as compared to that of the as-received alloy, this may be associated with surface film formation resulting from corrosion. The accompanying broadening of the phase angle plot with solutionizing duration indicates a two-time constant phenomenon [33]. Figure 21(b) shows the Nyquist plot which supports the increment with solutionizing duration evident from the increasing diameter of the incomplete semi-circle capacitive arc. The higher the diameter of the semi-circle the higher the total resistance to corrosion which indicates the protective performance of the alloys in the medium under consideration [37], [38]. Similarly, the samples solutionized at different temperatures demonstrated an increasing  $|Z|$ , a higher  $\theta_{max}$ , and a broader phase angle plot with temperature until 1200°C (A12T120), and these parameters then decrease at the solutionizing temperature of 1300°C (A13T120) as shown in Figure 22(a). This is also seen in the Nyquist plot in Figure 22(b) from the increasing diameter of the incomplete semi-circle capacitive arc with temperature until 1200°C after which the capacitive arc reduces. It is interesting to note that the  $\theta_{max}$  of sample A13T120 does not drop rather the broadening of the phase angle only reduces. This illustrates the mechanism and reason for the observed reduction in the protectiveness of this sample and this can be associated with the oxide film instability and not compact or denser enough in comparison to the other solutionized samples.

The EIS parameters obtained from the fitting are presented in Tables 12 and 13 for the effect of solutionizing duration and temperature, respectively. The parameters showing the effect of solutionizing duration (in Table 12) illustrate that both  $R_{ct}$  and  $R_f$  increased for the solutionized samples as compared to the As-Received alloy. Quantitatively, the  $R_{ct}$  and  $R_f$  for the sample A12T30 (solutionized for 30 min) were increased by 79% and 22 %, respectively, while for sample A12T60 they were increased by 81% and 31 %, respectively, and by 86% and 34 %, respectively for sample A12T90. Additionally, the  $R_{ct}$  and  $R_f$  for the sample A12T120 (solutionized for 120 min) were increased by 90% and 67 % respectively, while for sample A12T180 they were increased by 93% and 5 %, respectively, and by 95% and 4 %, respectively for sample A12T240. It is observed from this analysis that the higher resistance of the solutionized samples results from both the charge transfer resistance and the resistance of the surface oxide film and that the oxide film resistance also increases with solutionizing duration. Interestingly, solutionized samples for 180, 240 min possess superior  $R_{ct}$  values which may correlate to higher grain size (see Figure 10) while surprisingly,  $R_f$  for both show only a slight increase which maybe related to larger carbides and sigma phases (see Figure 12). The total impedance ( $R_T$ ) which is the sum of the  $R_{ct}$  and  $R_f$  was used to estimate the protective performance ( $\mathcal{E}_{eis}$ ) which shows the increasing protectiveness of 48%, 53%, 60%, 77%, 73% and 79 % with increasing solutionizing duration for 30, 60, 90, 120, 180 and 240 minutes respectively. Similarly, for the effect of solutionizing temperature on the electrochemical behavior of UN08029 alloy (as shown in Table 13), the  $R_{ct}$  increases with increasing the solutionizing temperature until 1200°C which then drops by 73%. However, the  $R_f$  values remain almost unchanged with increasing solutionizing temperature. Thus, the  $R_T$  shows 74, 71, 77, and 26 %

improvement in the corrosion protection performance for sample solutionized at temperatures of 1000°C, 1100°C, 1200°C, and 1300°C, respectively. The EIS results were obtained to substantiate the LPR and CPDP measurements.

**Table 12 EIS parameters obtained from the EC fitting for the samples solutionized for different durations.**

| Sample ID   | $R_s$<br>$\Omega.cm^2$ | $R_{ct}$<br>$k\Omega.cm^2$ | $CPE_{dl}$<br>$\mu F/cm^2$ | $n_{dl}$ | $R_f$<br>$k\Omega.cm^2$ | $CPE_f$<br>$\mu F/cm^2$ | $n_f$ | $R_t(R_{ct}+R_f)$<br>$k\Omega.cm^2$ | $\chi^2$<br>$\times 10^{-4}$ | $\mathcal{E}_{eis}$<br>(%) |
|-------------|------------------------|----------------------------|----------------------------|----------|-------------------------|-------------------------|-------|-------------------------------------|------------------------------|----------------------------|
| As-Received | 23.69                  | 53.110                     | 3.44E-04                   | 0.97     | 245.07                  | 2.16E-05                | 0.81  | 298.18                              | 2.3                          | -                          |
| A12T30      | 23.60                  | 259.635                    | 6.72E-05                   | 0.96     | 316.35                  | 2.87E-05                | 0.92  | 575.99                              | 11.9                         | 48.23                      |
| A12T60      | 23.11                  | 289.560                    | 5.13E-05                   | 0.92     | 356.25                  | 3.93E-05                | 0.91  | 645.81                              | 2.1                          | 53.83                      |
| A12T90      | 21.73                  | 378.195                    | 6.55E-05                   | 0.99     | 373.61                  | 4.35E-05                | 0.93  | 751.80                              | 3.0                          | 60.34                      |
| A12T120     | 20.39                  | 560.310                    | 5.67E-05                   | 0.71     | 746.42                  | 3.33E-05                | 0.91  | 1306.73                             | 1.9                          | 77.18                      |
| A12T180     | 22.75                  | 852.435                    | 8.35E-06                   | 0.74     | 257.73                  | 2.54E-05                | 0.93  | 1110.16                             | 0.9                          | 73.14                      |
| A12T240     | 22.50                  | 1197.570                   | 3.44E-06                   | 0.58     | 255.13                  | 1.76E-05                | 0.86  | 1452.70                             | 2.4                          | 79.47                      |

**Table 13 EIS parameters obtained from the EC fitting for the samples solutionized for different temperatures.**

| Sample ID   | $R_s$<br>$\Omega.cm^2$ | $R_{ct}$<br>$k\Omega.cm^2$ | $CPE_{dl}$<br>$\mu F/cm^2$ | $n_{dl}$ | $R_f$<br>$k\Omega.cm^2$ | $CPE_f$<br>$\mu F/cm^2$ | $n_f$ | $R_t(R_{ct}+R_f)$<br>$k\Omega.cm^2$ | $\chi^2$<br>$\times 10^{-4}$ | $\mathcal{E}_{eis}$<br>(%) |
|-------------|------------------------|----------------------------|----------------------------|----------|-------------------------|-------------------------|-------|-------------------------------------|------------------------------|----------------------------|
| As-Received | 23.69                  | 53.110                     | 3.44E-04                   | 0.97     | 245.07                  | 2.16E-05                | 0.81  | 298.18                              | 2.3                          | -                          |
| A10T120     | 22.24                  | 450.015                    | 1.77E-05                   | 0.83     | 714.15                  | 3.06E-05                | 0.88  | 1164.17                             | 3.0                          | 74.39                      |
| A11T120     | 23.09                  | 389.880                    | 2.87E-05                   | 0.79     | 642.08                  | 2.66E-05                | 0.93  | 1031.96                             | 5.3                          | 71.11                      |
| A12T120     | 20.39                  | 560.310                    | 5.67E-05                   | 0.71     | 746.42                  | 3.33E-05                | 0.91  | 1306.73                             | 1.9                          | 77.18                      |
| A13T120     | 22.55                  | 149.625                    | 4.84E-05                   | 0.73     | 255.08                  | 3.49E-05                | 0.93  | 404.70                              | 19.1                         | 26.32                      |

## E) CORROSION MECHANISM ANALYSIS

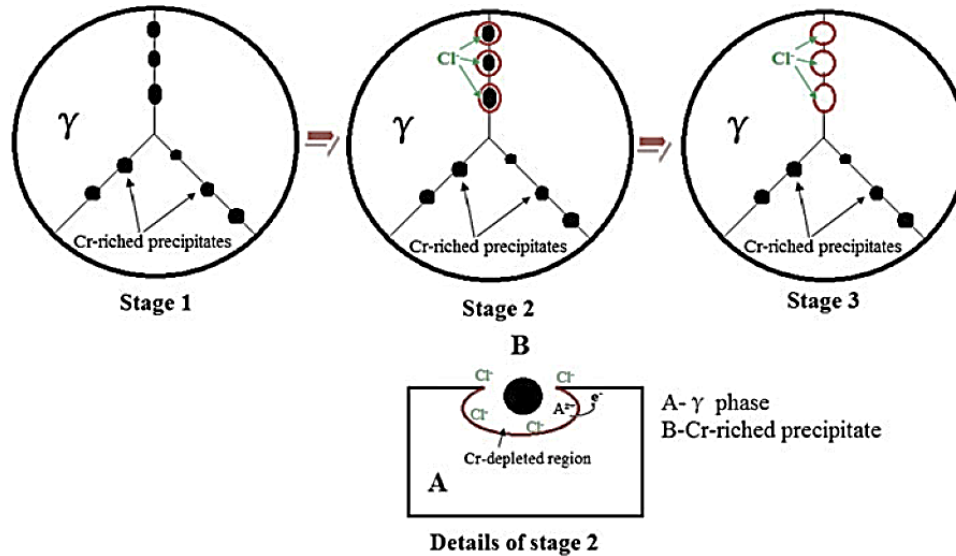
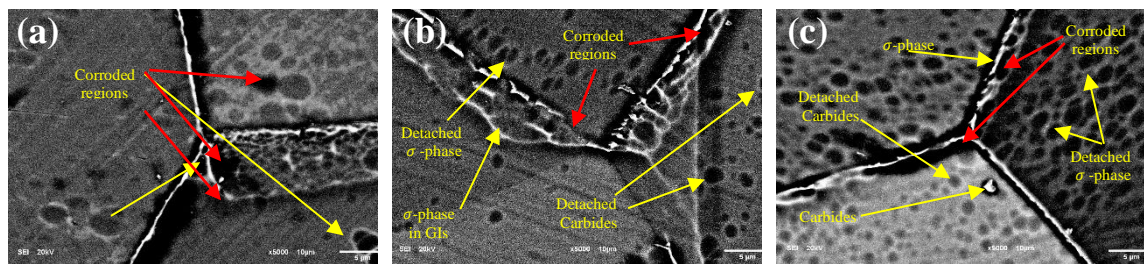


Figure 23 Schematic illustration of the corrosion process of N08029 after 1 h immersion in 3.5 % NaCl aerated solution [3].

SASS is known for its high resistance to corrosion, but it is not completely immune to corrosion. In fact, austenitic stainless steel can be susceptible to a type of corrosion known as crevice corrosion. This occurs when the steel is exposed to an environment that contains chlorides, such as saltwater or brine, and is in contact with a stagnant or low-flow area, such as a crevice, joint, or under a deposit [3]. In this type of environment, the concentration of chlorides can become elevated, which can cause localized breakdown of the protective passive film that typically forms on the surface of stainless steel. Once the passive film is compromised, corrosion can occur, leading to pitting or crevice corrosion [8]–[11]. L.N. Zhang et al. [3] explains the corrosion mechanism of alloy 28 which is the matching corrosion mechanism found in alloy 29. This process can be illustrated in Figure 23: (i) Cl<sup>-</sup> ions prefer to attack the matrix region around precipitates where Cr is depleted; (ii) This region is aggressively corroding; (iii) Finally, the precipitated granules detach from the grain boundaries. A similar phenomenon can be observed for the Cr-rich phase of SASS

alloys[3], [4] An increase in the amount of precipitates with increasing heat treatment time accelerates the micro-galvanic corrosion which is interpreted as the increase of corrosion rate of the investigated alloy. The difference in corrosion behavior of the specimens can be explained on the basis of their microstructural characteristics. Based on our experimental results, it is notable that the Cr-rich precipitates preferentially occur at grain boundaries and this is associated with the presence of chromium-depleted zones surrounding these Cr-rich phases (carbides and sigma phases). Moreover, another significant structural characteristic is the morphology of the precipitates. If the precipitates are present as small and short structures at the grain boundaries, a discontinuous range of depleted zones in the vicinity of precipitates exists. For more comprehensive understanding of the corrosion mechanism, the detailed characteristics of the corroded surfaces were analyzed by SEM.



**Figure 24 (a-c) SEM images which reveal grains arrangement of solutionized samples (a) A12T120, (b) A12T180 and (c) A12T240**

Figure 24 is the SEM images which illustrate heat-treated samples morphologies. The Cr-depleted region primarily at grain boundaries around precipitates is attacked by corrosion. Then, some regions surrounding the granular precipitates are completely corroded and the precipitates are detached from the grain boundaries (detached sigma and carbide phase) [indicated by yellow arrows]. With increasing solutionizing time, more and more coarse precipitates appear in grains interiors and at grain boundaries, and these locations are easily

attacked by the corrosive ions, and more particles are removed from grains interiors and from grain boundaries leaving mouth-shaped crevices or shallow holes as evidence by detached sigma and carbide phase locations. The existence of dark elongated spots along the grain boundaries [indicated by red arrows] of solutionized samples implies that these phases also undermine in the corrosion process. Exacerbated effect of precipitates on corrosion resistance is accelerated when the amount of precipitates increases. Based on the presented analysis, there is a galvanic effect of Cr-rich phase in the corrosion process. When a small fraction of short structures of Cr-rich phases precipitate at grain boundaries, these particles serve primarily as galvanic cathodes, while the Cr-depleted region around precipitates is anodic and is attacked by  $\text{Cl}^-$  ions. Figures 25 shows CPDP and LPR general corrosion rates of heat-treated samples. It is clear that increasing solutionizing duration for 30, 60, 90, 120, 180 and 240 minutes at  $1200^\circ\text{C}$  have minor effect on corrosion behaviour. Similarly, solutionized samples at  $1000^\circ\text{C}$  and  $1100^\circ\text{C}$  show almost similar general corrosion behaviours. However, as explained earlier and after careful analysis, A12T120 shows relatively optimum results as it possesses optimum average grain size (not too large or too small) and has higher amount of twin boundaries which attributed low interface energy which finally increasing corrosion resistance as such. In other hand, heat-treated sample at  $1300^\circ\text{C}$  for 2h have a significant reduction on corrosion resistance due to almost entirely corroded grain boundaries and high amount of precipitates found in the grain interiors due to transition from intergranular to intragranular precipitation phenomena as illustrated in SEM image (Figure 15(c<sub>2</sub>)). However, general corrosion is not the primary concern of SASS alloys, while localized corrosion is severely concerned and it is well discussed in next section.

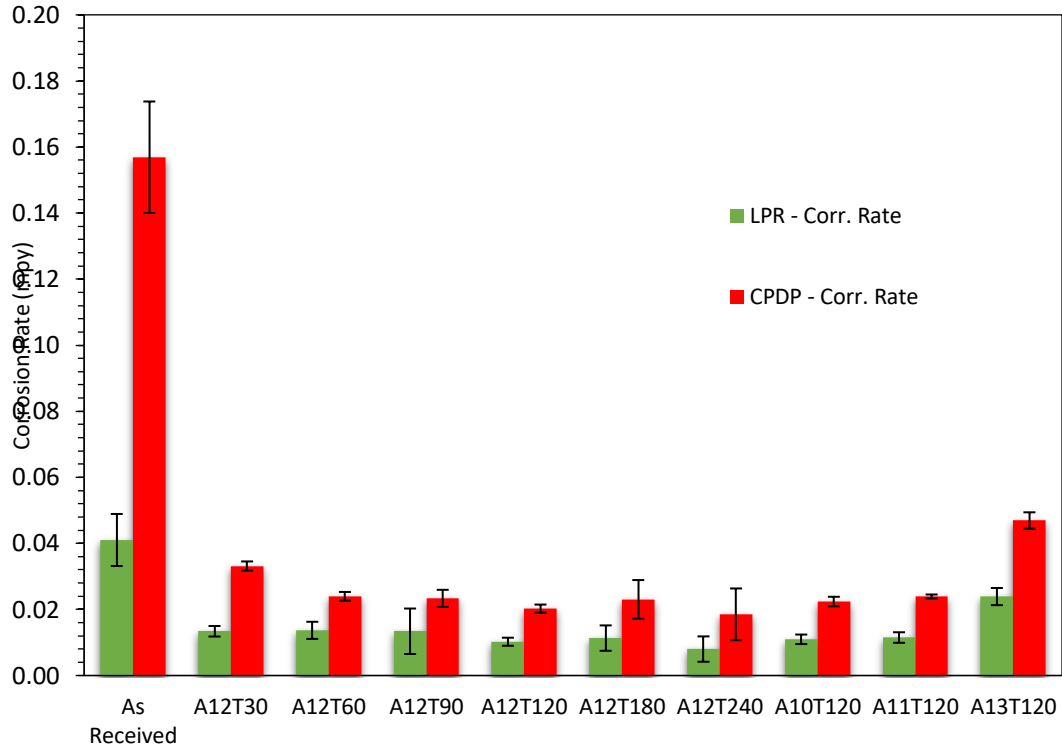


**Figure 25 CPDP and LPR corrosion rates of As-Received sample and all solutionized samples of N08029 after 1 h immersion in 3.5 % NaCl aerated solution.**

## F) CRITICAL PITTING TEMPERATURE (CPT) MEASUREMENT

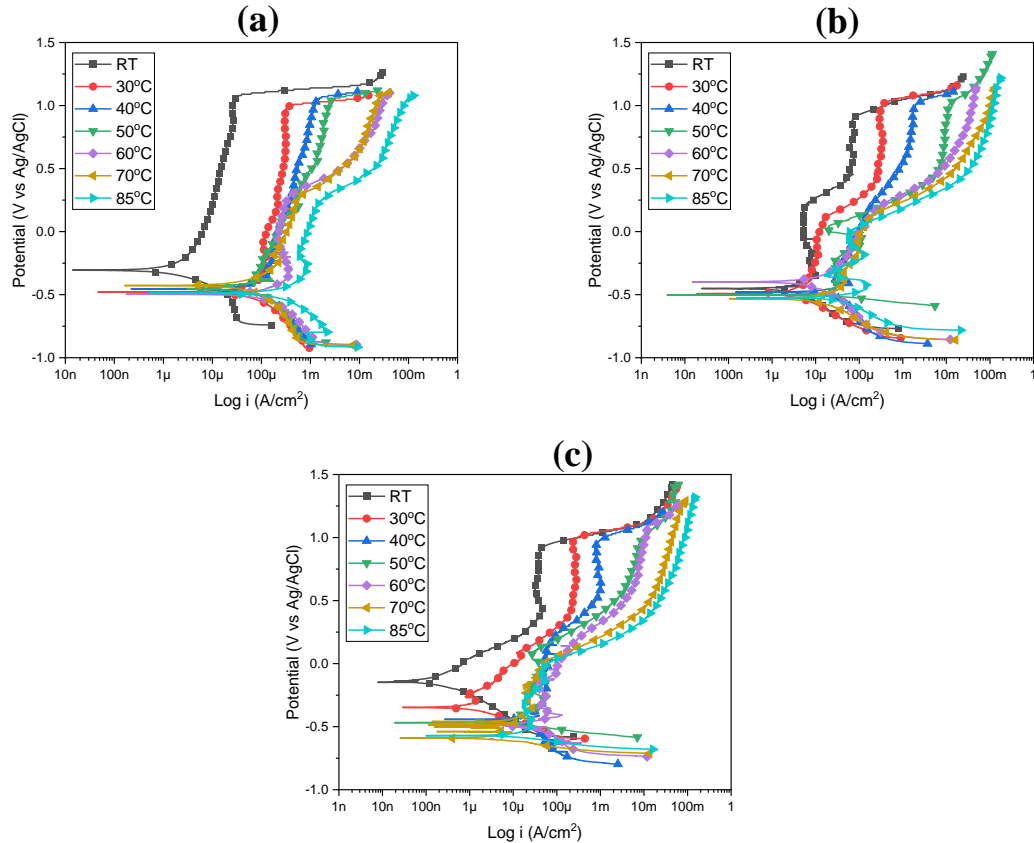


**Figure 26** CPDP curves showing the effect of temperature steepness versus pitting corrosion on (a) As-Received sample (b) A10T120 and (c) A12T120 solutionized samples on the CPT behavior of N08029 after 1 h immersion in 3.5 % NaCl aerated solution.

Since the early 1970s, pitting has had an important characteristic known as the critical pitting temperature (CPT). A wide variety of stainless steels that are no longer susceptible to pitting at room temperature were made possible by the production of high corrosion resistance stainless steels that contain additional alloying elements (mostly Mo and N). Higher temperature pitting corrosion studies on alloyed stainless steel have shown that pitting is very temperature dependent [39], [40]. Brigham and Tozer introduced the idea of CPT for the first time in 1973, which stated that the alloy CPT is the lowest temperature at which a stainless steel experiences pitting corrosion [39]–[45]. Pitting is a significant type of localized corrosion that develops when the passive layer on the metal surface breaks

down. It can spread and produce perforation or the start of stress corrosion cracking subsequently. Thus, pitting is a unique and unpredictable process, making it challenging to anticipate when and where it will start [44]. Transpassive refers to a state in which a metal is corroding, but the rate of corrosion is slow [39], [40]. There were four stages thought to be involved in the pitting corrosion of metals: (i) the creation of the passive layer, (ii) the breakdown of the passive layer, (iii) the growth of unstable pits that either can repassivate, and/or (iv) the growth of bigger and stable pits. The breakdown of the passive film and the beginning and spread of the pitting attack are both indicated when the potential hits a specific critical potential, breakdown potential ( $E_b$ ), and the passive current rises abruptly and steeply without any indication of oxygen evolution [39], [40], [46]. In the range of 1 to 5 M NaCl, Qvarfort showed that the CPT was independent of chloride concentration. He also discovered that the CPT was independent of pH in the range of 1 to 7 [44], [47]. The CPT marks a very sharp transition, and according to Qvarfort's findings, it can be precisely described to within  $-1^\circ\text{C}$  in the absence of undesirable crevice corrosion. The CPT is clearly the outcome of a deterministic process. The geometry of potential pit initiation locations must be considered, as the CPT varies significantly with surface roughness [44], [47]. Brigham and Tozer reported that the correlation between CPT of various commercially graded stainless steel and addition of Cu, Ni, N, or Si to the matrix have no observed effect [43]. Alloying elements and impurities that mixed with steel have significant impact on austenite, ferrite, and cementite phase formation. The combination of alloying ingredients and exerted heat treatment program result in a wide range of microstructures and characteristics of an alloy. Austenitic phase is stabilized mainly when high percentage of nickel and chromium elements exist [1]. The microstructural properties of alloys, in

general, have a significant impact on their performance. Nickel is a noncarbide-forming element in steels, the hardenability, impact toughness, and fatigue resistance of steels are increased when Ni combined with Cr and Mo [1]. Ni is an essential additive for stabilizing the austenite phase, however studies have shown that it has no appreciable impact on alloys that are already entirely austenitic's resistance to pit initiation [43]. Furthermore, Mo boosts corrosion resistance and is heavily utilized in high-alloy Cr ferritic stainless steels as well as with Cr-Ni austenitic stainless steels. Hence, the stainless steel's tendency to pit is diminished by high Mo concentration which has been reported as the main factor for pitting resistance [1], [43]–[47].

There are various methods that can be used to determine the CPT. The shifting of the alloy's behavior from transpassivity to pitting corrosion in solution containing aggressive ions is the focus of several methodologies that are used to measure CPT of high pitting resistance stainless steels [39]–[41]. As a result, there are two main types of measurement techniques that rely on applied potential from an external source (such a potentiostat). i) Those in which the test is repeated in a series of temperature increases while being conducted at a constant temperature called “potentiodynamic”. ii) Tests in which the temperature is constantly elevated during a single test run and the temperature at which a sudden increase in current density was noticed can be regarded as the alloy's CPT value “potentiostatic” [39]–[41]. Some authors have claimed that the potentiostatic CPT was nearly unaffected by various test conditions such exposed area, applied potential, and gas purging and that it closely mimics the potentiodynamic results [44]. Additionally, the potentiostatic test was faster and easier to perform. As a result, it was believed to be the most effective technique for conducting a short comparison of stainless steels resistance to pitting [45], [47], [48].

While investigators utilized potentiostatic more and more frequently. Potentiodynamic CPT was rarely discussed, the literature is still, in our judgment, insufficient. During the heat treatment and welding procedures of many heavily alloyed steels, a range of desirable and undesirable precipitates occur, which can have a significant impact on the mechanical properties and corrosion resistance of the steels [3]. The present work is focused on potentiodynamic CPT effect on cold-rolled heat-treated samples of Fe-Ni based alloy UNS N08029 (Alloy 29) of HAASS. Criterion of pit initiation, Breakdown Potential ( $E_b$ ), is mainly dependent on material behavior during electrochemical test methods [1]. For instance,  $10 \mu\text{A}/\text{cm}^2$  widely considered as breakdown potential for commercial classes of austenitic stainless steels [1], [42], [47]. In other hand, for almost same material and duplex stainless steel,  $100 \mu\text{A}/\text{cm}^2$  widely considered to be breakdown potential. Thus,  $10 \text{mA}/\text{cm}^2$  has been selected as breakdown potential since there is no strategical study that evaluates the influence of potentiodynamic CPT on the corrosion properties of SASS UNS N08029 grade.

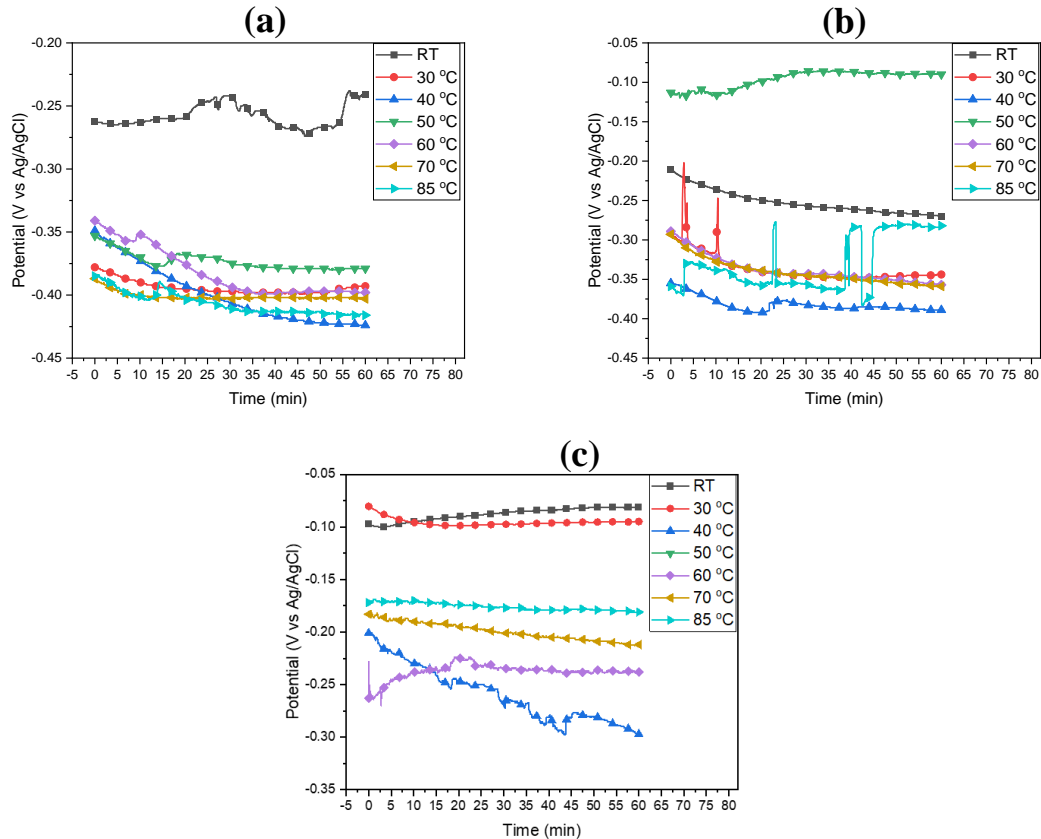


**Figure 27** Open circuit potentials showing the effect of temperature steepness versus pitting corrosion on (a) As-Received sample (b) A10T120 and (c) A12T120 solutionized samples on the CPT behavior of N08029 after 1 h immersion in 3.5 % NaCl aerated solution.

In this study, potentiodynamic measurement used to investigate the CPT for As-Received and solutionized samples at 1000°C (A10T120) and 1200°C (A12T120) for a temperature steepness of 10°C started from room temperature (RT) 20°C, 30°C, 40°C, 50°C, 60°C, 70°C and 85°C. Thus, by taking extra precautions to avoid crevice corrosion, measuring potentiodynamic polarisation curves at various temperatures and plotting the breakdown potential ( $E_b$ ) vs. temperature. When the variation of breakdown potential vs. temperature is plotted, if crevice corrosion does not affect the pitting test results, CPT is the temperature where the breakdown potential suddenly changes from transpassive to stable pitting corrosion. 10 mA/cm<sup>2</sup> has been selected as breakdown potential.

**Table 14 Tafel extrapolation and pitting parameters obtained from the CPDP measurement for the As-Received sample at different temperature steepness for the CPT behavior of N08029 after 1 h immersion in 3.5 % NaCl aerated solution.**

| Sample ID | $I_{corr}$ ( $\mu\text{A}/\text{cm}^2$ ) | $E_{corr}$ (mV) | $\beta_a$ (mV/dec) | $\beta_c$ (mV/dec) | CR (mpy) | $\epsilon_{pit}$ (%) | $E_{pit}$ (mV) | $I_p$ ( $\mu\text{A}/\text{cm}^2$ ) |
|-----------|--|-----------------|--------------------|--------------------|----------|----------------------|----------------|-------------------------------------|
| RT (20°C) | 291.0                                    | -144            | 919.67             | 203.90             | 1.33     | -                    | 906.5          | 42.9                                |
| 30°C      | 6333.3                                   | -144            | 227.67             | 172.33             | 28.95    | 8.49%                | 983.5          | 334.1                               |
| 40°C      | 13500.0                                  | -144            | 772.87             | 404.83             | 61.76    | 15.28%               | 1045           | 1324.0                              |
| 50°C      | 1200.0                                   | -144            | 79.27              | 42.93              | 5.48     | -                    | 124.8          | 287.9                               |
| 60°C      | 11066.7                                  | -144            | 197.53             | 196.73             | 50.65    | 86.23%               | 282.6          | 381.0                               |
| 70°C      | 13400.0                                  | -144            | 563.83             | 471.57             | 61.09    | -                    | 241.5          | 521.5                               |
| 85°C      | 24333.3                                  | -144            | 197.87             | 211.63             | 111.06   | 73.36%               | 217.0          | 1408.0                              |
|           |  |                 |                    |                    |          | 76.06%               |                |                                     |

**Table 15 Tafel extrapolation and pitting parameters obtained from the CPDP measurement for the A10T120 sample at different temperature steepness for the CPT behavior of N08029 after 1 h immersion in 3.5 % NaCl aerated solution.**

| Sample ID | $I_{corr}$ ( $\mu\text{A}/\text{cm}^2$ ) | $E_{corr}$ (mV) | $\beta_a$ (mV/dec) | $\beta_c$ (mV/dec) | CR (mpy) | $\epsilon_{pit}$ (%) | $E_{pit}$ (mV) | $I_p$ ( $\mu\text{A}/\text{cm}^2$ ) |
|-----------|--|-----------------|--------------------|--------------------|----------|----------------------|----------------|-------------------------------------|
| RT (20°C) | 139.0                                    | -103            | 98.13              | 107.90             | 0.64     | -                    | 931.2          | 255.0                               |
| 30°C      | 521.3                                    | -103            | 374.70             | 210.57             | 2.38     | 8.68%                | 1012.0         | 370.3                               |
| 40°C      | 3266.7                                   | -103            | 141.53             | 397.47             | 14.92    | 6.53%                | 992.0          | 1888.0                              |
| 50°C      | 954.7                                    | -103            | 42.60              | 21.83              | 4.37     | -94.33%              | 52.8           | 22.0                                |
| 60°C      | 1983.3                                   | -103            | 444.80             | 379.77             | 9.07     | -90.55%              | 88.0           | 144.7                               |
| 70°C      | 1650.0                                   | -103            | 193.87             | 202.40             | 7.54     | -97.04%              | 27.6           | 121.1                               |
| 85°C      | 3853.3                                   | -103            | 98.33              | 192.03             | 17.61    | -98.95%              | 9.7            | 63.8                                |

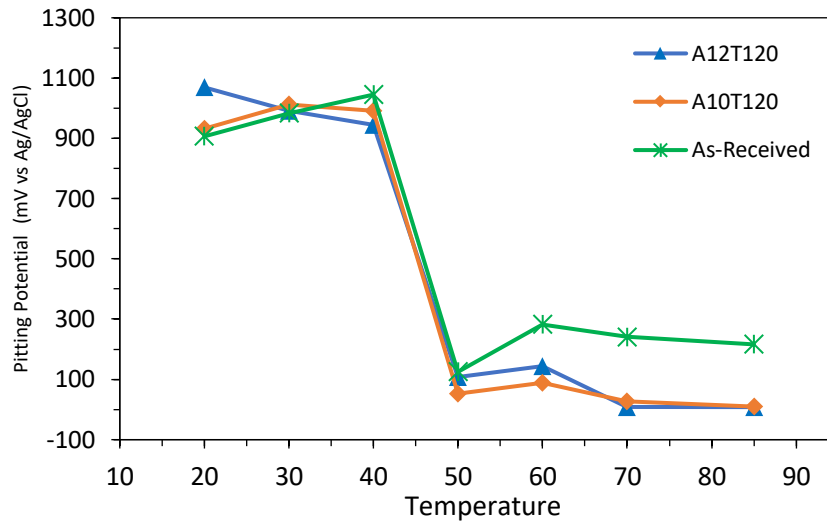
**Table 16 Tafel extrapolation and pitting parameters obtained from the CPDP measurement for the A12T120 sample at different temperature steepness for the CPT behavior of N08029 after 1 h immersion in 3.5 % NaCl aerated solution.**

| Sample ID | $I_{corr}$ ( $\mu\text{A}/\text{cm}^2$ ) | $E_{corr}$ (mV) | $\beta_a$ (mV/dec) | $\beta_c$ (mV/dec) | CR (mpy) | $\epsilon_{pit}$ (%) | $E_{pit}$ (mV) | $I_p$ ( $\mu\text{A}/\text{cm}^2$ ) |
|-----------|--|-----------------|--------------------|--------------------|----------|----------------------|----------------|-------------------------------------|
| RT (20°C) | 95.1                                     | -162            | 159.53             | 67.73              | 0.04     | -                    | 1069.0         | 31.3                                |
| 30°C      | 168.0                                    | -162            | 375.67             | 107.27             | 0.77     | -7.30%               | 991.0          | 273.7                               |
| 40°C      | 694.0                                    | -162            | 23.60              | 114.73             | 3.17     | -11.63%              | 944.7          | 810.6                               |
| 50°C      | 609.3                                    | -162            | 159.73             | 39.87              | 2.79     | -89.85%              | 108.5          | 33.8                                |
| 60°C      | 1750.0                                   | -162            | 81.10              | 127.73             | 8.00     | -86.46%              | 144.7          | 37.4                                |
| 70°C      | 412.0                                    | -162            | 544.27             | 44.67              | 2.71     | -99.21%              | 8.5            | 54.2                                |
| 85°C      | 1221.3                                   | -162            | 191.57             | 50.97              | 5.58     | -99.17%              | 8.9            | 55.2                                |

The system is anticipated to reach a steady-state condition when the potential is no longer dependent on the duration of immersion. The unperturbed corroding potential of the sample was monitored using the OCP measurement when no external current was applied. As a result, the OCP illustrates the electrochemical environment's stability prior to polarizing the system and gives details on the samples thermodynamic propensity for corrosion. Figure 27 is OCP for the solutionized samples makes it obvious that after a monitoring period of 1 h, the samples reached an equilibrium condition. Figure 27(a) shows the OCP trend of the As-Received sample for different temperatures (20°C to 85°C), it is seen that the samples attain an equilibrium state and exhibited an active potential as temperature increases while 40°C is the most active temperature step with potential of -424mV, -389 mV and -297mV for As-Received, A10T120 and A12T120, respectively. A similar trend is observed for the A12T120 sample which solutionized at (1200°C) as shown in Figure 27(c) which RT shows the noblest potentials at the end of -241mV and -81.3 mV for As-Received and A12T120, respectively. Furthermore, the noblest potential of the sample A10T120 is at 50°C with potential of -90 mV while RT temperature step potential is -270 mV as shown in Figure 27(b). However, the samples mostly showed a steady OCP over a wide duration indicating the early formation of the film and its stability and protectiveness. In other hand, at 40°C shows higher degree of instability, especially for A12T120, despite attaining equilibrium state, at relatively late stage, which indicates the less inertness of the sample at 40°C and hence the higher the corrosion propensity in the test environment. The CPT CPDP measurement rate was  $0.5 \text{ mVs}^{-1}$ , starting at 50 mV below OCP up to the anodic potential value at which an abrupt increase in current density occurred as shown in Figure 26. The sudden current increase was either due to extensive pitting corrosion or

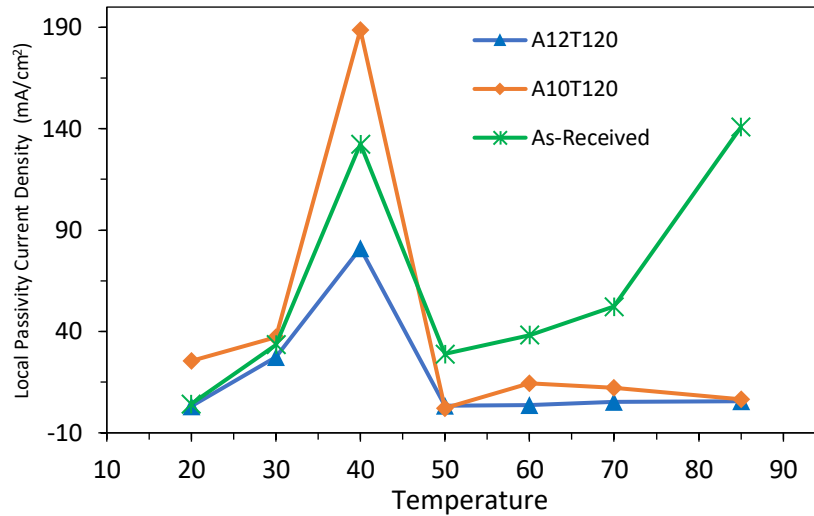
transpassivity dissolution as shown in Tables (14, 15 and 16) for As-Received, A10T120 and A12T120, respectively. The potential at which the current density exceeded passivity region was defined as the pitting potential ( $E_{pit}$ ). Generally, by increasing the temperature from lower temperatures to higher ones, the local passivity current density ( $I_p$ ) increases up to maximum at 40°C. For instance, in the case of As-Received alloy, it increased from 42.9 to 1324  $\mu\text{A}/\text{cm}^2$  when temperature increased from 20°C to 40°C, respectively, A10T120 and A12T120 trend similarly from 20°C to 40°.

The pitting potential sharply decreased at 50°C for As-Received, A10T120 and A12T120 by 86%, 94% and 90%, respectively as shown in Figure 28. It can be observed that in 3.5 % NaCl aerated solution, As-Received, A10T120 and A12T120 show local passivity behaviour in the temperature ranges of 20°C - 40°C in correspondence to pitting potential ( $E_{pit}$ ). Interestingly, heat-treated sample for 1000°C (A10T120) shows the highest local passivity current density (1888  $\mu\text{A}/\text{cm}^2$ ) while solutionized sample for 1200°C (A12T120) is the lowest local passivity current density (811  $\mu\text{A}/\text{cm}^2$ ) as illustrated in Figure 29. General corrosion rate at 50°C exhibit sharp reduction for all samples which might correlated to shortening pitting potential (faster pitting corrosion) and dominating transpassivity behavior to pitting corrosion which is in other word, a quick completion of stable pit formation and new passivation film formation.



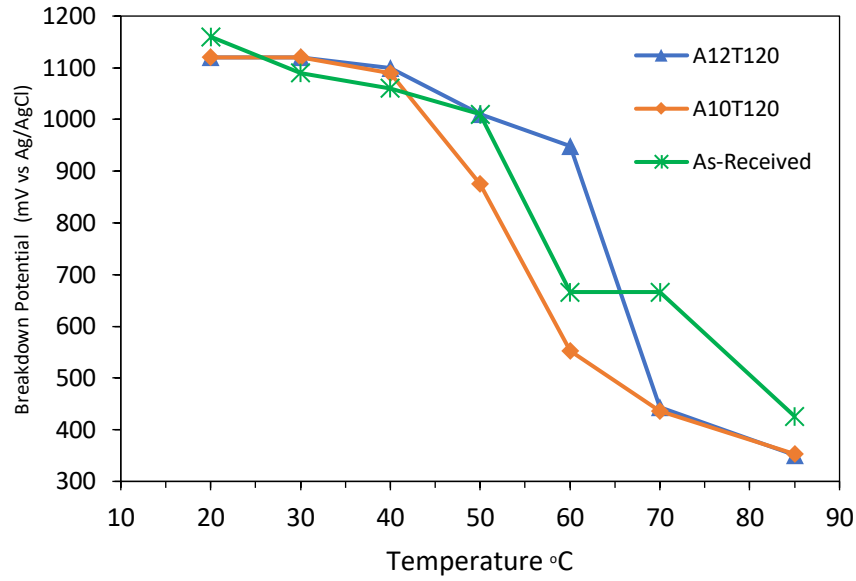
**Figure 28** Pitting potential vs. temperature curves showing the effect of temperature steepness versus pitting corrosion on As-Received, A10T120 and A12T120 solutionized samples on the CPT behavior of N08029 after 1 h immersion in 3.5 % NaCl aerated solution.

Additionally,  $I_p$  of As-Received alloy increased rapidly from 60°C to 85°C which might be an indication of weak, less dense, passive film formation and tends rapidly to pit formation at high temperatures. While A10T120 and A12T120 kept at low passivation current density which might be an indication of inertness and effectiveness of passivated stable pit formed earlier.



**Figure 29** Local passivity current density vs. temperature curves showing the effect of temperature steepness versus pitting corrosion on As-Received, A10T120 and A12T120 solutionized samples on the CPT behavior of N08029 after 1 h immersion in 3.5 % NaCl aerated solution.

CPT is the temperature where the breakdown potential suddenly changes from transpassive to stable pitting corrosion.  $10 \text{ mA/cm}^2$  has been selected as breakdown potential. Figure 30 shows CPT behavior of As-Received, A10T120 and A12T120. Interestingly, the breakdown potential ( $E_b$ ) at  $10 \text{ mA/cm}^2$  decreased for all samples.  $E_b$  of As-Received decreases from 1160 mV at  $20^\circ\text{C}$  to 426 mV at  $85^\circ\text{C}$ , while A10T120 and A12T120 decreases from 1120 mV at  $20^\circ\text{C}$  to 353 mV and 351 mV at  $85^\circ\text{C}$ , respectively. It can be observed that in 3.5 % NaCl aerated solution, As Received and A10T120 show passivity behaviour in the temperature ranges from  $20^\circ\text{C}$  to  $50^\circ\text{C}$  while A12T120 shows higher temperature passivity (from  $20^\circ\text{C}$  to  $60^\circ\text{C}$ ). At  $50^\circ\text{C}$ , the breakdown potential decreases by 13% and 22% for As Received and A10T120, respectively. Whereas a 15% reduction for A12T120 at  $60^\circ\text{C}$ . Despite it is still in passivity region, heat-treated sample for  $1000^\circ\text{C}$  (A10T120) shows quite high reduction percentage (by 22%) which may correlate this behavior to the distribution and presence of Mo-rich precipitates (carbides) along grain boundaries as shown in Figure 13(b) and Figure 15(a).



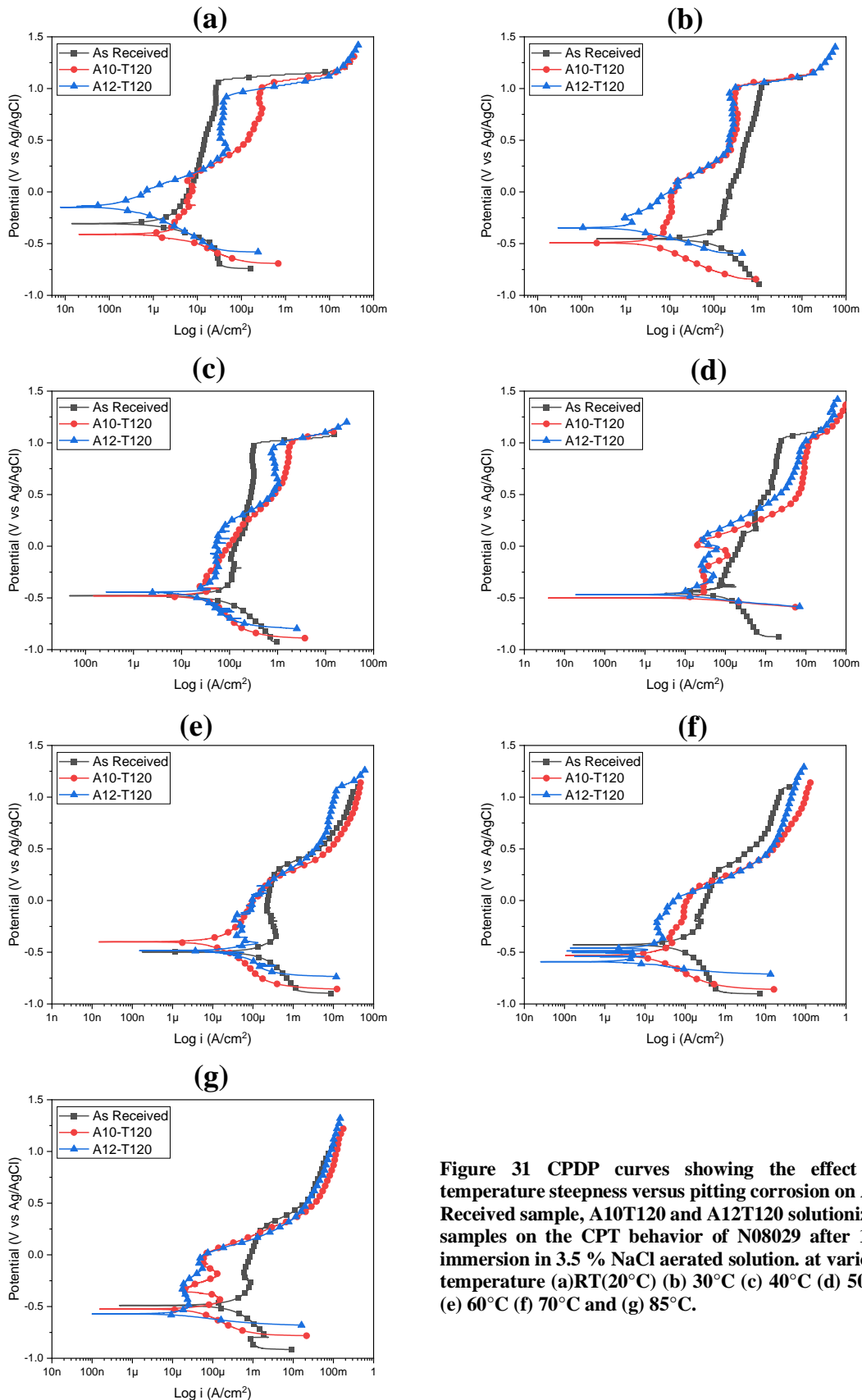
**Figure 30 Breakdown potential vs. temperature curves showing the effect of temperature steepness versus pitting corrosion on As-Received, A10T120 and A12T120 solutionized samples on the CPT behavior of N08029 after 1 h immersion in 3.5 % NaCl aerated solution.**

Figure 26(a,b) show high fluctuation in current density along with sharp potential reduction by 43% and 51% at 60°C for As Received and A10T120, respectively. A better representation can be seen in Figure 30. Similarly, a topical behavior is observed for A12T120 at 70°C with sharp potential reduction by 60% as seen Figure 26(c). Thus, the observed behavior is a transition from transpassivity to pitting corrosion. In summary, based on CPT CPDP measurements in various temperatures, shown in Figure 30 and Table 17, a transition from transpassivity to pitting corrosion occurs between 50°C to 60°C for As Received and A10T120 while heat-treated sample for 1200°C (A12T120) shows higher transition temperature (between 60°C to 70°C) which means possess higher pitting corrosion resistance.

Figure 31 shows CPDP for various elevated temperature curves which is an evident that solutionized sample for 1200°C (A12T120) at 120 min. is the most noble sample and thus, it can be considered to possess the most optimized sample as function of corrosion-resistance properties.

**Table 17 breakdown potential at 10 mA/cm<sup>2</sup> obtained from the CPDP measurement for As-Received, A10T120 and A12T120 samples at different temperature steepness for the CPT behavior of N08029 after 1 h immersion in 3.5 % NaCl aerated solution.**

| Sample ID | As-Received         |                    | A10T120             |                    | A12T120             |                    |
|-----------|---------------------|--------------------|---------------------|--------------------|---------------------|--------------------|
|           | E <sub>b</sub> (mV) | ε <sub>b</sub> (%) | E <sub>b</sub> (mV) | ε <sub>b</sub> (%) | E <sub>b</sub> (mV) | ε <sub>b</sub> (%) |
| RT (20°C) | 1160                | -                  | 1120                | -                  | 1120                | -                  |
| 30°C      | 1090                | -6%                | 1120                | 0%                 | 1120                | 0%                 |
| 40°C      | 1060                | -9%                | 1090                | -3%                | 1100                | -2%                |
| 50°C      | 1010                | -13%               | 875                 | -22%               | 1010                | -10%               |
| 60°C      | 666                 | -43%               | 552                 | -51%               | 949                 | -15%               |
| 70°C      | 666                 | -43%               | 436                 | -61%               | 444                 | -60%               |
| 85°C      | 426                 | -63%               | 353                 | -68%               | 351                 | -69%               |



**Figure 31** CPDP curves showing the effect of temperature steepness versus pitting corrosion on As-Received sample, A10T120 and A12T120 solutionized samples on the CPT behavior of N08029 after 1 h immersion in 3.5 % NaCl aerated solution. at various temperature (a)RT(20°C) (b) 30°C (c) 40°C (d) 50°C (e) 60°C (f) 70°C and (g) 85°C.

## 3.2.3 HARDNESS OF HEAT-TREATED SAMPLES

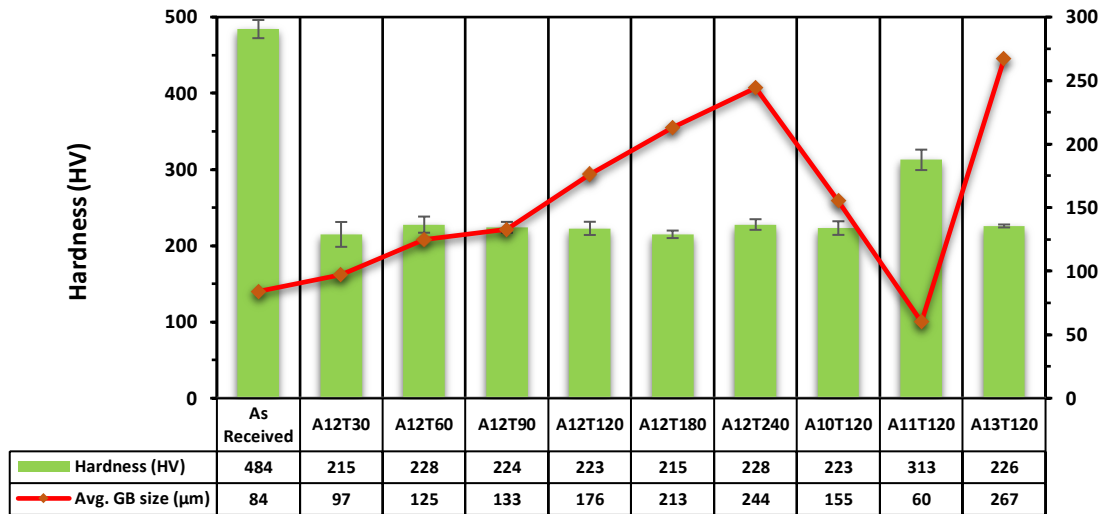


**Figure 32 Influence of average grain size on hardness of As-Received and heat-treated samples as function of solutionizing duration (A12T30, A12T60, A12T390, A12T120, A12T180 & A12T240) and temperature (A10T120, A11T120, A12T120 & A13T120).**

The hardness of the samples was determined as an indicator of changes in mechanical properties. The mean Vickers Hardness (HV) values for As-Received alloy sample and solutionized samples at different durations and temperatures that underwent heat treatment are shown in Figure 32. The current findings in conjunction with the information on the average grain boundary sizes clearly demonstrate that the increase in hardness is correlated with the percentage of average grain boundary sizes among the heat-treated samples. The higher the average grain boundary, the lesser area fraction of precipitates and hence the lower the hardness. In comparison to the other heat-treated samples, solutionized sample at 1100°C (A11T120) exhibits the highest value of hardness which can be correlated to possess the highest area proportion of precipitates due to lowest average grain boundary size (60 μm). According to Zhang et al., austenite's hardness is only about half as high as

that of the  $\sigma$ -phase which investigations of comparable corrosion-resistant stainless steels provided more support for the influence of precipitates on hardness [3].

### 3.3. CONCLUSIONS

The effect of solutionizing duration and temperature on the electrochemical corrosion and pitting resistance in 3.5% NaCl solution of cold rolled super austenitic stainless UN08029 alloy were investigated in this study. The samples were solutionized at a constant temperature for a duration of 30, 60, 90, 120, 180 and 240 min, and a temperature range of 1000°C – 1300°C for a fixed duration (120 min.) was considered during the solution annealing treatment. The following are some conclusions from the study:

1. The elongated columnar grains recrystallized to uniform equiaxed grains during the solution annealing. Increasing the solutionizing duration and temperatures resulted in grain growth. This was associated with increased grain boundary migration due to increased thermal kinetics at longer duration and higher temperatures.
2. The polarization resistance measurement showed that the corrosion resistance of the untreated (As-Received) alloy sample was increased by about 65%, 67%, 69%, 75%, 72% and 80 % after solutionizing for a duration of 30, 60, 90, 120, 180 and 240 min, respectively. Similarly, the resistance of the alloy was also increased by about 73%, 71%, 75%, and 42 % after solutionizing at temperatures of 1000°C, 1100°C, 1200°C, and 1300°C, respectively.
3. Though the  $E_{pit}$  for the untreated alloy sample is higher than that of the solutionized samples, the hysteresis loop for all solutionized samples was much lower in comparison. Based on the pitting potential and the hysteresis loop, which defined the pitting and repassivation properties of the alloys, the sample solutionized at

1200°C for 120 min (A12T120) showed an optimum combination of pitting resistance parameters, thus demonstrated the least pitting corrosion damage.

4. The total charge transfer resistance obtained from the electrochemical impedance measurement shows the increasing protectiveness of 48%, 53%, 60%, 77%, 73% and 79 % with increasing solutionizing duration for 30, 60, 90, 120, 180 and 240 minutes respectively. Also, a 74%, 71%, 77%, and 26 % improvement in the corrosion protection performance for sample solutionized at temperatures of 1000°C, 1100°C, 1200°C, and 1300°C, respectively.
5. Potentiodynamic measurement used to investigate the CPT for As-Received and solutionized samples at 1000°C (A10T120) and 1200°C (A12T120) for a temperature steepness of 10°C started from room temperature (RT) 20°C, 30°C, 40°C, 50°C, 60°C, 70°C and 85°C. OCP measurement shows that at 40°C is the most active temperature step with potential of -424mV, -389 mV and -297mV for As-Received, A10T120 and A12T120, respectively.
6. The pitting potential sharply decreased at 50°C for As-Received, A10T120 and A12T120 by 86%, 94% and 90%, respectively. It can be observed that As-Received, A10T120 and A12T120 show local passivity behavior in the temperature ranges of 20°C - 40°C in correspondence to pitting potential ( $E_{pit}$ ). A10T120 shows the highest local passivity current density (1888  $\mu\text{A}/\text{cm}^2$ ) while solutionized sample for 1200°C (A12T120) is the lowest local passivity current density (811  $\mu\text{A}/\text{cm}^2$ ). General corrosion rate at 50°C exhibit sharp reduction for all samples which might correlated to shortening pitting potential (faster pitting corrosion) and dominating

transpassivity behavior to pitting corrosion which is in other word, a quick completion of stable pit formation and new passivation film formation.

7. The breakdown potential ( $E_b$ ) at 10 mA/cm<sup>2</sup>, CPT criterion, decreased for all samples.  $E_b$  of As-Received decreases from 1160 mV at 20°C to 426 mV at 85°C, while A10T120 and A12T120 decreases from 1120 mV at 20°C to 353 mV and 351 mV at 85°C, respectively. It can be observed that in 3.5 % NaCl aerated solution, As Received and A10T120 show passivity behavior in the temperature ranges from 20°C to 50°C while A12T120 shows higher temperature passivity (from 20°C to 60°C).
8. CPT CPDP measurements in various temperatures show a transition from transpassivity to pitting corrosion occurs between 50°C to 60°C for As Received and A10T120 while heat-treated sample for 1200°C (A12T120) shows higher transition temperature (between 60°C to 70°C) which means possess higher pitting corrosion resistance.
9. The superior corrosion and pitting resistances for the sample solutionized at 1200°C for 120 min (A12T120) were attributable to larger grain size and spontaneous formation of the dense and compact passive film, which conferred it with higher charge transfer resistance and faster repassivation property.

## REFERENCES

- [1] G. National and H. Pillars, *Steel Heat Treatment Handbook*, Second. Portland, Oregon, 2006.
- [2] Y. Jiang, Q. Zuo, and F. Liu, "Mechanism for the multi-stage precipitation of Fe-Ni based alloy," *J Mater Sci Technol*, vol. 35, no. 11, pp. 2582–2590, Nov. 2019, doi: 10.1016/j.jmst.2019.05.064.
- [3] L. N. Zhang, J. A. Szpunar, J. X. Dong, and M. C. Zhang, "Influence of heat treatment on the microstructure and corrosion behavior of Ni-Fe-Cr alloy 028," *J Mater Res*, vol. 29, no. 18, pp. 2147–2155, Aug. 2014, doi: 10.1557/jmr.2014.249.
- [4] S. Ghosh and T. Ramgopal, "Effect of Chloride and Phosphoric Acid on the Corrosion of Alloy C-276, UNS N08028, and UNS N08367," 2005.
- [5] U. Kivis€u, "A test method for dewpoint corrosion of stainless steels in dilute hydrochloric acid." [Online]. Available: [www.elsevier.com/locate/corsciCorrosionScience45](http://www.elsevier.com/locate/corsciCorrosionScience45)
- [6] X. Gó Mez and J. Echeberria, "Microstructure and mechanical properties of carbon steel A210Á/superalloy Sanicro 28 bimetallic tubes." [Online]. Available: [www.elsevier.com/locate/msea](http://www.elsevier.com/locate/msea)
- [7] P. Vainikka *et al.*, "High temperature corrosion of boiler waterwalls induced by chlorides and bromides. Part 1: Occurrence of the corrosive ash forming elements in a fluidised bed boiler co-firing solid recovered fuel," *Fuel*, vol. 90, no. 5, pp. 2055–2063, May 2011, doi: 10.1016/j.fuel.2011.01.020.
- [8] T. Koutsoukis, A. Redjaimia, and G. Fournalis, "Phase transformations and mechanical properties in heat treated superaustenitic stainless steels," *Materials Science and Engineering A*, vol. 561, pp. 477–485, Jan. 2013, doi: 10.1016/j.msea.2012.10.066.
- [9] T. Koutsoukis, E. G. Papadopoulou, S. Zormalia, P. Kokkonidis, and G. Fournalis, "Precipitation sequences in cold deformed superaustenitic stainless steels," *Materials Science and Technology*, vol. 26, no. 9, pp. 1041–1048, Sep. 2010, doi: 10.1179/026708309X12506933872748.
- [10] T. Koutsoukis, K. Konstantinidis, E. G. Papadopoulou, P. Kokkonidis, and G. Fournalis, "Comparative study of precipitation effects during aging in superaustenitic and superferritic stainless steels," *Materials Science and Technology*, vol. 27, no. 5, pp. 943–950, May 2011, doi: 10.1179/026708310X12712410311938.
- [11] T.-H. Lee, S.-J. Kim, and Y.-C. Jung, "Crystallographic Details of Precipitates in Fe-22Cr-21Ni-6Mo-(N) Superaustenitic Stainless Steels Aged at 900 C."
- [12] C. O. A. Olsson, M. Hättestrand, H. Magnusson, D. Shinde, and M. Thuvander, "Early precipitation stages of sigma phase in alloy 28 studied with scanning electron microscopy and atom probe tomography," *ISIJ International*, vol. 61, no. 3, pp. 881–887, Mar. 2021, doi: 10.2355/ISIJINTERNATIONAL.ISIJINT-2020-591.
- [13] J. Anburaj, S. S. M. Nazirudeen, R. Narayanan, B. Anandavel, and A. Chandrasekar, "Ageing of forged superaustenitic stainless steel: Precipitate phases and mechanical properties," *Materials Science and Engineering A*, vol. 535, pp. 99–107, Feb. 2012, doi: 10.1016/j.msea.2011.12.048.
- [14] B. H. Shin, J. Park, J. Jeon, S. bo Heo, and W. Chung, "Effect of cooling rate after heat treatment on pitting corrosion of super duplex stainless steel UNS S 32750," *Anti-Corrosion Methods and Materials*, vol. 65, no. 5, pp. 492–498, Oct. 2018, doi: 10.1108/ACMM-05-2018-1939.
- [15] J. Schindelin *et al.*, "Fiji: An open-source platform for biological-image analysis," *Nature Methods*, vol. 9, no. 7, pp. 676–682, Jul. 2012. doi: 10.1038/nmeth.2019.
- [16] R. M. Souto and H. Alanyali, "Electrochemical characteristics of steel coated with TiN and TiAlN coatings", [Online]. Available: [www.elsevier.com/locate/corsci](http://www.elsevier.com/locate/corsci)
- [17] A. Y. Adesina, Z. M. Gasem, and A. Madhan Kumar, "Corrosion Resistance Behavior of Single-Layer Cathodic Arc PVD Nitride-Base Coatings in 1M HCl and 3.5 pct NaCl Solutions," *Metallurgical and Materials Transactions B: Process Metallurgy and Materials Processing Science*, vol. 48, no. 2, pp. 1321–1332, Apr. 2017, doi: 10.1007/s11663-016-0891-7.
- [18] ASTM Standard, "2129–19a," 2019.
- [19] F. Mohammadi, T. Nickchi, M. M. Attar, and A. Alfantazi, "EIS study of potentiostatically formed passive film on 304 stainless steel," *Electrochim Acta*, vol. 56, no. 24, pp. 8727–8733, Oct. 2011, doi: 10.1016/j.electacta.2011.07.072.

- [20] M. Zhu, Q. Zhang, Y. Yuan, S. Guo, and Y. Huang, "Study on the correlation between passive film and AC corrosion behavior of 2507 super duplex stainless steel in simulated marine environment," *Journal of Electroanalytical Chemistry*, vol. 864, May 2020, doi: 10.1016/j.jelechem.2020.114072.
- [21] D. [ Wallinder A\ \ *et al.*, "EIS and XPS study of surface modi\_ cation of 205LVM stainless steel after passivation."
- [22] A. Salam Hamdy, E. El-Shenawy, and T. El-Bitar, "Electrochemical Impedance Spectroscopy Study of the Corrosion Behavior of Some Niobium Bearing Stainless Steels in 3.5% NaCl," 2006. [Online]. Available: [www.electrochemsci.org](http://www.electrochemsci.org)
- [23] A. Y. Adesina, Q. A. Drmosh, A. M. Kumar, and A. K. Mohamedkhair, "Post-annealing effect on the electrochemical behavior of nanostructured magnetron sputtered W3O films in chloride- and acid-containing environments," *Surf Coat Technol*, vol. 420, Aug. 2021, doi: 10.1016/j.surfcoat.2021.127334.
- [24] M. F. Khan, A. Y. Adesina, and Z. M. Gasem, "Electrochemical and electrical resistance behavior of cathodic arc PVD TiN, CrN, AlCrN, and AlTiN coatings in simulated proton exchange membrane fuel cell environment," *Materials and Corrosion*, vol. 70, no. 2, pp. 281–292, Feb. 2019, doi: 10.1002/maco.201810377.
- [25] A. M. Kumar, R. S. Babu, I. B. Obot, A. Y. Adesina, A. Ibrahim, and A. L. F. de Barros, "Promising Hard Carbon Coatings on Cu Substrates: Corrosion and Tribological Performance with Theoretical Aspect," *J Mater Eng Perform*, vol. 27, no. 5, pp. 2306–2316, May 2018, doi: 10.1007/s11665-018-3148-6.
- [26] M. S. Chen, Z. H. Zou, Y. C. Lin, H. Bin Li, and W. Q. Yuan, "Effects of annealing parameters on microstructural evolution of a typical nickel-based superalloy during annealing treatment," *Mater Charact*, vol. 141, pp. 212–222, Jul. 2018, doi: 10.1016/j.matchar.2018.04.056.
- [27] Q. Han, Y. Zhang, and L. Wang, "Effect of Annealing Time on Microstructural Evolution and Deformation Characteristics in 10Mn1.5Al TRIP Steel," *Metall Mater Trans A Phys Metall Mater Sci*, vol. 46, no. 5, pp. 1917–1926, May 2015, doi: 10.1007/s11661-015-2822-7.
- [28] M. Martins and L. C. Casteletti, "Sigma phase morphologies in cast and aged super duplex stainless steel," *Mater Charact*, vol. 60, no. 8, pp. 792–795, Aug. 2009, doi: 10.1016/j.matchar.2009.01.005.
- [29] W. Kuang *et al.*, "The effect of cold rolling on grain boundary structure and stress corrosion cracking susceptibility of twins in alloy 690 in simulated PWR primary water environment," *Corros Sci*, vol. 130, pp. 126–137, Jan. 2018, doi: 10.1016/j.corsci.2017.11.002.
- [30] Z. Mo *et al.*, "Effect of continuous annealing temperature on the microstructure, mechanical properties and texture of annealed drawn and ironed plate," *Crystals (Basel)*, vol. 11, no. 12, Dec. 2021, doi: 10.3390/cryst11121569.
- [31] R. Baboian and G. Haynes, *Electrochemical Corrosion Testing*, vol. 9. 2009.
- [32] W. T. Choi, K. Oh, P. M. Singh, V. Breedveld, and D. W. Hess, "Hydrophobicity and Improved Localized Corrosion Resistance of Grain Boundary Etched Stainless Steel in Chloride-Containing Environment," *J Electrochem Soc*, vol. 164, no. 2, pp. C61–C65, 2017, doi: 10.1149/2.1271702jes.
- [33] F. El-Taib Heakal, N. S. Tantawy, and O. S. Shehta, "Influence of chloride ion concentration on the corrosion behavior of Al-bearing TRIP steels," *Mater Chem Phys*, vol. 130, no. 1–2, pp. 743–749, Oct. 2011, doi: 10.1016/j.matchemphys.2011.07.064.
- [34] F. El-Taib Heakal, A. A. Ghoneim, and A. M. Fekry, "Stability of spontaneous passive films on high strength Mo-containing stainless steels in aqueous solutions," *J Appl Electrochem*, vol. 37, no. 3, pp. 405–413, Mar. 2007, doi: 10.1007/s10800-006-9271-3.
- [35] A. Y. Adesina, M. Hussain, A. S. Hakeem, A. S. Mohammed, M. A. Ehsan, and A. Sorour, "Impact of Heating Rate on the Tribological and Corrosion Properties of AISI 52100 Bearing Steel Consolidated via Spark Plasma Sintering," *Metals and Materials International*, vol. 28, no. 9, pp. 2180–2196, 2022, doi: 10.1007/s12540-021-01113-4.
- [36] A. Fattah-alhosseini, M. A. Golozar, A. Saatchi, and K. Raeissi, "Effect of solution concentration on semiconducting properties of passive films formed on austenitic stainless steels," *Corros Sci*, vol. 52, no. 1, pp. 205–209, Jan. 2010, doi: 10.1016/j.corsci.2009.09.003.
- [37] T. Bellezze, G. Giuliani, and G. Roventi, "Study of stainless steels corrosion in a strong acid mixture. Part 1: cyclic potentiodynamic polarization curves examined by means of an analytical method," *Corros Sci*, vol. 130, pp. 113–125, Jan. 2018, doi: 10.1016/j.corsci.2017.10.012.

- [38] T. Bellezze, G. Giuliani, A. Viceré, and G. Roventi, "Study of stainless steels corrosion in a strong acid mixture. Part 2: anodic selective dissolution, weight loss and electrochemical impedance spectroscopy tests," *Corros Sci*, vol. 130, pp. 12–21, Jan. 2018, doi: 10.1016/j.corsci.2017.10.010.
- [39] N. U. Obeyesekere, "Pitting corrosion," in *Trends in Oil and Gas Corrosion Research and Technologies: Production and Transmission*, Elsevier Inc., 2017, pp. 215–248. doi: 10.1016/B978-0-08-101105-8.00009-7.
- [40] G. S. Frankel, "Pitting Corrosion of Metals: A Review of the Critical Factors," *J Electrochem Soc*, vol. 145, no. 6, pp. 2186–2198, Jun. 1998, doi: 10.1149/1.1838615.
- [41] N. Ebrahimi, M. Momeni, A. Kosari, M. Zakeri, and M. H. Moayed, "A comparative study of critical pitting temperature (CPT) of stainless steels by electrochemical impedance spectroscopy (EIS), potentiodynamic and potentiostatic techniques," *Corros Sci*, vol. 59, pp. 96–102, Jun. 2012, doi: 10.1016/j.corsci.2012.02.026.
- [42] R. J. Brigham and E. W. Tozer, "Temperature as a Fitting Criterionfi."
- [43] "43".
- [44] Y. T. Sun, J. M. Wang, Y. M. Jiang, and J. Li, "A comparative study on potentiodynamic and potentiostatic critical pitting temperature of austenitic stainless steels," *Materials and Corrosion*, vol. 69, no. 1, pp. 44–52, Jan. 2018, doi: 10.1002/maco.201709641.
- [45] T. Li, J. R. Scully, and G. S. Frankel, "Localized Corrosion: Passive Film Breakdown vs Pit Growth Stability: Part II. A Model for Critical Pitting Temperature," *J Electrochem Soc*, vol. 165, no. 9, pp. C484–C491, 2018, doi: 10.1149/2.0591809jes.
- [46] A. Igual Muñoz, J. García Antón, J. L. Guiñón, and V. Pérez Herranz, "Inhibition effect of chromate on the passivation and pitting corrosion of a duplex stainless steel in LiBr solutions using electrochemical techniques," *Corros Sci*, vol. 49, no. 8, pp. 3200–3225, Aug. 2007, doi: 10.1016/j.corsci.2007.03.002.
- [47] G. Bruce *et al.*, "Metastable Pitting and the Critical Pitting Temperature," 1998.
- [48] "SHORT COMMUNICATION FAST METHOD FOR DETERMINATION OF CRITICAL PITTING TEMPERATURE."

## VITAE

|                            |  |
|----------------------------|--|
| <b>Name</b>                | Hani Mohammed Razaz Ahmed  |
| <b>Nationality</b>         | Saudi Arabia   |
| <b>Date of Birth</b>       | 1/7/1991   |
| <b>Email</b>               | Hani.Razzaz77@Gmail.Com  |
| <b>Address</b>             | Al-Khobar City - Al Hamra Dist. (2979) – Zip Code (34628)  |
| <b>Academic Background</b> | BSc. Mechanical Engineering - 2015<br>MSc. in Material Science & Engineering - 2023  |
| <b>Publishes</b>           | <i>Journal</i> Journal of The Electrochemical Society [MDPI]   |
|                            | <i>Type</i> Research Paper   |
|                            | <i>Published</i> 8 December 2022   |
|                            | <i>Article Title</i> Effect of Solutionizing Duration and Temperature on the Electrochemical Corrosion and Pitting Resistance of Cold-Rolled Super Austenitic Stainless Steel  |
|                            | <i>Keywords</i> Stainless Steel; Supersaturated Austenite; Heat Treatment; Annealing; Corrosion; Pitting; Electrochemical Impedance Spectroscopy (EIS)   |
|                            | <i>DOI</i> <a href="https://doi.org/10.3390/ma15248780">https://doi.org/10.3390/ma15248780</a>   |
|                            | <i>Citation</i> “Adesina, A.Y.; Ahmed, H.M.; Suleiman, R.K.; Hassan, S.F. Effect of Solutionizing Duration and Temperature on the Electrochemical Corrosion and Pitting Resistance of Cold-Rolled Super Austenitic Stainless Steel. <i>Materials</i> 2022, 15, 8780. <a href="https://doi.org/10.3390/ma15248780">https://doi.org/10.3390/ma15248780</a> ” |